PICOSECOND VACUUM ULTRAVIOLET WAVELENGTH GENERATION

by

Robert John Manning BSc., A.R.C.S.

A thesis submitted in partial fulfilment of the
requirements for the degree of Doctor of Philosophy
of the University of London and the Diploma of
Imperial College

December 1981

Blackett Laboratory,
Imperial College
London SW7 2AZ

England

To my parents.

ABSTRACT

This work describes the use of a ruby laser for harmonic generation. The operation of a passively mode-locked ruby oscillator, operating in TEM_{oo} transverse mode, is discussed and techniques for optimising its performance are outlined.

A single stage amplifier was used in conjunction with the oscillator to provide light pulses having energies up to 4.5 millijoules. Using an electron-optical streak camera, the pulse durations were measured to be between 15 psec. and 30 psec. The pulse trains were used to generate the second harmonic of ruby (at a wavelength of 3471.5 Å), in a non-linear crystal.

By focussing the emergent beams from the crystal into a column of magnesium vapour, the fourth harmonic at 1735 Å was produced via a four-wave mixing process. Xenon was used as a phase-matching gas and served additionally as a buffer. Power conversion efficiencies (from the fundamental frequency) of between 2.4×10^{-4} and 1.8×10^{-3} were obtained, corresponding to a variation in the magnesium atomic number density from 3.2×10^{22} m^{-3} to 7.35×10^{22} m^{-3}. The scaling of the fourth harmonic power with fundamental intensity was investigated, and scans of the relative signal with pressure and temperature as variables were undertaken.

The theory of the fourth harmonic process was developed, and is presented in this thesis. Good agreement was found between this theory and the experimental results for low magnesium number densities. At higher number densities saturation effects were observed, and possible reasons for this are discussed. From experimental data, a value for the susceptibility $\chi^{(3)}(-4\omega_1, \omega_1, \omega_1, 2\omega_1)$ of 5.5 ($\pm$ 0.7) $\times 10^{-49}$ m^5 v^{-2} was deduced. Applications of the fourth harmonic, in particular its possible amplification in an inverted Xe_2^* medium, are outlined.

CONTENTS

Page

Chapter 5 (continued)

LIST OF PLATES

CHAPTER 1

GENERAL INTRODUCTION

The invention of the laser very quickly led to the demonstration of non-linear optical effects in various media[1,2], due to the intense light fluxes which were consequently made available for the first time. There was a rapid growth of interest in non-linear optics, which has continued to the present day. The primary reason for this interest was that non-linear behaviour (sum frequency generation, difference frequency generation and harmonic generation) could be exploited in various devices to provide coherent light in parts of the spectrum where previously no coherent source was available.

With the discovery of mode-locking[3] came the possibility of providing highly intense light pulses which had durations of a few picoseconds or less. These pulses were ideal for improving conversion efficiencies of intensity dependent, higher order non-linear processes. They also offered exciting possibilities for probing the behaviour of various media, at previously inaccessible wavelengths, on a time-scale at which only electronic transitions would occur. Furthermore, energy levels in the atoms or molecules of the non-linear medium which could not be populated by straightforward single photon absorption, could be populated by using two (or more) photon absorption or other non-linear processes. Many experiments using these kind of techniques have since been carried out [e.g. 4, 5, 6]. Experiments have also been performed in which a laser producing one wavelength has been used to generate, via non-linear effects, light of a frequency at which another

laser operates, and the microscopic properties of the active medium have then been studied [7,8,9].

A knowledge of non-linear effects is also useful because these come into play at high intensities and so set an upper bound on the light flux which can be passed through a medium without either absorption (two- or multi-photon) which depletes the incident light, or distortion of the beam (spatially by self-focussing, spectrally or temporally by self-phase modulation). Very high light levels may also permanently damage the medium, especially if it is a solid.

Much early work was concentrated on crystalline non-linear media. This was due to the fact that the second order non-linear susceptibility is zero in centrosymmetric media (crystals that are used lack a centre of symmetry). Because of this, other media would only exhibit higher order, and therefore weaker, non-linear effects. It was also shown by several authors [10,11,12] that, by exploiting the birefringent properties of the crystal, the phase velocities of the fundamental and generated wavelengths could be equalised. This so-called "phase matching" enabled long coherence lengths to be used, which greatly increased conversion efficiencies. However, there were major drawbacks with crystalline materials, notably their damage threshold and their transparency (or lack of it) at the fundamental and second harmonic wavelengths.

For these reasons, gases and vapours have been studied more extensively in recent years. These media show very low absorption in both the ultra-violet and infra-red, and do not suffer irreversible damage at large light fluxes. However, vapours generally have much lower number densities than solids and are centrosymmetric, and consequently the lowest order non-linear processes they exhibit are of the third order. These effects are smaller in magnitude than ones

of second order, and to compensate, either the electric field strengths of the incident radiation must be correspondingly higher, or the third order susceptibility must be resonantly enhanced. This may be done by suitable choice of the interacting frequencies and the non-linear medium so that the wavelengths are close to resonance with the energy levels of the medium.

The study of non-linear properties of gases was pioneered by Ward and New[13], who produced the third harmonic of a ruby laser in a variety of gases. However, both the third harmonic and fundamental frequencies were well away from any resonance, and the process was not phase-matched, and consequently conversion efficiencies were extremely low. A major advance in the field was then made by Miles and Harris[14], who used alkali metal vapours to act as the non-linear media, which were phase-matched by adding a buffer gas. This buffer gas was positively dispersive at the frequencies used, and its addition compensated for the negative dispersion of the metal vapour. By exploiting the energy levels present in these media the susceptibilities were resonantly enhanced, and it was shown that high conversion efficiencies were possible. Third harmonic generation with a high power mode-locked Nd:YAG laser source has since given conversion efficiencies of several percent[15].

If tunable sources in the ultraviolet (uv) or vacuum-ultraviolet (vuv) are required, dye lasers may be used as the tunable fundamental. The peak powers are much less than those available from mode-locked ruby or neodymium lasers, but dye lasers offer the advantage of tunability in the generated harmonic, and also may be tuned to a wavelength at which the susceptibility is resonantly enhanced. Hodgson et al.[16] obtained useful powers over a considerable range of the vuv by tuning one dye laser source to a two-photon resonance

in Sr vapour and frequency summing using a second dye laser source. Bloom et al.[17] used Na vapour to obtain up-conversion from the infrared to the uv with a conversion efficiency of 50%.

It is apparent that harmonic and sum frequency generation will play an important part in providing sources of coherent light in the uv and vuv. These processes are of the the "parametric" type, which refers to the fact that the atoms taking part in the non-linear process are returned, after the interaction, to their initial state. This thesis describes work which was primarily devoted to the study of one such process: the production of the fourth harmonic of a mode-locked ruby laser. The non-linear medium chosen was magnesium vapour, which has not been studied at all extensively in the literature. Most authors have concentrated on the alkali metals, though in the past few years Mg has been used more than previously[18, 19, 20]. The process involves the frequency mixing of two fundamental (ruby) photons and a second harmonic photon in Mg vapour, to produce picosecond light pulses at a wavelength of 1735 Å, which is the vuv region of the spectrum.

Chapters 2 and 3 of this thesis describe the necessary preliminary work that was done in order to produce the fourth harmonic, that is, the development of a reproducible mode-locked ruby laser and amplifier system, and the generation of the second harmonic (at a wavelength of 3471 Å). The following chapter gives theoretical details of the frequency mixing process that generates fourth harmonic, and the fifth chapter outlines the practical work undertaken. Chapter 6 outlines possible applications of the fourth harmonic, and in particular discusses the possibility of amplification in an inverted Xe_2^* medium. Finally the general conclusions found from the work are presented.

CHAPTER 2

THE MODE-LOCKED RUBY LASER SYSTEM

I. Introduction

The source of light at the fundamental frequency, which was to be doubled and subsequently frequency mixed, was a ruby laser, operating at 6943Å. This laser was run in T.E.M.$_{oo}$ mode, and was passively mode-locked to produced pulses of approximately 20 psec. in duration. It was possible to preserve a beam of good spatial quality after a single stage of amplification and this allowed powers of up to 200 MW per pulse to be obtained. This availability of high powers in a good quality beam was the justification for the use of the ruby system in the work, these two features being essential for efficient harmonic generation.

It is of interest to note that not only was ruby the first material in which laser action was demonstrated[21], but it was also the first laser to be passively mode-locked[22]. Even today it is still one of the most useful laser materials, due to its high output power and good spatial quality at its operating wavelength. The active medium in ruby is Cr^{3+}, which is present as an impurity in Al_2O_3 crystal (sapphire). Pink ruby, which was used in this work, results from a Cr doping of 0.05% by weight. The energy level diagram is shown in Figure 2-1 (taken from Reference[23]).

Ruby is normally pumped by irradiation with light from a pulsed xenon lamp, which emits radiation in the blue and green, corresponding to the two absorption bands $^2F_2$ and $^4F_1$ of the Cr^{3+} ions. The ions

Energy Levels For Ruby

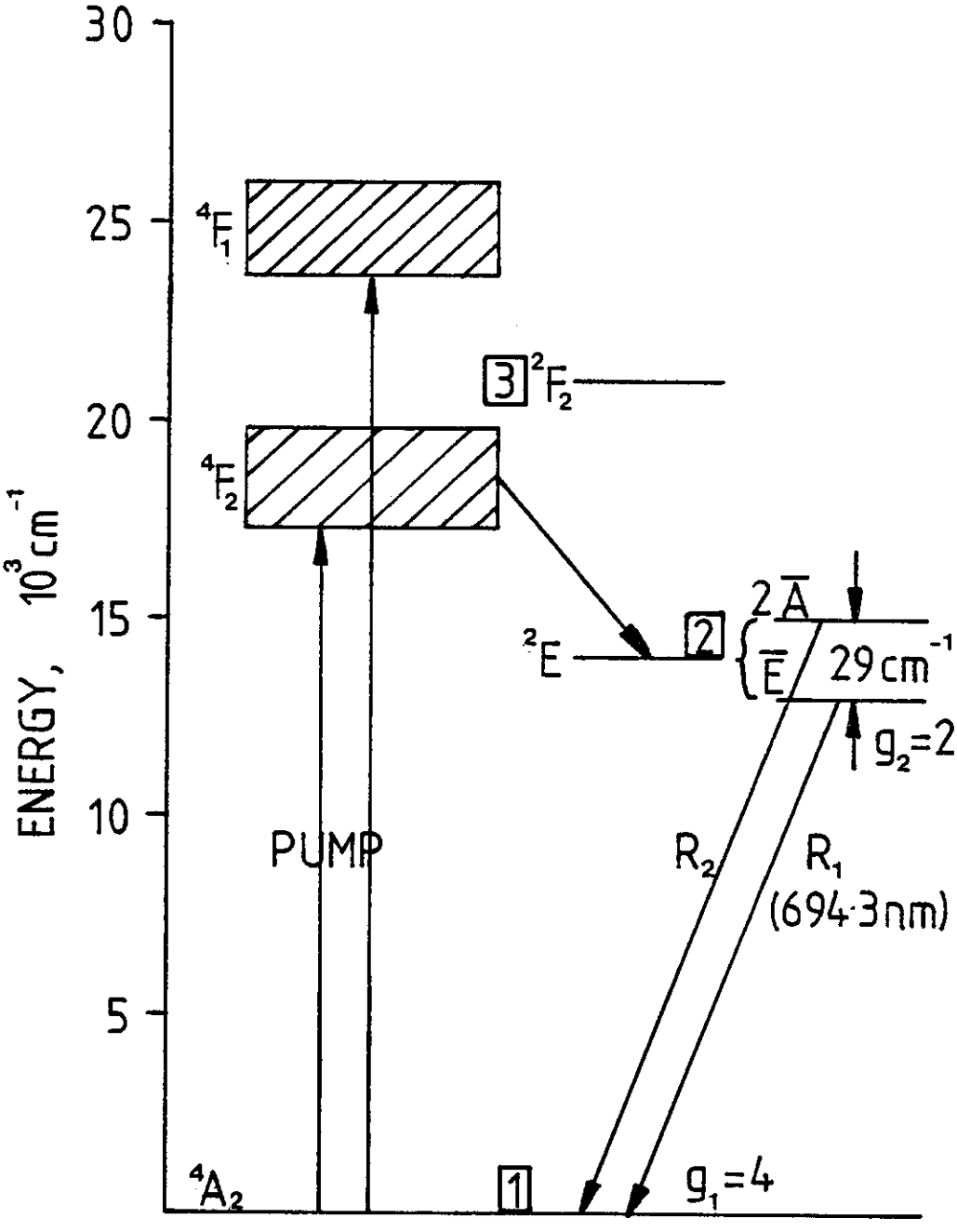

Fig 2-1

populating these levels quickly decay (with a lifetime of $\sim 5 \times 10^{-8}$ secs) into the upper laser level ^2E. This upper level in fact consists of two levels, $2\bar{A}$ and $\bar{E}$, which are separated by 29 cm^{-1}. It is the lower of these levels $\bar{E}$, which is actually the upper laser level. The lower laser level is the ground state, and the ruby thus forms a three level system. Its threshold is therefore slightly higher than the corresponding Nd^{3+} systems (these being four-level systems).

The lifetime of the upper laser level is approximately 3×10^{-3} secs, and flashlamps used to pump ruby must have pulses of this half width or less to optically excite the ruby efficiently. A wide lasing bandwidth is required if any system is to be capable of producing picosecond pulses. Ruby enjoys the advantage of having a bandwidth of $3\mathring{A}$, which permits picosecond pulses to develop, but is also narrow enough to allow reduction to single longitudinal mode operation[25]. Picosecond pulses are generated within the cavity by use of a saturable dye in contact with the back (100% reflectivity) mirror. The choice of dye depends upon the duration of pulses ultimately required (see next section), and in this work the shortest (and therefore most intense) pulses possible were needed. Consequently 1,1'-diethyl-2, 2'-dicarbocyanine iodide (DDCI) in ethanol was used, which has a fluorescence lifetime of $\sim$11 psec.[24].

The background theory to passive mode-locking is given in the following section. The experimental system is described next, and polaroid and streak records are presented. Finally details of the single-stage amplification are given, and conclusions are presented.

II. Background Theory to Passive Mode-Locking

When a laser has been mode-locked, its output consists of a train of pulses (of duration less than the round trip time) which

are separated by the round trip time of the cavity. To achieve this behaviour, a saturable dye is placed inside the cavity, normally in contact with the back mirror. The dye can be thought of as a switch which opens and closes every round trip. This technique of so-called passive mode-locking is capable of producing pulses whose half-widths are the order of picoseconds.

Mode-locking refers to the fact that, to produce such high intensity, short duration pulses, it is necessary to maintain a fixed phase and fixed amplitude relationship between all the longitudinal modes [26]. These longitudinal modes are separated in frequency by c/2L, where c is the velocity of light and L is the length of the laser resonator[27]. Their number is determined by the shape of the laser gain curve in frequency space. When ideal mode-locking arises, the laser may be said to be in a perfectly organised state.

Most theoretical explanations of mode-locking are based on a time-domain model, the so-called "fluctuation model" first suggested by Letokhov[28] and Fleck[29]. In this picture, the mode-locked intensity distribution originates from the initial fluorescence intensity fluctuations present at the time threshold is reached for the laser. The duration of these fluctuations is of the order of the inverse of the bandwidth. This noise pattern is random in nature and is different on every firing of the laser[30]. The saturable absorber acts in such a way as to preferentially select the most intense peaks in the pattern, and finally one (ideally) of the peaks is many times more intense than the rest. After this selection process, intensity dependent non-linear effects (predominantly self-phase modulation and self-focussing) may come into play. These usually take place in the laser medium, and lead to spectral and temporal broadening or even fragmentation of the mode-locked pulse in the cavity[31]. Spatial distortion or break up can also result.

The build up of mode-locking has been observed experimentally in several laser systems, in particular Nd lasers[32], and the ruby laser, where the effect of the lifetime of the saturable absorber on the pulse duration ultimately obtained has been convincingly demonstrated [33]. The stages of the mode-locking process are shown in Figure 2-2. At the beginning of the flashlamp pumping pulse, spontaneous emission occurs. As the gain builds up, the radiation pattern within the cavity develops a structure which repeats itself every round trip time, $T(= 2L/c)$. At the laser threshold, the gain exceeds the linear and non-linear losses in the resonator and the stage of linear amplication begins (at time t_1 in Figure 2-2). Spectral narrowing occurs and this leads to broadening of the duration of the fluctuations. The linear stage continues until saturation effects in the absorber become significant. The second stage of pulse development, the non-linear stage, then begins (at time t_2). It was assumed in the earlier theoretical papers[28] that this second stage is complete before the final giant pulse stage occurs, where the population inversion in the laser medium is depleted and laser action terminates. This requires the largest fluctuations to reach an intensity such that they saturate the absorber without depleting the gain. If this indeed happens, the fluctuations continue to develop independently.

However, it is found in practice that a clear division between the non-linear and giant pulse stages can rarely be drawn. This was pointed out by Glenn [34] and has been discussed further by New[30]. It now seems clear that the best mode-locking occurs just above the "second threshold" of the laser[32], where absorber saturation and gain depletion are in a state of delicate balance and combine to transform the random intensity structure into a single dominant pulse.

Behaviour Of Gain, Intensity And Spectral Width In Mode-Locking (From Reference [37])

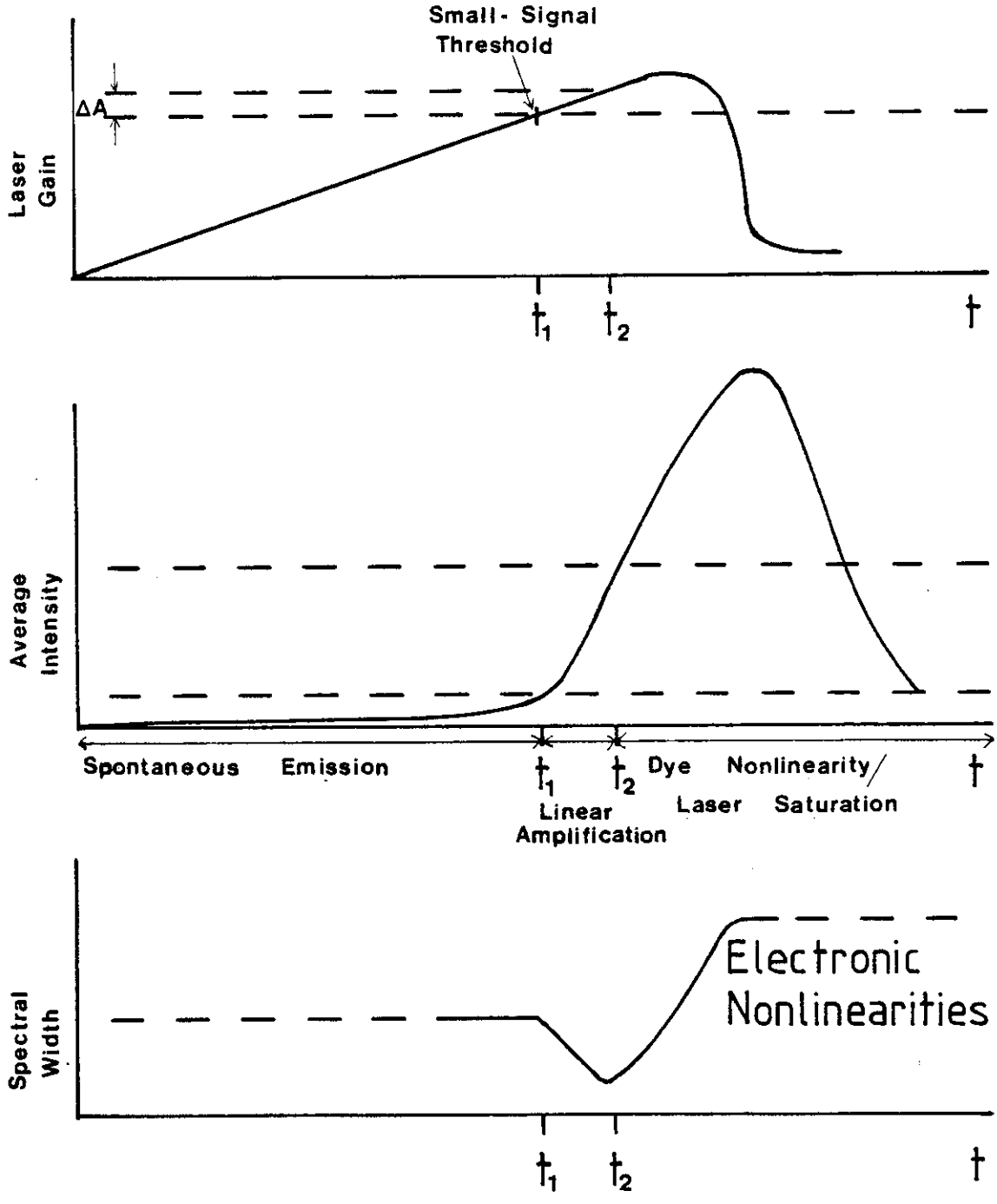

Fig 2-2

The interplay of these two effects leads to the individual fluctuations of the intensity patterns losing their independence.

The pulse intensities in the non-linear stage are determined by the equation[34]:

$$\frac{d}{dk} I_{k_i} = I_{k_i} \left(A_{k_i} - \Gamma - \frac{B_o}{1+I_{k_i}} \right) \qquad (2\text{-}1)$$

where the symbols have the following meaning:

I_{k_i} is the intensity of the ith member of the set of M pulses circulating in the cavity, at the kth pass. This intensity is normalised to the saturation intensity of the absorber $I_s = (2\sigma_b T_{1b})^{-1} . h\nu$

A_{k_i} is the gain of the kth pass, for the ith pulse

Γ represents the cavity losses (mirror transmission and scattering)

σ_b is the cross-section of the dye absorber

T_{1b} is the relaxation time of the dye

B_o is the initial (small signal) absorption coefficient

$k = t/T$

T is the round trip time

A_{k_i} obeys the equation

$$\frac{dA_{k_i}}{dk} = - A_k (2\sigma_a I_s T) I_{k_i} + fT \qquad (2\text{-}2)$$

where f is the rate of flashlamp pumping

σ_a is the gain cross-section.

Both equations (2-1) and (2-2) assume an instantaneous response for the absorber, and that a linearly increasing value of A is produced by the flashlamp if acting alone.

The effective gain coefficient is

$$G = A - r - \frac{B_o}{(1+ I_{k_i})} \tag{2-3}$$

A clear distinction between the non-linear and giant pulse stages can be made if the depletion of A is negligible during the non-linear stage. In this case the value of A in equation (2-1) may be replaced by its initial (unsaturated) value, and the M equations become independent of one another. If this is not so, A must be computed for each pass, and the pulses will not evolve independently.

G is positive for all the pulses in the intensity pattern at the beginning of the non-linear stage. After this time, however, only pulses which are above a certain critical intensity I_c will continue to experience net gain. G is equal to zero for pulses whose intensity is equal to I_c, which is given by the expression

$$I_c = \left(\frac{B_o}{A-r} \right) - 1$$

$$= \left(\frac{B_o}{B_o + \Delta A} \right) - 1 \tag{2-4}$$

As the gain becomes depleted, ΔA ($= A - \Gamma - B_0$) goes to zero and becomes negative, thus increasing the value of I_c. This depletion improves the pulse selection process since a very large pulse will deplete the gain faster and cause I_c to rise more rapidly. Smaller pulses are then more effectively eliminated. Ideal mode-locking requires the eventual growth of one pulse only. The basic behaviour predicted by this model is illustrated in Figure 2-3 (from New [30]). In particular, it is seen that ideal operation occurs under the circumstances outlined above, where only one pulse eventually emerges from the region of non-linearity.

The results, and those of Glenn from computer simulations, show that the excess gain $\Delta A = A - \Gamma - B_0$ existing at the beginning of the non-linear stage is the crucial parameter governing the quality of the mode-locking. There is a small range of values for $\Delta A > 0$, for which a single pulse is nearly always selected. This effectively means that the best mode-locking will be obtained when running the laser just above threshold. For $\Delta A < 0.01$, the gain is depleted before any pulse can saturate the dye, whilst for $0.01 < \Delta A < 0.02$ excellent discrimination between fluctuations is predicted. For higher values of excess gain, discrimination is poor.

The dye not only plays an essential part in selecting the larger fluctuations, but also causes the profile of each pulse to shorten. [35] If the relaxation time of the dye T_{1b} is longer than the mean duration of the fluctuation peaks occurring at the beginning of the non-linear stage, then the pulses of duration $t < T_{1b}$ are poorly selected and the resultant giant pulse will frequently consist of a series of noise spikes. To select the most intense peak effectively

Development Of A Set Of Fluctuations
a) When Gain Saturation is Neglected
b) Showing the Effect of Gain Saturation

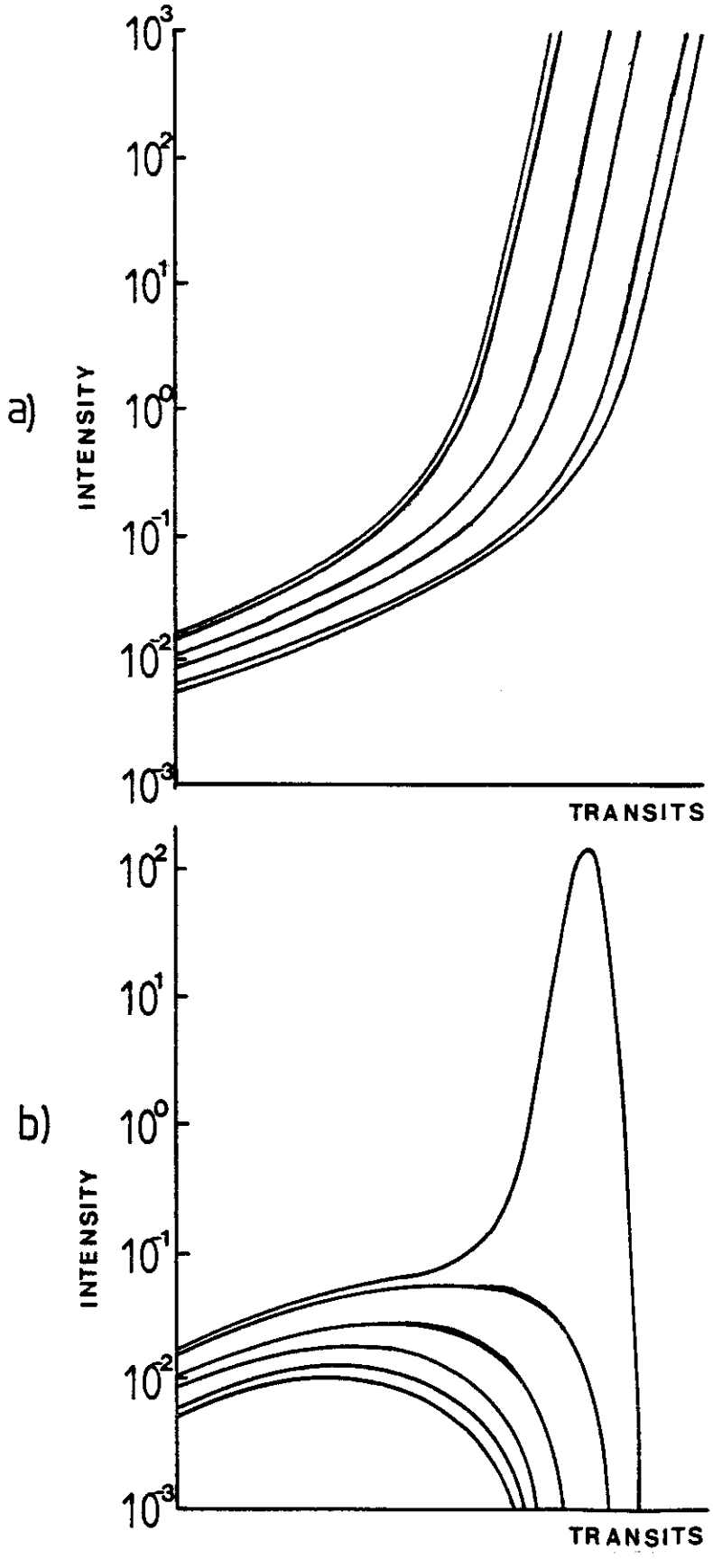

Fig 2-3

the condition

$$M \cong T/T_{1b} \qquad (2\text{-}5)$$

should be satisfied.[36]

III. The Ruby Oscillator

III-1 General Aspects

A major part of the early experimental work of this thesis was devoted to the development of a reliable and reproducible mode-locked ruby laser. There are several well-known conditions which must be satisfied if reliable mode-locking is to be achieved [37]. These include:

a) High Optical Quality and Cleanliness.

b) Optimum Cavity Configuration

It is essential that spurious reflections inside the cavity be eliminated, and also that feedback from optical components outside is avoided. Single transverse mode operation is desirable[30]. Thermal effects in the laser rod which can distort the transverse mode structure of the beam should be minimised.

c) Optimum Absorber Configuration

The optimum arrangement is for the saturable dye to be placed in a thin cell in optical contact with one of the cavity mirrors (preferably the one of highest reflectivity)[38]. Since the duration of the pulses is limited ultimately by the relaxation time of the absorber, this time should be as short as possible [36].

d) Minimising Non-Linear Effects

As discussed in the previous section, self-phase modulation and self-focussing often occur in the final (giant pulse) stage of pulse development, usually in the laser medium. The degree to which these phenomena occur may be reduced by working at low power densities. This entails using a high value for the low light level transmission of the saturable dye ($\geq$ 70%).

e) Optimisation of the Excess Gain Parameter, ΔA

ΔA should be made as small as possible, which requires that the laser be fired very close to threshold.

A laser design incorporating the above requirements was utilized. The ruby rod was of the best optical quality and both ends were cut at Brewster's angle. Since the output from ruby is polarised perpendicularly to the c-axis, Brewster angled faces reduced the reflection loss within the cavity, as well as preventing oscillation within the rod itself. All the rest of the resonator components were wedged. T.E.M.$_{oo}$ mode operation was achieved by the use of a circular aperture placed in the cavity. This was drilled through a thin ($\sim$ 1mm) dural sheet, which was subsequently countersunk and then anodised to prevent stray reflections. Several aperture sizes were in fact tried before the correct size ($\simeq$ 2mm in diameter) was discovered. (The relevant burn marks on spent polaroid placed about 60 cm. from the output mirror were examined for shape and quality in each case.)

The saturable absorber dye was in optical contact with the back (100% reflectivity) mirror and was contained in a thin adjustable cell, set to a thickness of 400μm. As previously stated, the dye was

DDCI in ethanol, which has a fast relaxation time of $\sim$ 11 psec. The transmission of the dye was approximately 70% for low light levels, which corresponded to a 3.1×10^{-5} molar solution. Methanol was used firstly as the dye solvent, but was found to cause rapid deterioration of the rear mirror surface. Ethanol had a less severe effect upon the coating.

The optical resonator consisted of a plane output mirror (soft coated) of $\sim$ 80% reflectivity at 6943 Å, and a rear mirror of nominally 100% reflectivity. This latter mirror had a hard baked coating to withstand the ethanol, and had a radius of curvature of 5m . Both mirrors were 1" in diameter and were coated on wedged glass substrates. A red filter, of $\sim$ 80% transmission at 6943 Å, was placed immediately in front of the dye cell, to prevent the possible photo-decomposition of the dye by stray u.v. light from the flashlamp. A schematic of the cavity is shown in Figure 2-4.

III-2 Optical Resonator Considerations

Petty has shown [25] that the ruby rod in a pumped condition can be considered to behave as a thin, diverging lens of focal length f = -7 m. This lens and the output (plane) mirror may be considered to act as a single convex mirror, whose focal length f' is given by:

$$\frac{1}{f'} = -\left(\frac{2}{f} + \frac{2d}{f^2}\right) \qquad (2\text{-}6)$$

Where d is the separation of the ruby lens and plane mirror, and f is positive in this formula. The effective mirror is located at a distance d' from the ruby lens, where

$$d' = \frac{fd}{f + d} \qquad (2\text{-}7)$$

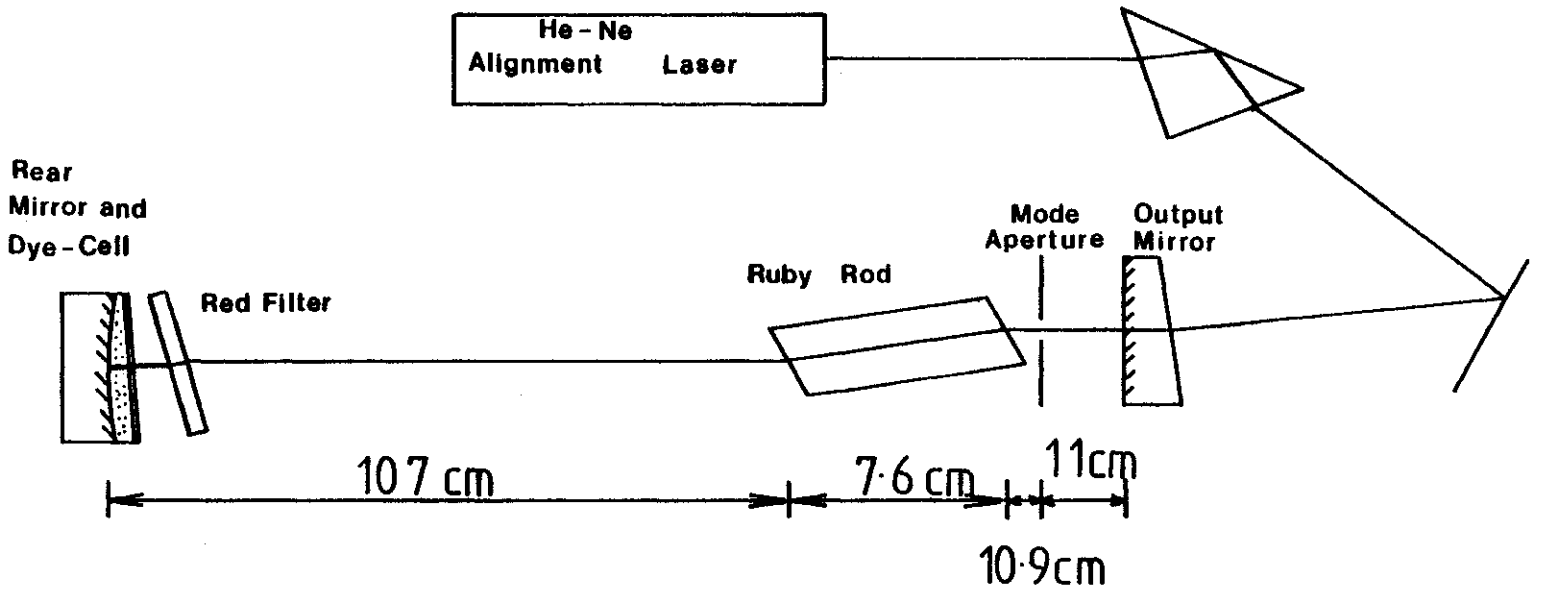

a) The Ruby Oscillator

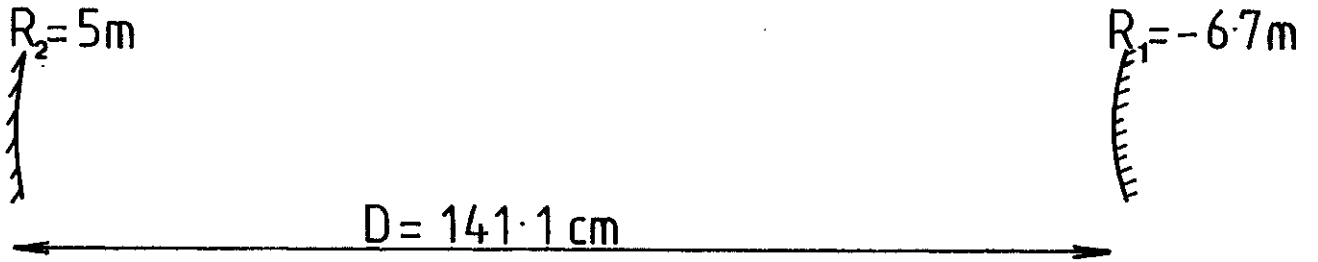

b) Effective Mirror Configuration

Fig 2-4

Substituting the relevant values into these equations yields the values f' = - 3.36 m, and d' = 27.5 cm, where the length of the ruby rod has been replaced by an effective length l' = n x 7.62 cms = 13.4 cms (n = 1.76). The effective mirror configuration is shown in Figure 2.4 (b). According to optical resonator theory[39], a cavity is stable if it obeys the condition

$$0 \leq \left(1 - \frac{D}{R_1}\right)\left(1 - \frac{D}{R_2}\right) \leq 1 \qquad (2\text{-}8)$$

Where D is the effective distance betweenthe mirrors and R_1 and R_2 are the two mirror radii. Using the values calculated above, the product of the two terms is found to be ≈ 0.84, which obviously satisfies (2-8). The effective cavity lies in the top right hand side of the stability diagram[40].

III-3 Operation of the Ruby Oscillator

A photograph of the ruby system is given in Plate 1. The ruby rod was mounted in the cavity head and surrounded by a concentric cylindrical quartz jacket through which cooling water (distilled) continuously flowed. This jacket lay immediately inside the helical, xenon filled, flashlamp; and this in turn was surrounded by a cylindrical aluminium reflector which also served to pre-pulse the lamps before firing (being connected to a third electrode pulsed to ∿ 25 kV). The lamps were fired from a capacitor bank consisting of 8 x 38μF capacitors, which discharged through a 500μH inductance to slow the rise time of the pulse (this reduced shock in the tube). The lamps fired when a thyratron, which held off the capacitor bank voltage, was made to conduct by the arrival of a trigger pulse.

PLATE 1

The Ruby Oscillator and Amplifier System

The Ruby Oscillator is on the L.H.S. of the photograph. To its right lies the He-Ne Alignment laser, and then the Ruby Amplifier Head. The A.D.P. Second Harmonic Crystal may be discerned (covered with silver foil) in the background. On the far left are gas lines leading to the heat-pipe (to be described later).

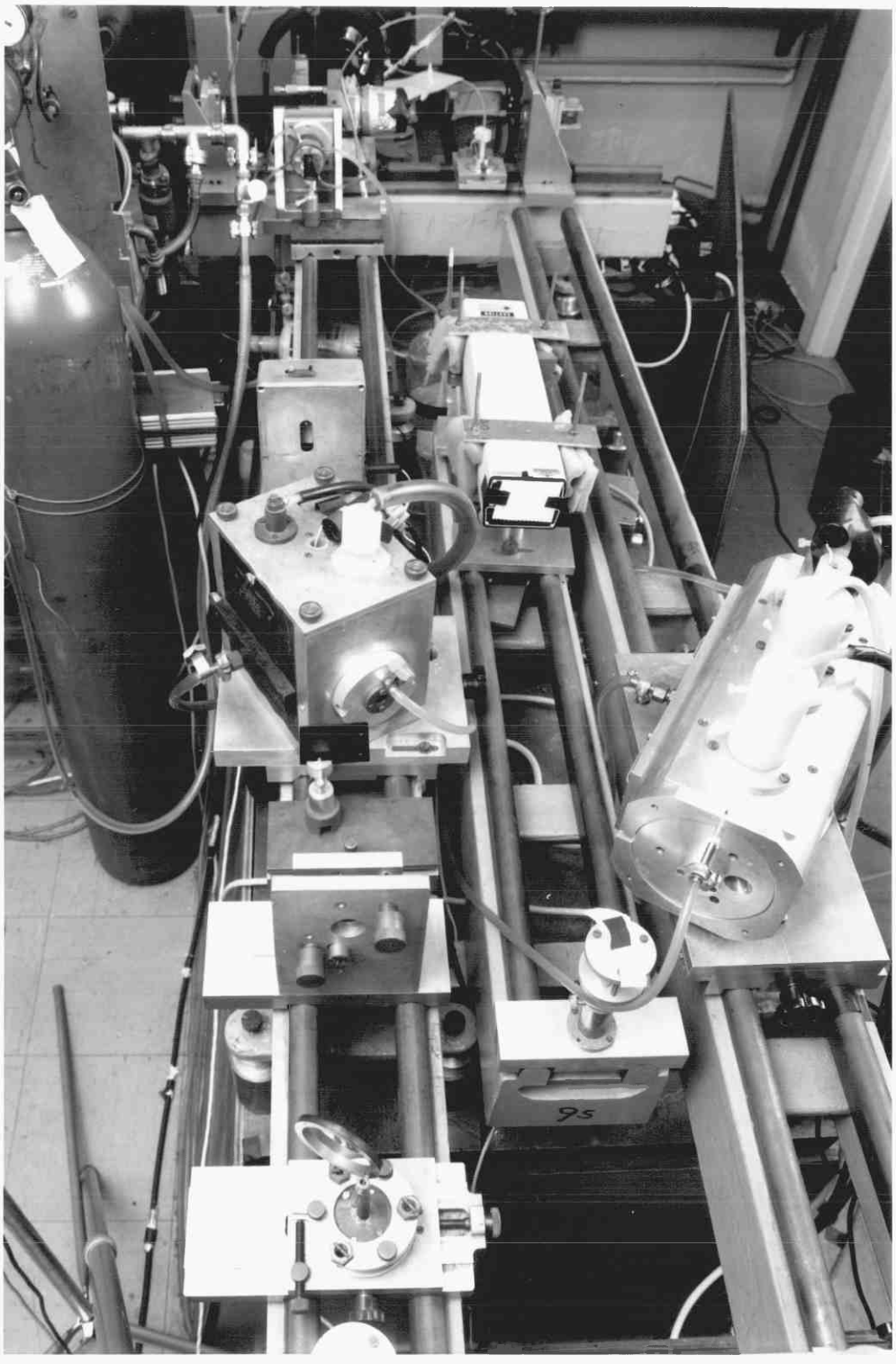
9s

III-3.1 Alignment

The system was aligned using a He-Ne laser and pellicle (as shown in Figure 2-4(a) and in Plate 1). The output mirror was put in place and adjusted simultaneously with the pellicle until the He-Ne beam ran parallel to the optical bench, and the return spot from the front mirror fell coincidentally upon the output from the He-Ne (i.e. it returned along the same path). A white covering with a small aperture was placed over the front of the He-Ne laser to facilitate location and final adjustment of the return spot. The cavity head was then positioned such that the He-Ne beam passed down the centre of the rod and it was ensured that the displaced He-Ne beam still ran parallel to the optical bench (the rod had to be slightly rotated if this was not the case). Finally the red filter and back mirror were positioned and the transverse mode selector was placed between the cavity head and output mirror. By adjusting the rear mirror the reflected spot was found on the rear side of the anodised mode selector. Since the spot was larger than the aperture, alignment was achieved by allowing the spot to fall symmetrically, as judged by eye, onto the hole. It was often found in practice that optimum alignment coincided with the spot falling slightly assymmetrically on the TEM_{00} mode aperture.

III-3.2 Precautions

It was found that, in order to produce an output from the oscillator which consisted of a single train of mode-locked pulses on a consistent basis, several precautions had to be taken, each one of which was crucial in determining the degree of reproducibility obtained. These steps are outlined below:

III-3.2(a) Temperature Control

The temperature of the distilled water used for cooling purposes had to be maintained at a strictly constant temperature (a variation of more than ± 0.2°C led to irreproducibility). The water was kept in a temperature controlled, 5 litre bath.*

It has been noted[41] that the transmission of the mode-locking dye can change by up to 1% for each 1°C change in temperature for Neodymium systems. Temperature control of the dye in the present system, to within ± 0.1°C, led to a noticeable improvement in shot-to-shot reproducibility. This was achieved by placing the 1 litre conical flask containing the mode-locking dye solution in the temperature-controlled water bath, and continuously flowing the dye through the dye cell by means of a pump (centrifugal type). By placing the pump so that the dye solution entered it after having passed through the cell, air bubbles were prevented from appearing in the cell. The dye solution in the conical flask was continuously stirred (using a small motor) and its temperature monitored. The bath and flask were covered with an aluminium top to keep the dye in darkness, preventing gradual photo-decomposition of the dye by the room lights.

In order to keep the cell at the same temperature as the dye, a brass coil, through which distilled water from the bath was pumped, was fitted to the outside of the cell. This had the additional function of stabilising the temperature of the rear mirror mount. The temperature of the water was usually maintained at ∿ 18°C, this being high enough to prevent condensation of water vapour from the atmosphere on any of the optical surfaces.

---

* Supplied by Grant Instruments of Cambridge

III-3.2(b) Voltage Control

The voltage at which the capacitor bank was discharged, monitored using a digital voltmeter, proved to be absolutely critical. Once the threshold had been found on any particular day, it was discovered that a measured variation of as little as 5V above this threshold (in usually $\sim$ 5.1kV) led to a noticeably greater number of trains consisting of multiple pulses. It is of interest to note that the flashlamp was reproducible enough for this to be apparent. Care had been taken to pre-pulse (or "pseudo-simmer") the lamps before the capacitor bank voltage appeared across them, using a variable electronic delay which could deliver a pulse to the lamps anything up to 1 msec before the capacitors discharged through the thyratron. Pseudo-simmer is a widely used technique to enhance the reproducibility of flashlamps[41].

The lamp was monitored to assess its reproducibility using a biplanar fast photodiode (ITT) and a Tektronix 7844 oscilloscope. Two photographs, one obtained from a single firing of the flashlamp, and one obtained from a series of five shots, all overlaid, are shown as part of Plate 2. The extreme reproducibility is immediately evident.

These results are obviously in keeping with the discussion of Section II, in particular with the argument that the laser must be fired as close as possible to threshold, in order that a single pulse will be selected via absorber saturation and gain depletion, that is, that the excess gain parameter ΔA should be minimised.

The apparent very low tolerance on the temperature and voltage variation led to an investigation of the interdependence of these two parameters. The dye temperature was controlled independently in another temperature-stabilised water tank and the cooling water temperature was varied in approximately 1.5°C steps, the corresponding threshold being

PLATE 2

Reproducibility Aspects

Photographs a and b demonstrate the flashlamp reproducibility

a - Single shot

b - Five shots overlaid

Vertical scale: 20 mv/cm

Timebase: 0.2 msec/cm

c and d show the effect of slight misalignment on the mode-locked train shape.

c shows a mode-locked train when the cavity is properly aligned.

d shows the affect of a slight misalignment.

Vertical scale: 10 V/cm

Timebase: 50 nsec/cm

a

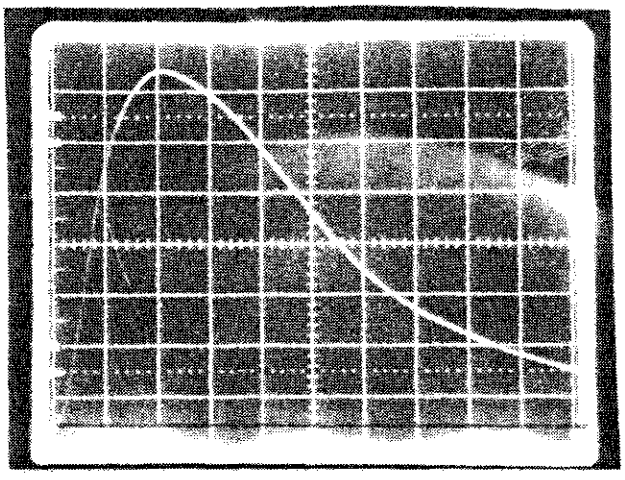

b

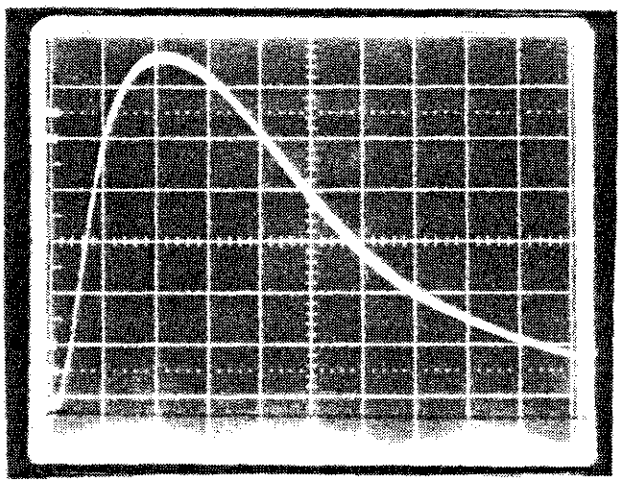

c

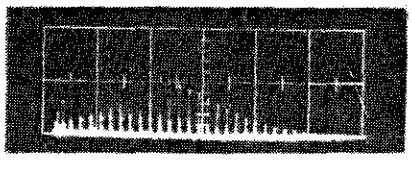

d

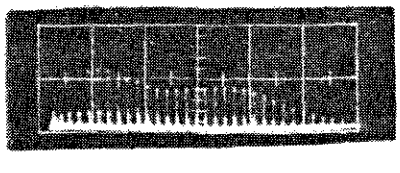

recorded for each new temperature. A graph of the results is shown in Figure 2-5, from which it is apparent that a 1°C rise in temperature at 18°C leads to approximately a 12 V rise in the threshold. Thus, to control the threshold to within 4 V, a variation in the water temperature of no more than 0.3°C may be allowed.

A similar experiment, to determine the dependence of the threshold upon the dye temperature, with the cooling water temperature held constant, was attempted but proved inconclusive since the shifts in temperature of the dye also led to the rear mirror mount changing in temperature and the system consequently moved out of alignment. This first led to a rise in threshold until the alignment became so poor that lasing could no longer take place. It proved impossible in practise to re-align exactly to mimic the previous conditions, and so no definite conclusions could be drawn from the results.

III-3.2(c) Alignment

Alignment of the system for operation in TEM_{oo} mode was extremely critical, and temperature controlled mounts were required to maintain a stable configuration. Slight changes in alignment were found to raise the threshold drastically (by several hundred volts), and also alter the shape of the mode-locked trains (see Plate 2 photographs (c) and (d)). These were recorded on a Tektronix 519 oscilloscope, using a fast biplanar photo-diode (ITT) as detector, via a glass beam-splitter placed outside the cavity.

III-3.2(d) Saturable Absorber Concentration

The dye concentration had an effect on the output power ultimately obtained from the mode-locked oscillator, and upon the shape

Threshold Voltage Versus Temperature
For The Ruby Oscillator
Temp. Of Mode-Locking Dye = 21°C

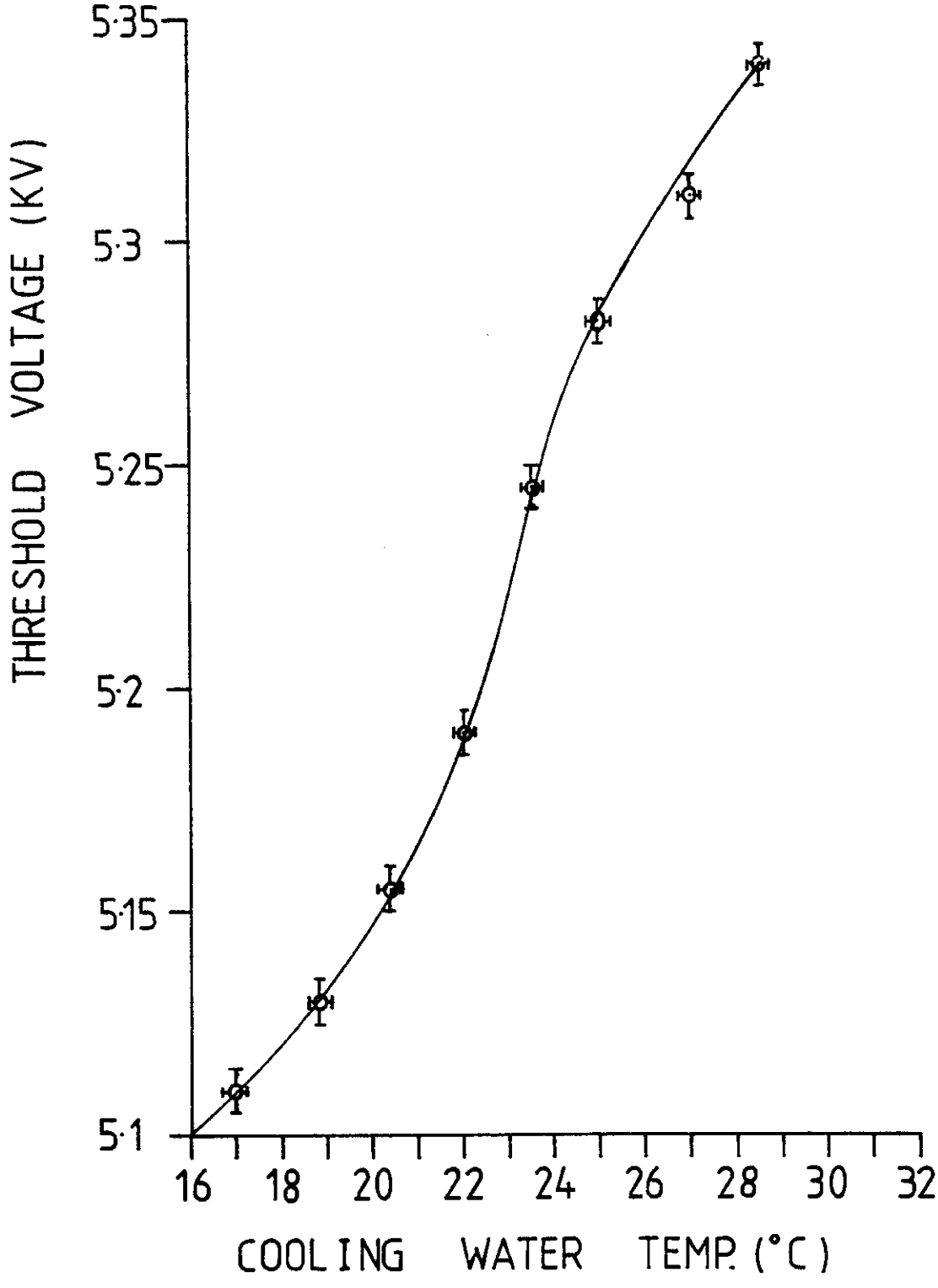

Fig 2-5

of the pulse trains. For a dye transmission (low light level) of 70%, output powers of 14-18 Mw at the peak of the pulse train were obtained. Peak powers of roughly five times this value were obtained with a dye transmission of $\sim$ 50%, but the train shape altered (see Plate 3) and the higher powers introduced non-linear effects in the later part of the train (see next section). Note photographs (c) and (d) of Plate 2 are for a dye transmission of $\sim$ 55%.

When all these precautions were followed, a high degree of reproducibility was obtained from the oscillator. Single trains of pulses occurred with a success rate of up to 90%, and peak pulse intensities were reproducible to within 25% from shot to shot. Plate 3 (photographs (c) - (f)) shows four consecutive shots to illustrate this.

Lastly, it may be pointed out that further improvement might be achieved by the use of an intra-cavity beam expanding telescope[30,42], which increases the beam cross-section at the saturable dye cell relative to that at the rod. The configuration used in this work (Figure 2-4 (a)) was such that the ruby rod was close to the output end of the cavity. Thus some benefit was derived anyway from the expansion of the beam onto the curved back mirror.

III-4 Streak Photography of the Oscillator Pulse Durations

It was necessary to ensure that the pulses observed with the photo-diode/oscilloscope combination were, in fact, properly mode-locked pulses of sufficiently high quality for use in harmonic generation experiments. The photo-diode and oscilloscope had a combined rise-time of approximately 0.5 nsec. so the measured duration was detector limited. An electron-optical streak camera (the Photocron II)

PLATE 3

Mode-Locked Trains from the Oscillator

a - Low Power Output. Saturable Dye Transmission = 70%.

b - High Power Output. Saturable Dye Transmission = 50%.

Note: A further 0.7 N.D. Filter was placed over the photodiode c.f. a.

c,d,e,f - Four consecutive shots at low power output demonstrating reproducibility finally obtained.

Vertical Scale on all photographs: 10V/cm

Timebase on all photographs: 50nsec/cm

a

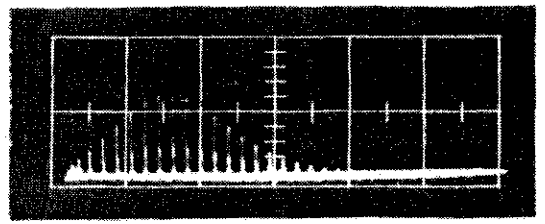

b

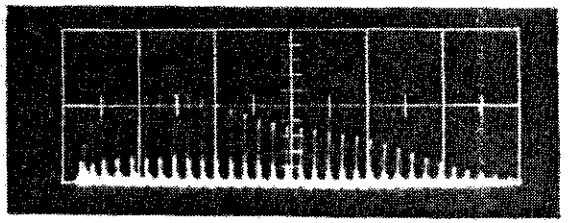

c

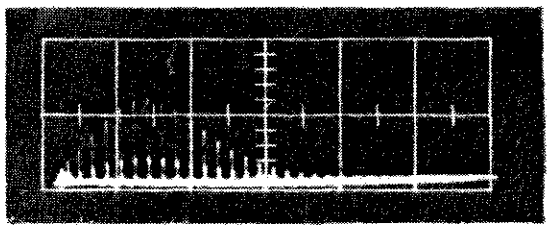

d

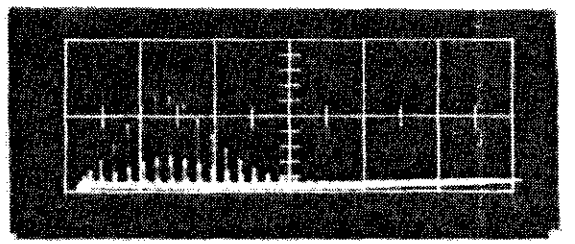

e

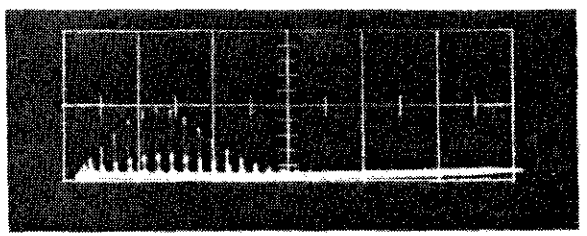

f

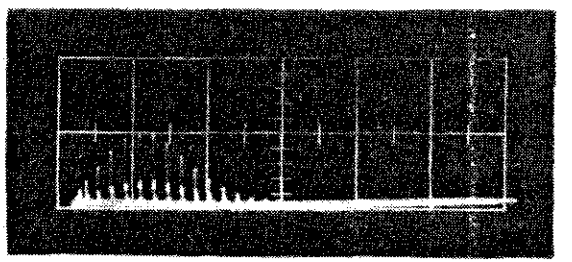

was therefore used to measure the duration of the pulses at various parts of the mode-locked train. This instrument has a time resolution of $\sim$ 1 psec, the principle limitation being transit time spread effects[26].

Figure 2-6 shows a schematic of the arrangement used for streaking. A dielectric mirror M1 (of nominally 100% reflectivity at 6943 Å) reflected the pulses from the oscillator through a beam splitter (B/S) onto an aluminium coated mirror M2. This was used to direct the pulses down an optical delay line, which consisted of three plates with parallel faces which sub-divided each pulse in intensity and so provided a means of calibrating the streak camera. The time duration between reflected pules from each one of the sets was 57 psec. After reflection from the delay line, the pulses fell onto several neutral density filters (ND) which were placed immediately in front of the input slit (S) of the streak camera (a slit width of $\sim$ 50μm was used). The function of the various labelled components in streak camera was as follows:

L_1 coupled the slit image to the photocathode (P/C) of the image converter.

M was a fine mesh, separated by $\sim$ 0.5mm from the photocathode, and set at a positive potential of 1kV. This has been shown[43] to reduce the time dispersion of the instrument.

C and A, the cone and anode respectively, acted to focus the electron image.

The reflected signal from the beam-splitter (B/S) fell onto a biplanar diode, whose resulting output was fed into a Tektronix 519 oscilloscope. By making use of the

Experimental Arrangement Used For Streaking

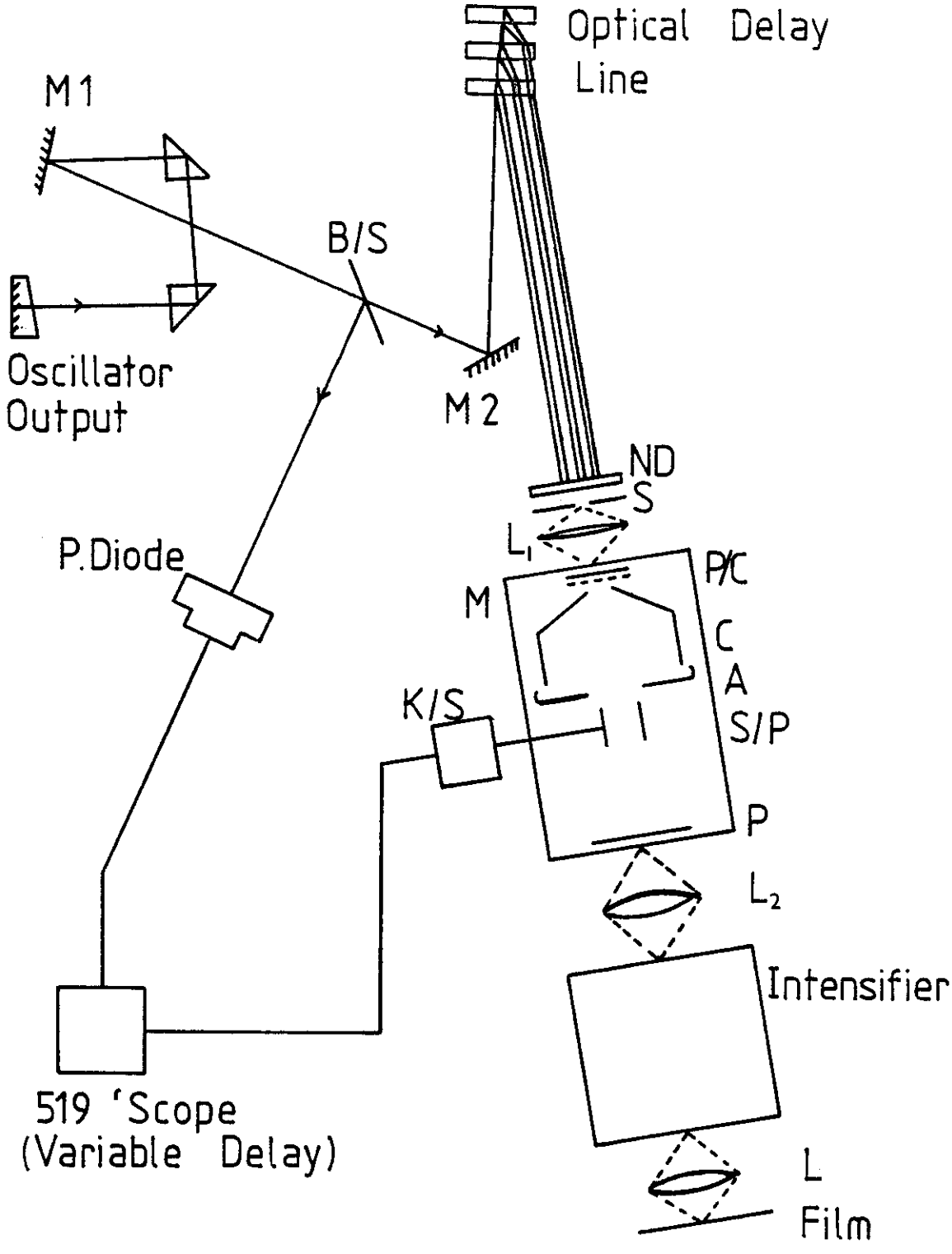

Fig 2-6

variable delay facility on these instruments, an avalanche transistor-krytron circuit (K/S) was triggered at a later time. This supplied a fast rising ($\sim$1 nsec) 5 kV signal, the central 1.5 kV of which was used as the ramp of the streak plates (S/P). Varying the delay of the signal allowed pulses in different parts of the train to be examined.

L_2 focussed the streaked image on the phosphor (P) onto the photocathode of an image intensifier. For quantitative work, Ilford type H.P.4 film was used to record the streaked image. Microdensitometer traces were subsequently taken of this film.

Two such traces are shown in Figure 2-7. The first, of a high quality, was for a pulse from the first half of the train, using a low dye concentration (70% transmission), i.e. low output power. The second, of poorer temporal quality, was for a higher dye concentration (55% transmission) and was from a pulse near the peak of the pulse train.

For low power output, the pulses in the first half of the train varied in duration from 10 psec to 30 psec, having an average length of about 20 psec. In the second half of the train, after the peak, the pulses broadened gradually to reach, on average, about 40 psec in duration. It seems likely that this was due to spectral broadening brought about by self-phase modulation, and subsequent dispersion in the active medium, which gradually broadens the pulse.

For high power output, good quality pulses were only obtained from the beginning of the train, where their durations were again about

Microdensitometer Traces (See Text)

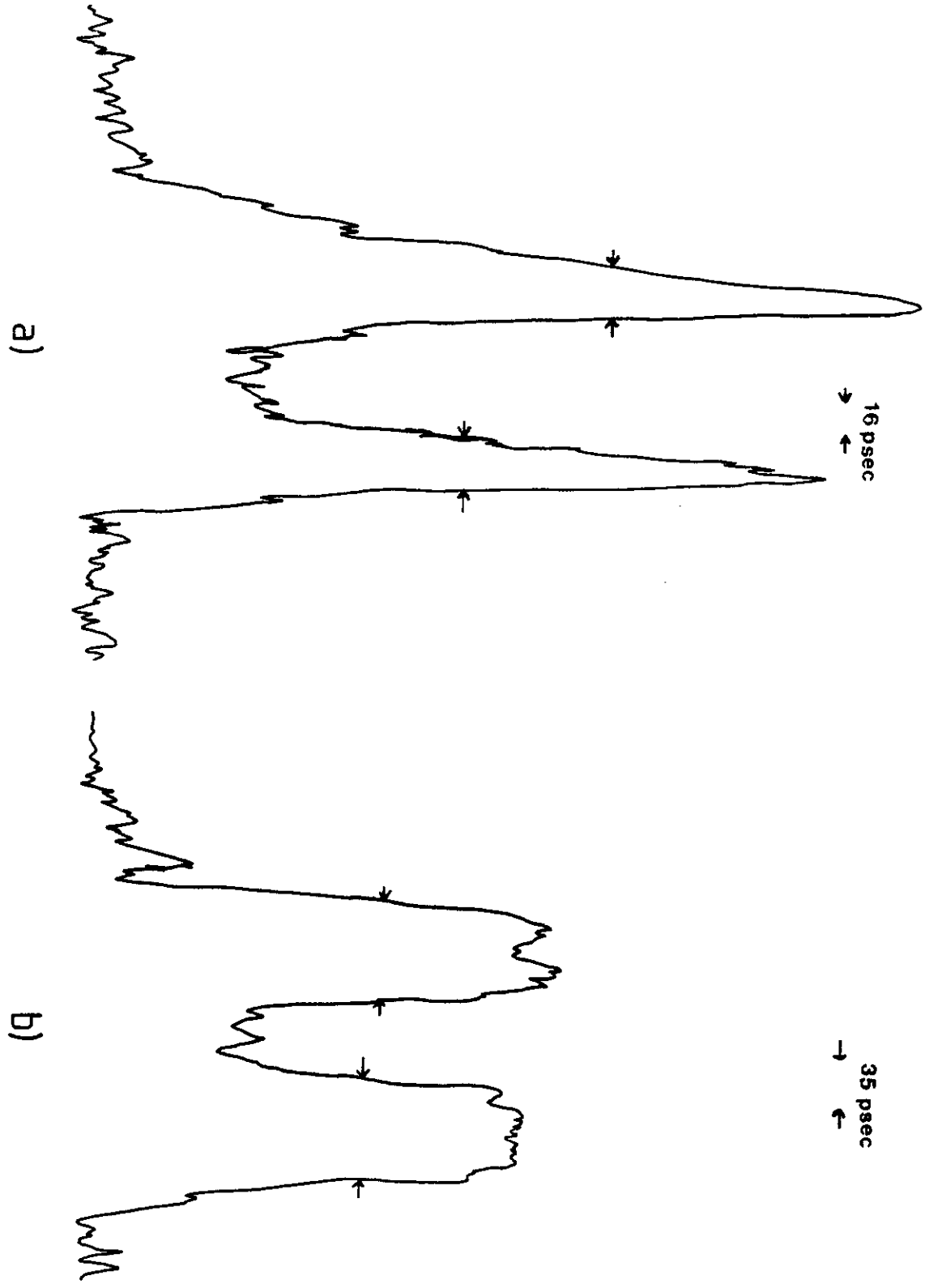

Fig 2-7

20 psec. By the middle of the train the pulse had broadened to about 40 psec, and pulses at the end of the train were longer still, typically about 60 psec.

Again this behaviour is almost certainly due to self-phase modulation, and occurs more rapidly due to the higher intensities. This is in good agreement with the results of Tashiro, Schulz-Hennig and Müller[44], who also studied the evolution of the pulse spectrum through the train. They found that at the beginning of the train, nearly bandwidth-limited pulses were produced,[a] whilst in the later parts, the spectrum broadened.[b] Temporal broadening did not occur at low power levels, however, until after the peak of the train. At high power levels, the pulse duration increased before the peak of the train, and was more severe in the latter parts.

These findings led to the use of low dye concentrations (70% transmission) in all subsequent experiments, since good quality pulses showing high spectral brightness were essential for efficient harmonic generation.

IV. Amplification

The oscillator yielded pulses with peak powers of $\sim$ 15MW (corresponding to $\sim$ 0.3 mJ per pulse). In order to increase the power, a single stage amplifier was used. The rod employed was a 9" by $\frac{5}{8}$" ruby of rather poor optical quality. Both faces of the rod were cut at Brewster's angle. This led to a marked dispersion taking place between the alignment He-Ne laser beam at 6328 Å and the ruby beam at 6943 Å, and made subsequent alignment more difficult.

The rod was mounted in a head of similar design to that used for the oscillator. A capacitor bank consisting of 20 x 38μF condensors

a) $\Delta\lambda \simeq 0.4$ Å b) $\Delta\lambda \simeq 1.2$ Å

was used, and a charging voltage of up to 6.6 kV (voltages higher than this approached the damage threshold of the flash-tube). The flashlamp was again helical, with an overall length of $\sim$ 25 cms and diameter $\sim$ 5 cms, and had a third, central, electrode which effectively produced two lamps in parallel (this reduced the RC time of the lamp and capacitor bank sufficiently to allow significant gain to build up in the rod[25]).

Because of the poor optical quality of the rod, it was found that the TEM_{oo} mode became severely distorted on passing through it, which was obviously highly undesirable for future frequency conversion experiments. By a process of trial and error, however, one position of the amplifier was discovered for which the mode quality was preserved after amplification. The beam passed down one side of the rod centre, and the system was always used with the amplifier in thisposition in subsequent experiments. The mode sizes before and after amplication are shown in Plate 6.

To produce an efficient oscillator-amplifier system, it is necessary to synchronise the firing of the two flashlamps, such that the mode-locked train from the oscillator arrives at the amplifier when its gain is at a maximum. To do this, a delay unit providing two voltage pulses separable by times from 10μsec to 10 msec was used. The amplifier was always triggered first, since the maximum of the flash lamp pulse always occurs later in this sytem due to its larger capacitance and inductance compared to the oscillator.

In order to find the optimum delay and the absolute gain of the amplifier, two diode-oscilloscope combinations were employed. These were cross-calibrated by using only the oscillator output and deflecting part of this onto the two (S1) diodes via glass beam splitters placed at 45° to the beam. The diodes were then placed to

monitor the input and output of the amplifier, their respective beamsplitters still being kept at an angle of 45° to the beam. By varying the delay for a constant pump power, the optimum delay was found. The results, as shown in Figure 2-8, indicated an optimum delay time of 0.95 msec.

With the delay set at this optimum value, the gain was determined for progressively higher pump powers, up to a maximum capacitor bank voltage of 6.6 kV. The results are shown in Figure 2-9, and give a maximum gain factor of 14($\pm$1), which enabled pulses up to 225 MW in power to be produced.

The rod was cooled by flowing distilled water over it, but it was found that the system's reproducibility as a whole was not as critically dependent upon the temperature of this cooling water as it was for the oscillator. Variations of up to 1°C could be tolerated, and for this reason a heat exchanger was found to be adequate for cooling purposes. However, the amplification achieved was severely reduced if the rod was given insufficient time to cool in between shots. A period of five minutes between shots was essential for the gain to remain the same over a "run", and often six or seven minutes were allowed.

V. Conclusions

The development of a reliable and reproducible mode-locked ruby oscillator/amplifier system has been described. By strict control of the temperature of both saturable dye and cooling water, and by voltage control on the capacitor bank, single pulse trains were observed with a 80%-90% success rate. At low output powers, the temporal form of the pulses over the first half of the train was good. Together with the good spatial TEM_{00} mode, the ruby beam was of sufficiently high quality for harmonic generation experiments to be performed.

Relative Amplification Factor

Versus Delay

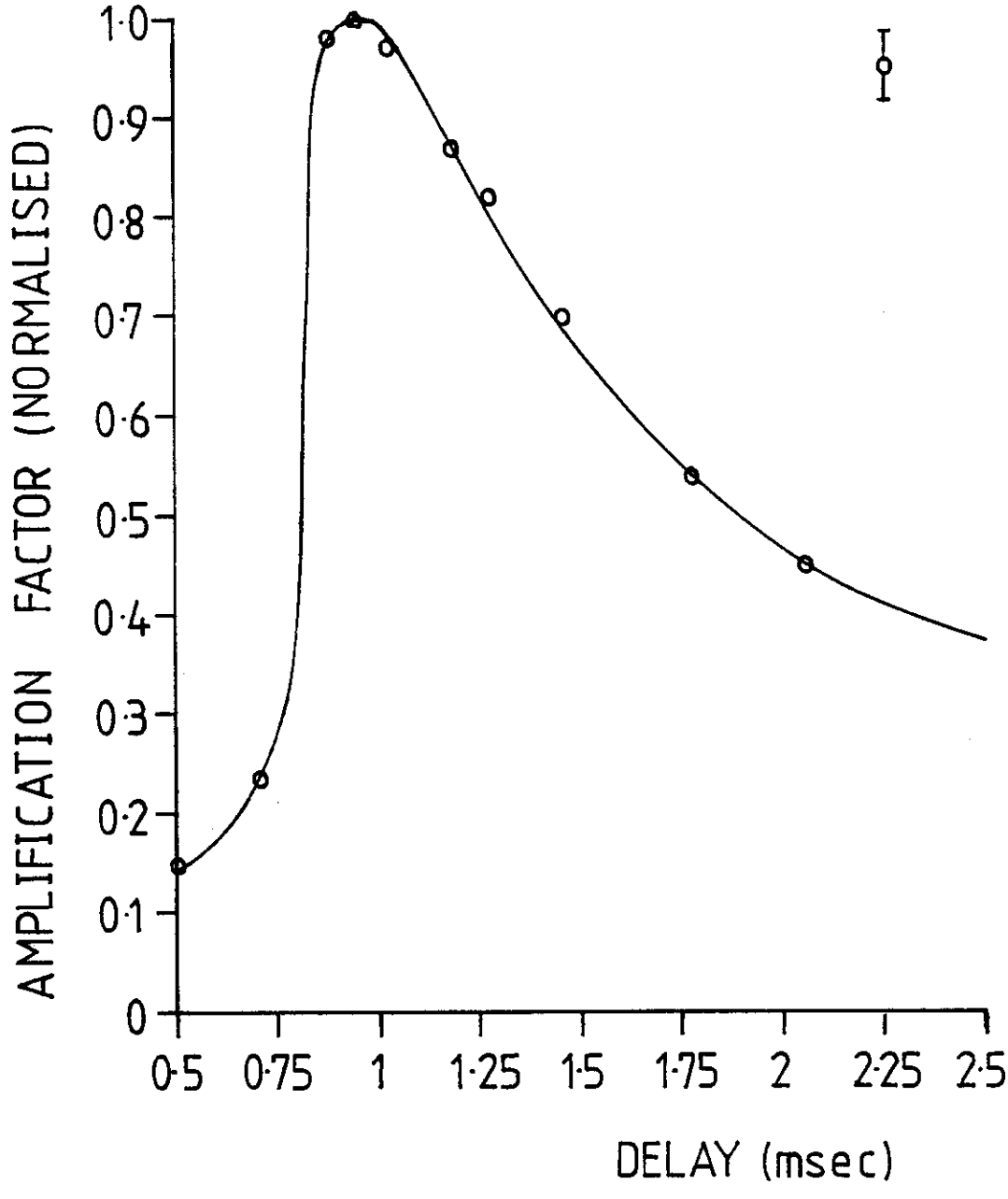

Fig 2-8

Amplifier Gain Versus Flashlamp Voltage

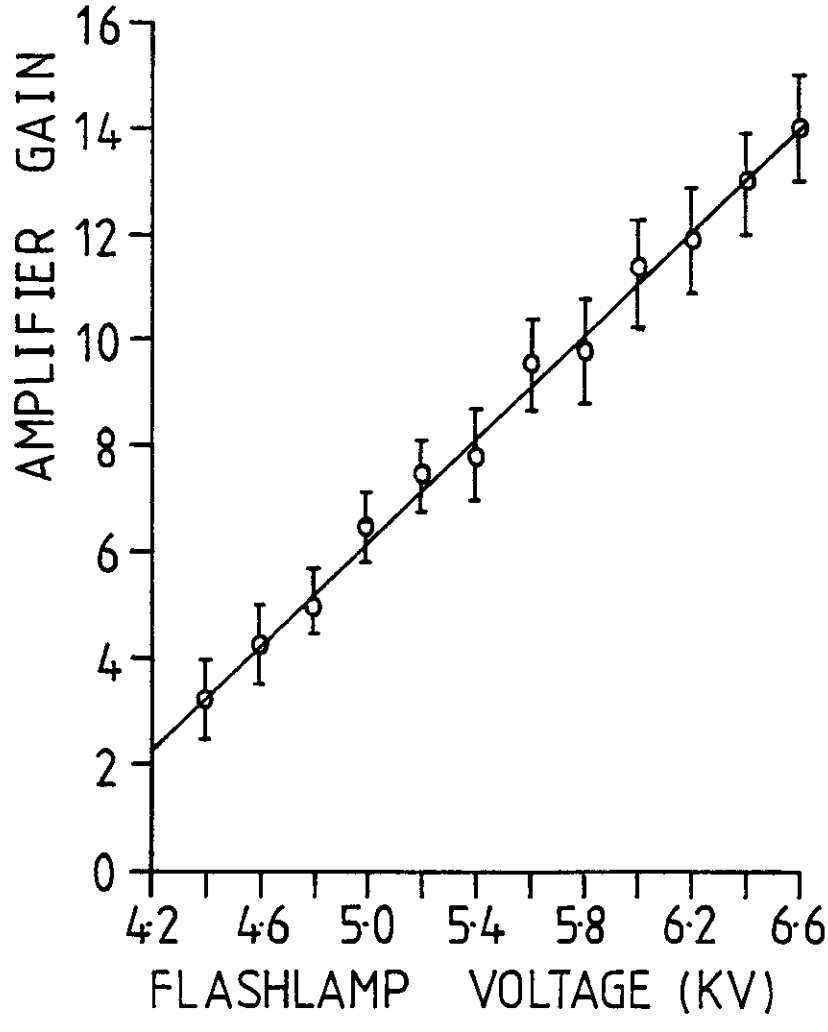

Fig 2-9

The powers obtained were $\sim$ 15 MW for a 20 psec pulse, and by using a single stage amplifier which preserved the spatial quality of the beam and exhibited gains of up to a factor of 14, pulses with powers in excess of 200 MW were finally produced.

The usefulness of this system for experiments is impaired by the very slow repetition rate which it is necessary to adopt to maintain reproducibility. With a larger cooling rate (i.e. faster water flow) it should be possible to improve this aspect of the system's performance.

CHAPTER 3

GENERATION OF SECOND HARMONIC

I. Introduction

In order to produce the fourth harmonic of mode-locked ruby in a gas, it is necessary to employ a four-wave mixing process, since an isotropic medium will not exhibit non-linear optical properties of even order. The requirement in this work, specifically, was the occurrence of the following process:

$$\omega_1 + \omega_1 + \omega_2 = \omega_4 \qquad (3\text{-}1)$$

where ω_1 = Frequency of the fundamental (ruby) wavelength

$\lambda_1 = 6943$ Å

ω_2 = Frequency of the second harmonic wavelength

$\lambda_2 = 3471.5$ Å

ω_4 = Frequency of the fourth harmonic wavelength

$\lambda_4 = 1735.75$ Å

Thus a necessary preliminary to the production of fourth harmonic was the production of a series of second harmonic pulses, coincident spatially and temporally, as far as possible, with the mode-locked train of ruby pulses. This was achieved simply by passing the ruby beam through an ADP (ammonium dihydrogen phosphate) crystal, which was angle tuned to give maximum conversion to second harmonic.

This chapter gives a brief outline of the theory of second harmonic generation, to prepare the ground for the theory of fourth harmonic generation

which is presented in detail in Chapter 4. The requirements for efficient conversion are considered. The experimental system is then described and the results are presented. Since the first demonstration of second harmonic generation in 1961[45], many types of crystals have been used in its production, and the techniques have been used extensively in laboratories throughout the world. Because of its familarity, this chapter is correspondingly brief.

II. Theory of Second Harmonic Generation

Any electric field tends to lead to a polarisation taking place in the atoms of the medium to which it is applied. The same is true when the field is electromagnetic in character. Normally the polarisation P is directly proportional to the applied electric field E, i.e.

$$\underline{P} = \varepsilon_o \chi^{(1)} \underline{E} \qquad (3\text{-}1)$$

where $\chi^{(1)}$ is the bulk linear susceptiability of the medium, and ε_o is the permittivity of free space. $\chi^{(1)}$ is related to the refractive index n by

$$\chi^{(1)} = n^2 - 1 \qquad (3\text{-}2)$$

However, when the applied fields are large, as is the case with mode-locked laser pulses (the ruby laser system delivers pulses whose electric fields are up to 10^8 V/m), the polarisation exhibits other, non-linear terms which are usually neglected for low field strengths. The polarisation, then, may be more correctly expressed as

$$P = \varepsilon_o (\chi^{(1)} E + \chi^{(2)} E^2 + \chi^{(3)} E^3 + ...) \qquad (3\text{-}3)$$

$\chi^{(2)}$ and $\chi^{(3)}$ are non-linear susceptibilities which lead to the non-linear variation, and $\chi^{(2)}$ specifically is the term responsible for second harmonic generation. This is seen simply by considering the contribution to the polarisation from this term when a sinusoidal field, $E_o \cos \omega t$ is applied:

$$P_2 = \varepsilon_o \chi^{(2)} E_o^2 \cos^2 \omega_1 t = \tfrac{1}{2}\left[\varepsilon_o \chi^{(2)} E_o^2 (1+\cos 2\omega_1 t) \right] \qquad (3\text{-}4)$$

The first term in (3-4) represents a d.c. component of the polarisation, while the cos 2ωt term represents the second harmonic production. Where the crystal concerned is isotropic, or has a centre of inversion, a reversal of the field direction leads to a reversal of the polarisation, and so even terms in the expansion (3-3) have to be eliminated. Thus second harmonic generation (S.H.G.) is only possible in non-centrosymmetric crystals.

The susceptibility $\chi^{(2)}$ is most generally a tensor, and the direction of P does not necessarily coincide with that of E. The relationship between the two may be written

$$P_i^{2\omega} = \varepsilon_o \sum_j \sum_k d_{ijk} E_j^{\omega} E_K^{\omega} \qquad (3\text{-}5)$$

where d_{ijk} is the non-linear optical coefficient of the medium. This is a third rank tensor containing 27 elements which may be simplified by following simple symmetry arguments. Since no physical significance can be attached to an exchange of E_j and E_K in (3-5), the subscripts jk may be replaced by a single symbol l. The resulting tensor d_{il} becomes a 3 x 6 matrix, which obeys the same symmetry

restrictions as the piezoelectric tensor. The number of non-vanishing elements then depends upon the point group symmetry of the medium[46]. Ammonium dihydrogen phosphate has a $\bar{4}2$ m point group symmetry, and for crystals belonging to this class, all elements of the tensor are zero except for d_{14}, d_{25} and d_{36}. Furthermore, the elements d_{14} and d_{25} are equal.

Kleinman has shown[47] that, when the non-linear polarisation is electronic in origin and the crystal is transparent throughout the frequencies encompassed by the non-linear process, further restrictions apply to the number of independent d_{ij} elements. Dispersive effects may then be neglected and the non-linear tensor becomes independent of the frequences, and hence symmetric for the interchange of any two indices. It then follows that $d_{14} = d_{25} = d_{36}$ and there is only one independent coefficient for A.D.P.

Thus a polarisation may be induced in A.D.P. which varies at twice the frequency of the applied field. If the electric field at the fundamental frequency varies as cos $(k_1 x - \omega_1 t)$, then the second harmonic polarisation varies as cos $(2k_1 x - 2\omega_1 t)$, the spatial variation of the polarisation being tied to the spatial variation of the fundamental. The second harmonic which is radiated as light has a spatial variation given by $\cos(k_2 x - 2\omega_1 t)$ where $k_2 = 2\omega_1 / v_2$, and v_2 is the phase velocity of radiation at frequency $2\omega_1$. Thus the polarisation wave and the second harmonic radiation will in general be out of step with each other, unless the refractive indices at frequencies ω_1 and $2\omega_1$ are identical.

It may be shown[46] that the second harmonic electric field generated at a point z in the crystal varies as

$$\frac{dE^{2\omega}}{dz} \propto \mathrm{Re}\{e^{i\Delta k z}\} \qquad (3\text{-}6)$$

where $\Delta k = k_2 - 2k_1$.

Summing throughout the length of the crystal, and assuming no second harmonic input ($E^{2\omega}(0) = 0$) we find

$$E^{2\omega} \alpha \int_0^L \text{Re } e\{ i\Delta kz \} \, dz$$

$$= \text{Re } \{\frac{e^{i\Delta kL} - 1}{i\Delta k}\} \tag{3-7}$$

The intensity $I^{2\omega}$ of the second harmonic at the end of the crystal is then

$$I^{2\omega} \alpha \frac{L^2 \text{ Sin }^2(\Delta kL/2)}{(\Delta kL/2)^2} \tag{3-8}$$

If Δk is not zero, the second harmonic generated at plane z_1, say, is not in phase with the second harmonic generated at a plane z_2. The resulting interference is described by the above equation (3-8). Thus a maximum intensity is obtained for a crystal length of lc, where

$$lc = \pi/\Delta k \tag{3-9}$$

or, using the relation $k^{(\omega)} = \frac{\omega n^{(\omega)}}{c}$

$$lc = \frac{\lambda_o}{4(n_1 - n_2)} \tag{3-10}$$

where lc is termed the coherence length, and

n_1 = refractive index at the fundamental frequency

n_2 = refractive index at the second harmonic frequency

λ_o = wavelength of the fundamental in vacuum

The periodic variation of the second harmonic intensity with crystal length, as indicated by Equation (3-8), was first demonstrated by Maker et al.[48]

Phase Matching

It can be seen that appreciable conversion to second harmonic may take place only if $\Delta k = 0$, or $n_1 = n_2$, for in this case the power generated should scale as the square of the crystal length (Equation 3-8). It is now an established technique[48,49] to obtain this phase matching requirement by exploiting the natural birefringence of crystals such as A.D.P. This is achieved by choosing the direction of propagation and the polarisation for the light propagating through the crystal in such a way that the fundamental ray is an ordinary ray and the second harmonic is an extraordinary ray, and

$$n_1^o = n_2^e(\theta) \tag{3-11}$$

where the superscripts o and e refer to the ordinary and extraordinary refractive indices. The point is illustrated in Figure 3-1(a). This shows the refractive index surfaces of a negative ($n_e - n_o < 0$) uniaxial crystal. The matching can be achieved for rays orientated at an angle θ_m to the optic axis, where

$$\sin^2 \theta_m = \frac{(n_1^o)^{-2} - (n_2^o)^{-2}}{(n_2^e)^{-2} - (n_2^o)^{-2}} \tag{3-12}$$

and n_2^e is the refractive index of the second harmonic extraordinary ray perpendicular to the optic axis. By rotating

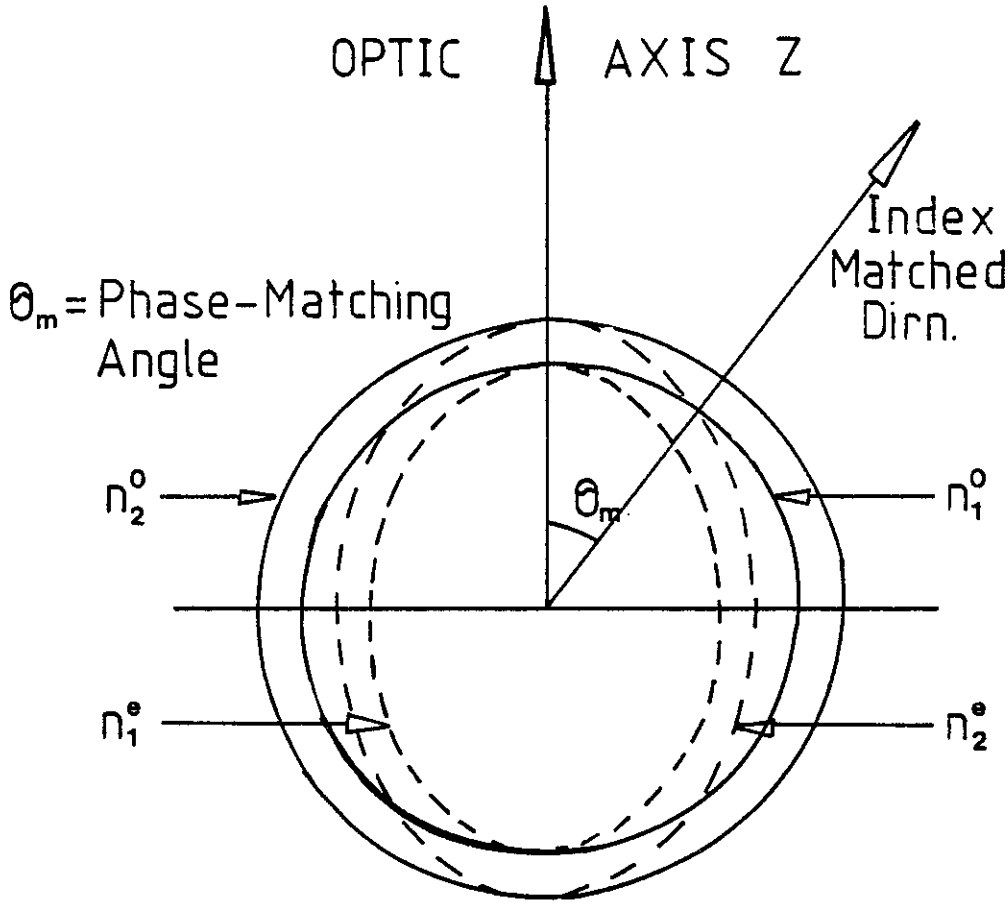
OPTIC AXIS Z
Index Matched Dirn.
θ_m = Phase-Matching Angle
n_2^o
n_1^o
θ_m
n_1^e
n_2^e

a)

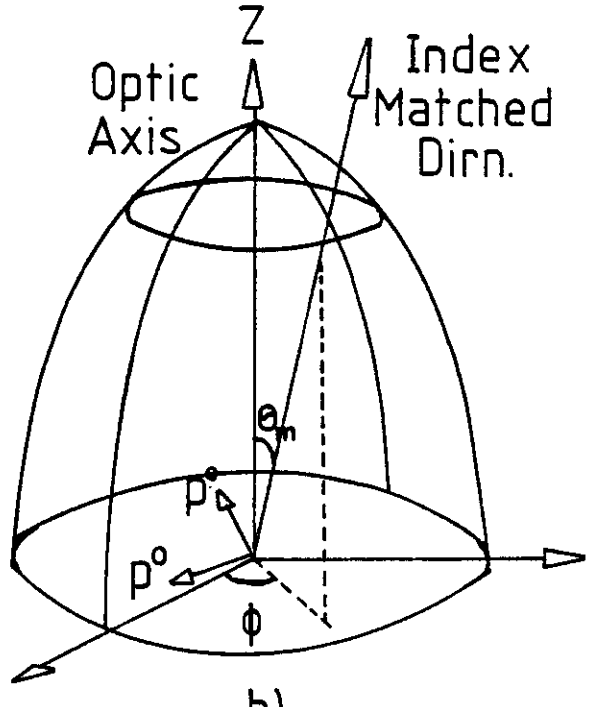
Z
Optic Axis
Index Matched Dirn.
θ_m
p^o
p^o
ϕ

b)

Fig 3-1

Figure 3-1(a) about the optic axis, an index surface is obtained, as in Figure 3-1(b), which illustrates the cone of possible phase-matched directions for the phase-matching angle θ_m. It has been shown, however, that the conversion to second harmonic is greatest for an azimuthal angle of $\phi = 45°$ [50]. Kleinman first formulated the complete expression for the second harmonic power P_2 [51]. For the plane wave case, it is given by (in MKS units)

$$P_2 = P_1^2 \left(\frac{\mu_o}{\varepsilon_o}\right)^{3/2} \frac{\omega_1^2 (d_{36})^2 L^2 \sin^2 \theta_m}{(n_1^o)^3 A} \frac{\sin^2(\frac{\Delta kL}{2})}{(\Delta kL/2)^2} \qquad (3\text{-}13)$$

Where P_1 is the fundamental power at angular frequency ω_1, and A is the beam area.

Limitations to Efficient Conversion

It has been shown [52] that the direction of energy flow, which is given by the Poynting vector, is normal to the index surface. Thus the direction of phase propagation is parallel to the Poynting vector for the ordinary wave, but deviates by an angle ρ from it for an extraordinary wave. This angle is given by [52]

$$\tan \rho = \tfrac{1}{2} (n_1^o)^2 [(n_2^e)^{-2} - (n_2^o)^{-2}] \sin^2 \theta_m \qquad (3\text{-}14)$$

When phase-matching in A.D.P., the fundamental (O ray) is undeviated, so this walk-off exhibited by the second harmonic e ray limits the effective volume over which harmonic generation may occur.

An additional loss of efficiency occurs when the fundamental beam has a finite divergence. There is an effective coherence length L_c',

beyond which the harmonic output scales as L instead of L^2, given by[53]

$$L_c' = \lambda/2\, n_1^o\, \Delta \mathrm{Sin}\, \rho \qquad (3\text{-}15)$$

where Δ is the beam divergence of the input beam at wavelength λ.

The limitations caused by walk-off may be removed by phase matching for $\theta_m = 90°$. The phase propagation direction of the second harmonic is then perpendicular to the index surface, and so colinear with the Poynting vector and the fundamental beam. This non-critical phase-matching is obtained by variation of the crystal temperature (both ordinary and extraordinary refractive indices are temperature dependent). For a wavelength of 6943 Å, however, the required temperature is too high for this method to be used [54], and angle variation must be employed for phase matching. The temperature of the crystal must be kept constant for this latter technique to be efficient. The variation of n_e and n_o at constant temperature is shown in Figure 3-2[55]. Using this and Equation (3-12) allows the phase matching angle to be determined. For a ruby laser beam, this angle is 52°.

III. Experimental Second Harmonic Generation

The ADP crystal used in this work was cut such that the ruby laser radiation normal to the input face was incident at the phase matching angle of 52°. It was assumed that type I phase matching occurred ($\omega^o + \omega^o = 2\omega^e$). The crystal measured 25 mm square in cross-section and 37 mm in length. It was mounted in a cylindrical container,

n_o And n_e Versus Wavelength
For ADP at 25°C

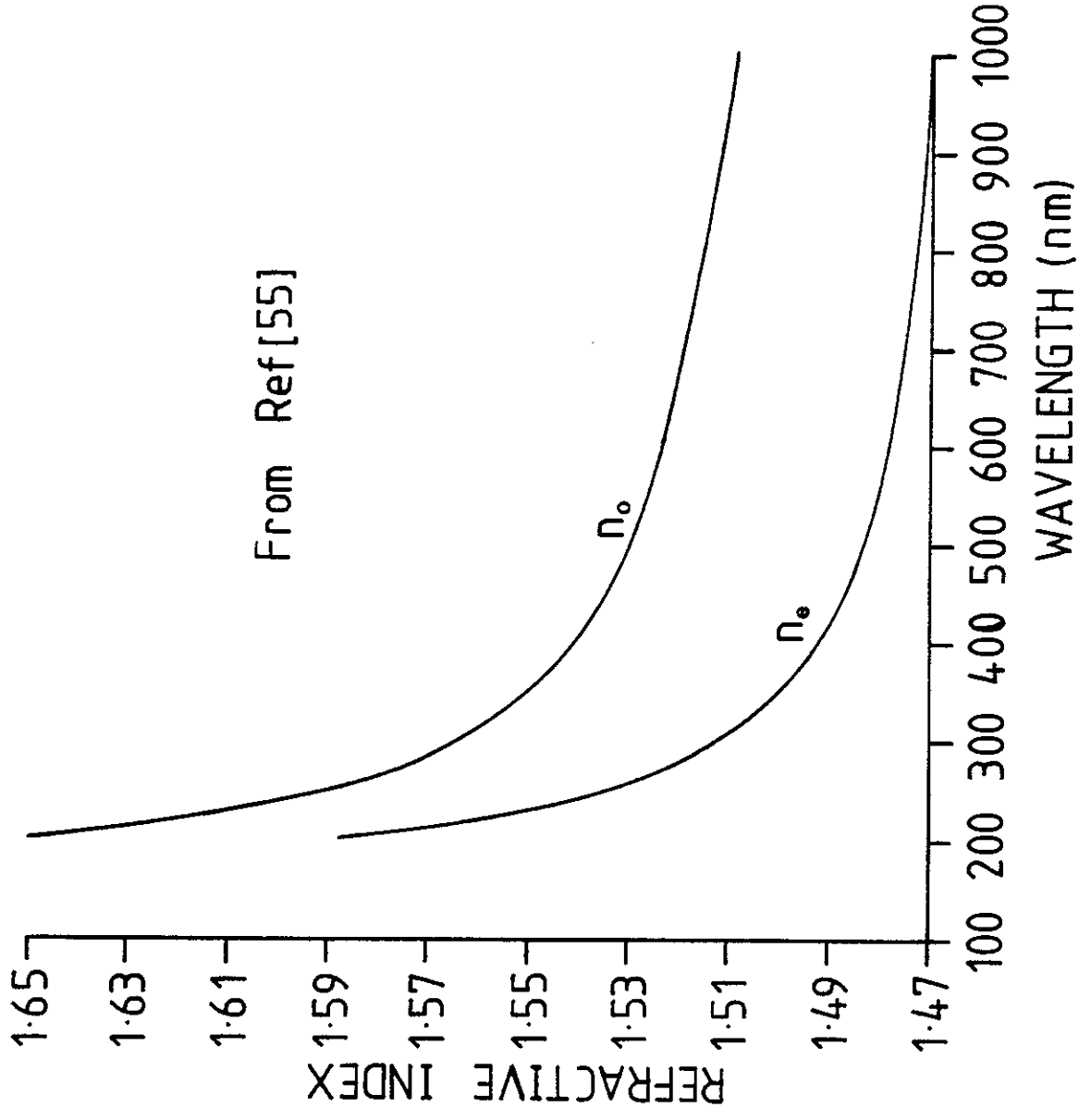

Fig 3-2

which had sealed entrance and exit quartz windows, and was subsequently filled with index matching fluid. In this way, contact of the crystal surface with air was avoided, so preventing the hygroscopic crystal from absorbing water vapour from the atmosphere. This precaution also ensured that the crystal faces were free from dust and dirt at all times. Because of the temperature dependence of the refractive indices of ADP, it was necessary to mount the container in a simple oven, whose temperature was maintained at a constant value of approdimately 35°C. This ensured that effective phase matching could take place. Fine adjustment of the crystal was afforded by the use of micrometer heads on the mounts to which the oven was attached.

The crystal was placed approximately 1 m from the output face of the ruby amplifier and the harmonic signal generated was detected on an ITT biplanar photodiode (having an S-20 photo-cathode) via a glass beam splitter and a set of filters which eliminated the fundamental radiation. These filters had a 10^{-4}:1 discrimination ratio between the ruby and second harmonic wavelengths. A sample of the incident ruby beam was also deflected by a similar beam splitter onto a fast photo-diode to monitor the fundamental intensity. Usually, two Tektronix 519 oscilloscopes were used in conjunction with the photo-diodes to give a simultaneous record of the incident and harmonic radiations, although on some occasions, a Tektronix 7904 replaced one of the 519 'scopes. The photo-diode monitoring the second harmonic was first placed to receive incident ruby light from immediately in front of the crystal. No signal was recorded, indicating that the discrimination factor of the filters was satisfactory. It was then replaced in its normal position to monitor the second harmonic output. Plate 4 shows two typical trains from the mode-locked oscillator-amplifier system and the corresponding second harmonic output. The non-linearity of the

PLATE 4

Two typical trains and their corresponding Second Harmonic (a and b)

L.H.S.		R.H.S.	
Fundamental		Second Harmonic	
Vertical Scale:	500mV/cm	Vertical Scale:	8V/cm
Timebase :	20nsec/cm	Timebase :	50nsec/cm

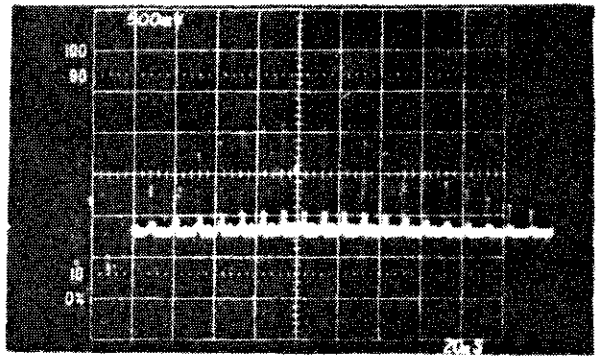

a

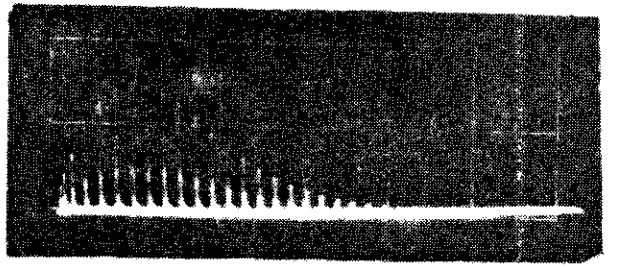

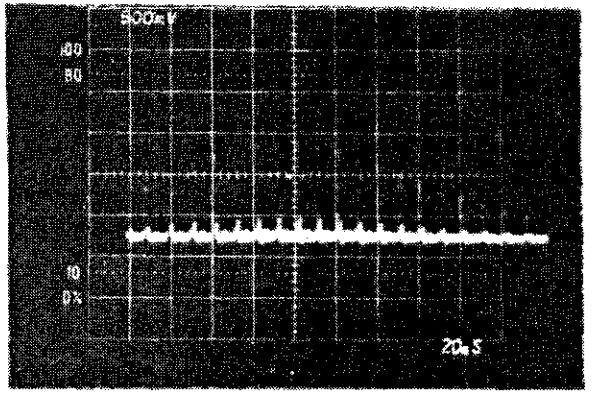

b

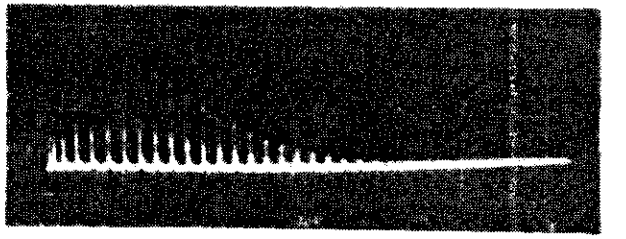

process is shown qualitatively in these photographs.

By adjusting the angle of inclination of the crystal face to the input beam a plot was obtained of relative second harmonic signal against angle, which peaked as the phase matching angle was passed through. This is shown in Figure 3-3. The variation of second harmonic power with that of the incident fundamental was also investigated, and is shown in the log-log plot of Figure 3-4. Both these graphs were in reasonable agreement with the behaviour predicted by Equation (3-13), the second harmonic showing a $(\text{sinc})^2$ dependence on the angle, and the plot of Figure 3-4 indicating a power dependence of the form

$$P_2 \propto P_1^{1.7} \tag{3-16}$$

The efficiency of conversion at the phase-matching angle was calculated to be 2%, the two photo-diodes having been calibrated [56] previously. This corresponded to an estimated incident fundamental power of 209.5 MW, and a power in the second harmonic of $\sim$ 3.5 MW. The low conversion efficiency can be accounted for by taking into account walk off and beam divergence ($\sim$ 1 m radians), which results in only a small fraction of the crystal length contributing efficiently to the harmonic generation process. It may also be noted that later pulses in the ruby train will not be phase-matched over their entire spectrum. The second harmonic falls to half its peak value at a bandwidth $\partial\lambda$ given by[57]

$$\partial\lambda = 1.39\ \lambda_1/\pi L \left[\frac{1}{2} \frac{\partial n_2^{e}}{\partial \lambda_2} - \frac{\partial n_1^{o}}{\partial \lambda_1} \right] \tag{3-17}$$

Substituting the relevant parameters into the above equation yields a value for $\partial\lambda$ of 1 Å at 6943 Å, a bandwidth to which the ruby

Relative Second Harmonic Power
Versus Angle

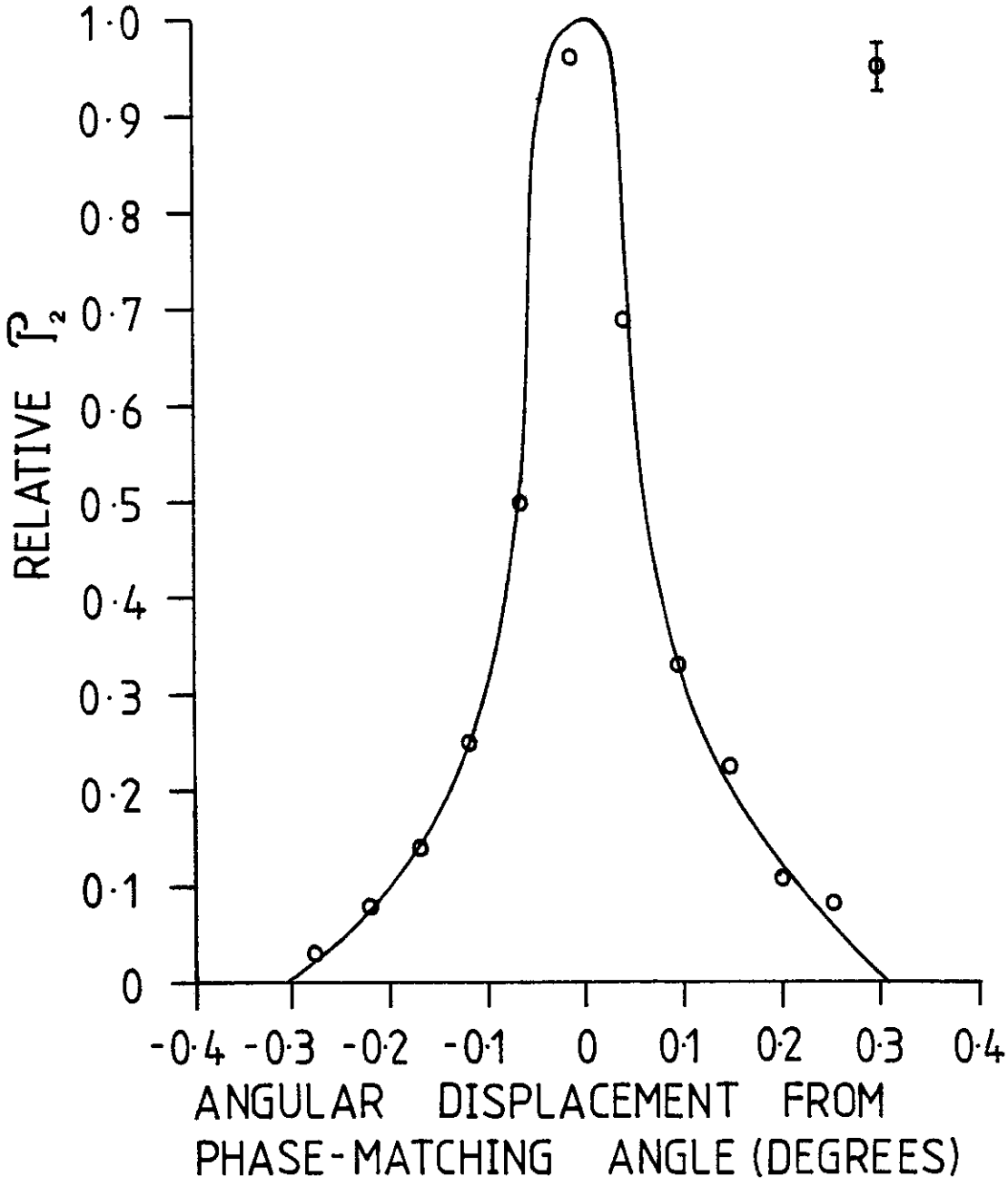

Fig 3-3

Power Dependance Of Second Harmonic On Fundamental

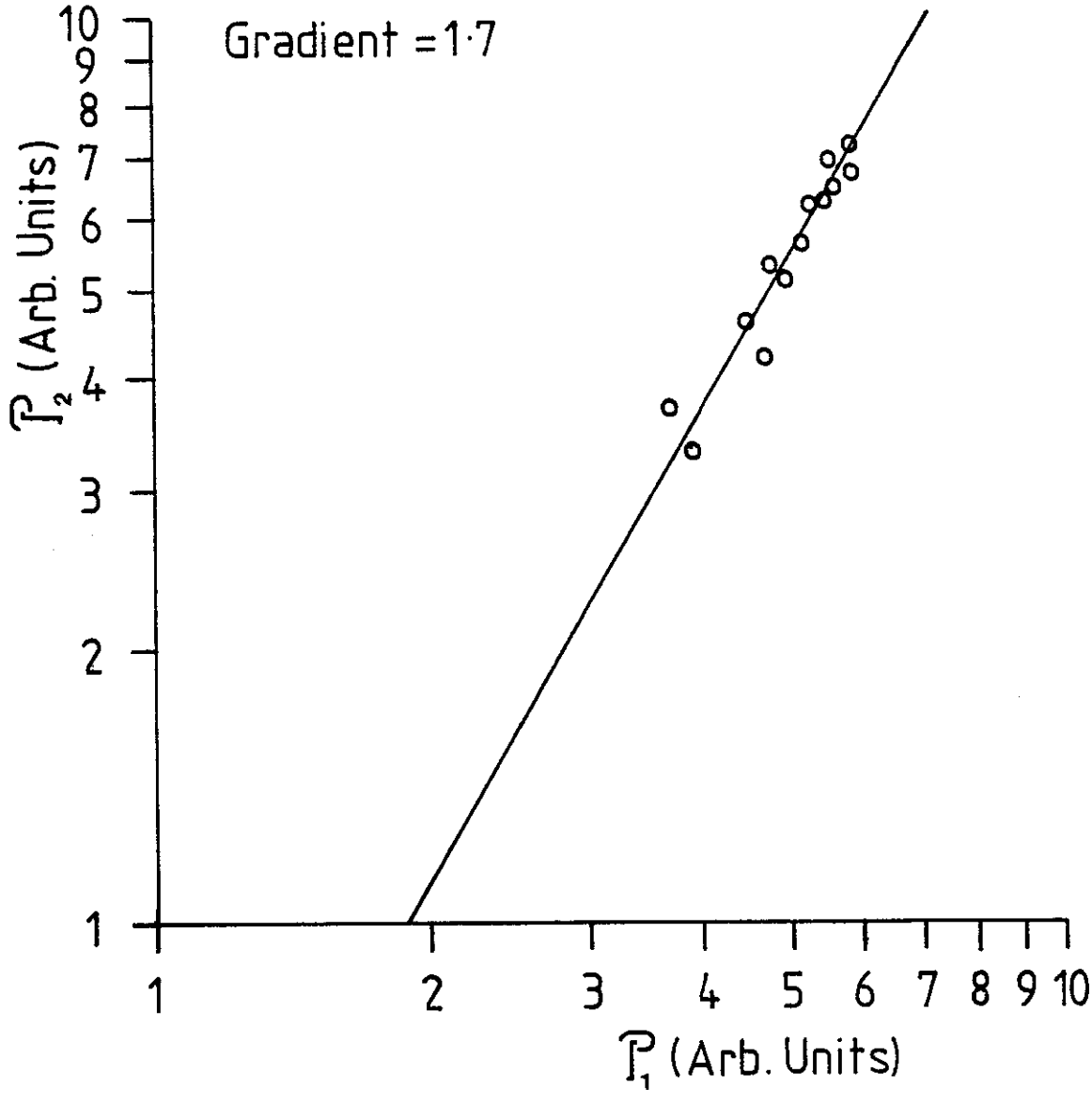

Fig 3-4

pulses have increased by the middle of the train (see previous chapter). This will lead to a decrease in the power dependency, as observed. There will also be some (small) absorption at the second harmonic frequency, as is indicated from the steeping slopes of n_e and n_o in Figure 3-2 at this wavelength. Group velocity dispersion is not an important effect at these frequencies. The second harmonic and ruby pulses will only be out of step by $\sim$ 3 psec by the time they have traversed the crystal length (the average pulse duration for the ruby pulses is $\sim$ 20 psec).

IV. Conclusion

Using a mode-locked ruby laser/amplifier system, and an A.D.P. crystal as the non-linear medium, frequency doubled trains of pulses at 3471.5 Å have been generated, with powers up to 3.5 MW. The powers obtained represent a conversion efficiency of approximately 2%, and are limited by several processes, predominantly walk-off occurring inside the crystal, and a possible failure to phase-match over the entire fundamental spectrum for the most intense pulses. These powers are sufficient, however, for use in frequency mixing experiments to generate the fourth harmonic of the ruby fundamental.

CHAPTER 4

BACKGROUND THEORY TO THE GENERATION OF FOURTH HARMONIC

I. Introduction

This chapter gives theoretical details of the method used to produce the fourth harmonic of ruby, at a wavelength of λ_4 = 1735.75 Å. A four-wave mixing process in magnesium vapour was employed, i.e.:

$$\omega_1 + \omega_1 + \omega_2 = \omega_4 \qquad (4.1)$$

where ω_1 = frequency of the fundamental (Ruby) wavelength λ_1 = 6943 Å
$\omega_2=2\omega_1$ = " " " second harmonic λ_2 = 3471.5Å
$\omega_4=4\omega_1$ = " " " fourth harmonic λ_4 = 1735.75Å

Thus, this process involves the combinations of two ruby photons with one second harmonic photon in the non-linear medium, to produce one photon at the fourth harmonic frequency.

A gaseous metalvapour was chosen since the standard non-linear crystals (ADP or KDP) are strongly absorbing at wavelengths below their cut-off at approximately 2,000 Å, so simply doubling twice in two consecutive crystals is not feasible. Metal vapours also have the advantage of higher breakdown power and energy densities than crystals, and if breakdown does occur, it does not destroy the medium. Also Poynting vector walk-off is not exhibited, since the gas is isotropic.

A four-wave mixing technique has to be employed because it is only possible for an isotropic gas to exhibit non-linear optical processes of odd order (first, third, fifth, etc.). This may be most simply

understood in terms of angular momentum considerations. In an isotropic gas, all energy levels have a well defined parity, so for each photon in the process, the selection rule $\Delta l = \pm 1$ must be obeyed. Thus only odd numbers of photons in combination are allowed.

Magnesium was the metal vapour eventually chosen since its term diagrams exhibits a near two-photon resonance for the combination $\omega_2 + 2\omega_1$, the mismatch being approximately 300 cm^{-1}, and so has a correspondingly enhanced non-linear susceptibility. It is transparent in the vacuum-ultraviolet, and, being anomalously dispersive for the frequencies chosen, can be phase matched by adding xenon (which is normally dispersive) as a buffer gas. The magnesium vapour was generated in a concentric heat-pipe oven arrangement, which will be discussed more fully later on.

Immediately after propagating through the ADP crystal, the ruby and second harmonic beams passed through a half-wave plate at 6943 Å, so that the polarisation of the ruby beam rotated through $\pi/2$, whilst the second harmonic polarisation remained unaltered.

Thus the polarisations of the two beams were rendered parallel before focussing into the Mg vapour. The incident ruby and second harmonic beams were focussed, using an achromatic doublet, to the centre of the oven. This doublet ensured that the beam waists of the two incident beams were coincident.

The fourth harmonic signal was optimised by varying the partial pressure of the Xe buffer gas, which was mixed with the Mg vapour, until a maximum signal was obtained corresponding to the optimum ratio of Xe:Mg atoms for a given (constant) temperature. Fuller details of the experimental apparatus and procedure will be given in the next chapter, but a brief outline has been presented here to anticipate the model used in the theoretical description of this problem, which is

presented in the next two sections of this chapter. The first of these deals with the theory for the case of a focussed laser beam in a non-linear medium, and the second with considerations of the non-linear susceptibility for this process. Phase matching details are dealt with in the last section.

A discussion of the results obtained, as well as processes likely to limit the generation efficiency, is given in the next chapter.

II. Theory of Generation and Optimisation for the Focussed Case

The theory of third order optical processes has been studied extensively in recent years, notably by Ward and New[13], Miles and Harris[14], who first suggested using metal vapours, and more recently by Bjorklund[58]. Higher order processes have also been treated recently by Tomov and Richardson[59].

The analysis presented here follows closely that of Bjorklund's, applied to the specific case of fourth harmonic generation.

We consider the case of two focussed Gaussian beams in the non-linear medium, having the geometry depicted in Figure 4.1. These beams, at frequencies ω_1 and ω_2 are lowest order Gaussian modes propagating concentrically along the z-axis with identical waist locations and confocal beam parameters. We denote the wave-vectors of these beams in the non-linear medium by k_1 and k_2 respectively, and the electric field amplitudes by E_{10} and E_{20}. The fundamental electric field is thus

$$E(r,z,t) = \text{Re}\ [2E_1(R,z)\exp(-i\omega_1 t) + E_2(R,z)\exp(-i\omega_2 t)] \tag{4.2}$$

Kogelnik and Li[27] express $E_n(R,z)$, n = 1 or 2, as

Focussed Beam Geometry

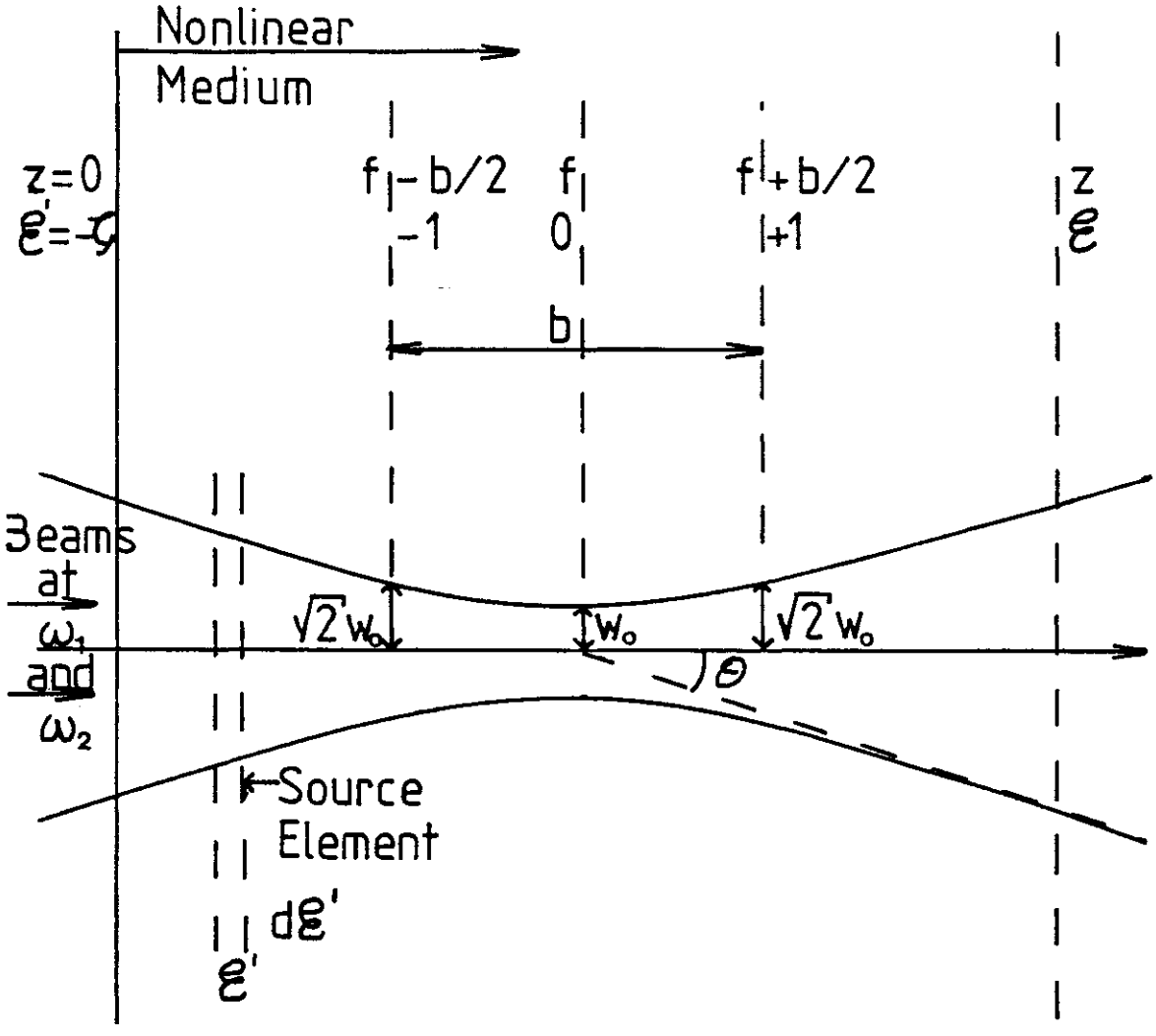

w_o = Minimum Beam Radius

$\xi = \frac{2(z-f)}{b}$ $\quad b = \frac{2\pi}{\lambda} w_o^2$

b/2 = Distance Over Which Beam Area Doubles

θ = Far-Field Diffraction Angle Of The Fundamental Mode

$= \lambda / \pi w_o$

$w(\xi) = (1+\xi^2)^{1/2} w_o$

Fig 4-1

$$E_n(R,z) = E_{no}\,\frac{w_o}{w}\,\exp\{i(k_n z - \Phi) - R^2\left(\frac{1}{w_n^2} - \frac{ik_n}{2R'_n}\right)\} \tag{4-3}$$

Where they take z as the distance measured from the beam waist, radius w_o, and

$$R = (x^2+y^2)^{\frac{1}{2}} \tag{4-4a}$$

$$w_n^2(z) = w_{no}^2\left[1 + \left(\frac{\lambda_n z}{\pi w_{no}^2}\right)^2\right] \tag{4-4b}$$

$$\Phi = \arctan\left(\lambda_n z/\pi w_{no}^2\right) \tag{4-4c}$$

$R'_n(z)$ = radius of curvature of the wavefront that intersects the axis at z.

$$R'_n(z) = z\left[1 + \left(\frac{\pi w_{no}^2}{\lambda_n z}\right)^2\right] \tag{4-5}$$

The various terms in 4-3 are explained in the following way:

The phase angle Φ represents the phase difference between the Gaussian beam and an ideal plane wave, and the factor w_o/w gives the amplitude decrease on axis due to the expansion of the beam. Note that the phase goes from $-\pi/2$ to $+\pi/2$ as z goes from $-\infty$ to $+\infty$.

The factor $\exp\left(-\frac{R^2}{w_n^2}\right)$ gives the decrease of the electric field amplitude at z with distance, R, from the axis.

Considering the form of a spherical wave from a point radiator placed at z = 0 gives us:

$$E \propto \frac{1}{R_n} \exp \{+ ikR'_n\}$$

$$= \frac{1}{R_n} \exp \{+ ik(x^2+y^2+z^2)^{\frac{1}{2}}\}$$

$$= \frac{1}{R_n} \exp \{+ ikz + \frac{ik(x^2+y^2)}{2\,R'_n}\} \quad x^2+y^2 \ll z^2 \qquad (4\text{-}6)$$

(since $z = R'_n$, the radius of curvature of the spherical wave). This explains the origin of the term $\exp\{ikR_n^2/2R'_n\}$ in (4-3).

For the geometry we have chosen in Figure 4.1, we find that the z of Kogelnik and Li[27] corresponds to our z-f, and that it is convenient to define the parameter

$$\xi = \frac{2(z-f)}{b} \qquad (4\text{-}7)$$

where f is the position of the focus along the z axis

and

$$b = \frac{2\pi}{\lambda_n} w_{no}^2 \qquad (4\text{-}8)$$

$$= \frac{4}{\theta_n^2 k_n} \qquad (4\text{-}9)$$

b is the so-called "confocal parameter".
where θ_n is the farfield diffraction angle given by

$$\theta_n = \frac{\lambda_n}{\pi w_{no}} \qquad (4\text{-}10)$$

we thus find, from (4-4b), (4-7) and (4-8), that

$$\frac{w_n}{w_{no}} = (1+\xi^2)^{\frac{1}{2}} \qquad (4\text{-}11)$$

and

$$\frac{k}{b(1+\xi^2)} = \frac{1}{w_n^2} \qquad (4\text{-}12)$$

and we may re-express $E_n(R,z)$ as *

$$E_n(r) = E_{no} \exp(ik_n z)\,(1+i\xi)^{-1}$$

$$\times \exp\{-k_n(x^2+y^2)/b(1+i\xi)\} \qquad (4\text{-}13)$$

We may justify the assumption of equal confocal parameters using the following simple argument: it is assumed that the ruby laser beam passing through the A.D.P. crystal has an approximately plane wavefront, and a beam waist radius of W. Due to the power dependence of the second harmonic, we would expect it to have a corresponding waist size of $W/\sqrt{2}$, if we neglect walk-off. The focal spot size w_{10} of the fundamental beam focused by a lens of focal length f is given by[60]

$$w_{10} = \frac{W}{\{1+(k_1^2 W^4/2f^2)\}^{\frac{1}{2}}} \approx \frac{2f}{k_1 W} \qquad f \ll \frac{k_1 W^2}{2}$$

$$= \frac{\lambda_1 f}{\pi W} \qquad (4\text{-}14)$$

Neglecting the differences in refractive index in the medium for λ_1 and λ_2, we have

---

* 1) $(1+i\xi)^{-1}$ may be written

$$(1+i\xi)^{-1} = (1+\xi^2)^{\frac{1}{2}} \exp\{-i\tan^{-1}\xi\}$$

and using 2) $\dfrac{\lambda z}{\pi w_{no}^2} = \dfrac{\pi w_n^2}{\lambda R'}$, [27]

we have $\dfrac{k\xi}{b(1+\xi^2)} = \dfrac{k}{2R'}$

$$w_{20} = \frac{\lambda_1 f}{2\pi W/\sqrt{2}} \tag{4-15}$$

$$\text{Thus } b_1 = \frac{2\pi}{\lambda_1}\left(\frac{\lambda_1 f}{\pi W}\right)^2 = b_2 = \frac{2\pi}{\lambda_1/2}\left(\frac{(\lambda_1/2)f}{\pi W/\sqrt{2}}\right)^2 \tag{4-16}$$

Thus, this assumption is seen to be a reasonable approximation to reality.

The basic approach taken within the theoretical frame-work is as follows:

1) Obtain an expression for the driving polarisation at ω_4
2) Decompose the driving polarisation into its plane-wave components using Fourier analysis
3) Calculate the harmonic radiation generated from each such component
4) Sum these individual contributions to obtain the total field.

The fundamental and generated beams are all assumed to be linearly polarised in the same direction, as we have ensured experimentally, and so we neglect the vector nature of the electric fields and the tensor nature of the non-linear susceptibility. The driving polarisation at ω_4 is given by

$$P_4(r,t) = \mathrm{Re}[P_4(r) \exp(-i\,\omega_4 t)] \tag{4-17}$$

where
$$P_4(r) = \frac{3}{4} N\epsilon_0 \chi^{(3)}(-\omega_4; \omega_1, \omega_1, \omega_2)\, E_1^2(r) E_2(r) \tag{4-18}$$

and
N = no density of atoms

$\chi^{(3)}$ = non-linear susceptibility per atom.

From Figure 4.1, we consider the non-linear medium to occupy the space where $z > 0$, and where for $z < 0$, we have vacuum. From (4-13) and (4-18)

$$P_4(r) = \frac{3}{4}\,\varepsilon_o N\,\chi^{(3)}(-\omega_4;\,\omega_1,\,\omega_1,\,\omega_2)\,E_{10}{}^2E_{20}\,\exp(ik'z)$$
$$x(1+i\xi)^{-3}\,\exp\{-\frac{k'(x^2+y^2)}{b(1+i\xi)}\}B(z) \qquad (4\text{-}19)$$

where k' is the wave-vector of the driving polarisation,

$$k' = 2k_1+k_2 \qquad (4\text{-}20)$$

and
$$B(z) = \begin{matrix} 1 & z<0 \\ 0 & z<0 \end{matrix} \qquad (4\text{-}21)$$

We now Fourier decompose $P_4(r)$ to find the amplitudes of the plane wave components of the driving polarisation. Thus the amplitude of a plane wave component with wave-vector K is

$$P_4(K) = \frac{1}{(2\pi)^3}\int_{-\infty}^{\infty} dx'' \int_{-\infty}^{\infty} dy'' \int_{-\infty}^{\infty} dz''\; P_4(r'')\exp(-i\underline{K}\cdot\underline{r}'') \qquad (4\text{-}22)$$

The total polarisation may be written

$$\underline{P} = N\varepsilon_o\chi_L\,\underline{E} + \underline{P}_{NL} \qquad (4\text{-}23)$$

χ_L = linear susceptibility

$\underline{P}_{NL}$ = non-linear polarisation

and $\underline{P}_{NL}$ = $P_4(r)$ for our case, though of course it is properly a sum over all the possible non-linear polarisations.

Maxwell's Equations read:

$$\nabla\cdot\underline{D} = 0 \qquad \nabla\cdot\underline{B} = 0$$

$$\nabla \wedge \underline{H} = \frac{\partial \underline{D}}{\partial t} = \frac{\partial}{\partial t} (\varepsilon_o \underline{E} + \underline{P})$$

$$\nabla \wedge \underline{E} = - \frac{\partial \underline{B}}{\partial t} \qquad (4\text{-}24)$$

Taking the curl of the fourth equation, we obtain

$$\nabla \wedge \nabla \wedge \underline{E}_4(K)(r) = -\mu_o \frac{\partial^2}{\partial t^2} (\varepsilon_o \varepsilon \underline{E}_4(K)(r) + \underline{P}_{NL}(r)) \qquad (4\text{-}25)$$

or

$$- \nabla^2 \underline{E}_4(K)(r) - k_4^2 E_4(K)(r) = \frac{k_o^2}{\varepsilon_o} P_4(K)(r) \qquad (4\text{-}26)$$

where k_4 = wave-vector of 4th harmonic in the non-linear medium

k_o = wave-vector of 4th harmonic in vacuum.

This has the solution[51]

$$E_4(K)(r) = \frac{ik_o^2 z}{2k_4 \varepsilon_o} \; g(U_K) \exp \{i\underline{K} \cdot \underline{r}\} \; P_4(K) \qquad (4\text{-}27)$$

where

$$U_K = iz \left[K_z - k_4 + \frac{(K_x^2 + K_y^2)}{2k_4} \right] \qquad (4\text{-}28)$$

and

$$g(x) = \left[1 - \exp(-x) \right] / x = \int_0^1 \exp[-xp] \, dp \qquad (4\text{-}29)$$

These expressions are valid for K_x, $K_y << K_z$, and $|K| - k_4 << K$.

We define the wave-vector mismatch by

$$\Delta k = k_4 - k' \tag{4.30}$$

This has the opposite sign to the convention adopted by Ward and New.

We now substitute $k_4 = k' + \Delta k$ and $p = -\frac{\frac{1}{2} b (\xi'-\xi)}{z}$ into (4-28) and (4-29), and assume $\Delta k << k_4, k'$, to find

$$g(U_K) = \frac{b}{2z} \int_{-\zeta}^{\xi} d\xi' \exp \{ib [K_z - k' + (K_x^2+K_y^2)/2k' - \Delta k] x(\xi'-\xi/2)\} \tag{4-31}$$

where $\xi = \frac{2(z-f)}{b}$ and $\zeta = 2f/b$.

The total generated field $E_4(r)$ is then found by combining all the $E_4(K)(r)$

$$E_4(r) = \int_{-\infty}^{\infty} dK_x \int_{-\infty}^{\infty} dK_y \int_{-\infty}^{\infty} dK_z E_4(K)(r) \tag{4-32}$$

$E_4(r)$ being defined by (4.27), (4.31) and (4.22).

Integrating over K_z gives the factor $\delta(Z''-z)$, and the remaining integrals are evaluated first over z", then over x", y", K_x and K_y.

The result is

$$E_4(r) = \frac{i3N}{4k_4} \quad \frac{k_o^2 b \chi^{(3)}(-\omega_4; \omega_1, \omega_1, \omega_2) E^2_{10} E_{20}}{4}$$

$$x \exp(ik'z)\,(1+i\xi)^{-1} x \exp\left[\frac{-k'(x^2+y^2)}{b(1+i\xi)}\right]$$

$$x \int_{-\zeta}^{\xi} \frac{\exp[-ib/2\,\Delta k(\xi'-\xi)]}{(1+i\xi')^2}\, d\xi' \qquad (4\text{-}23)$$

Assuming the non-linear medium to be contained in a cell of length L, and the location of the focus at Z = f it is seen, that with

$$\xi = 2(L-f)/(b) \quad \text{and} \quad \zeta = \frac{2f}{b},\ z = L,$$

equation (4-23) completely describes the amplitude of the generated field at the plane of the output window.

For the process $\omega_1+\omega_1+2\omega_1 \rightarrow 4\omega_1$, $E_4(r)$ is a Gaussian beam of lowest order mode and has the same confocal parameter and waist location as the input beams. Furthermore, $E_4(r)$ is circularly symmetric about the z-axis and the total generated power at $\omega_4(= 4\omega_1)$ is found by evaluating integrals like

$$\int_0^{\infty} 2\pi R|E_4(R)|^2 dR$$

where $R = (x^2+y^2)^{\frac{1}{2}}$ and $z = L$.

Thus we find the total generated power, P_4 to be given by

$$P_4 = \frac{1}{2}\sqrt{\frac{\varepsilon\,\varepsilon_o}{\mu_o}} \int_0^{\infty} 2\pi\, R|E_4(R)|^2 dR$$

$$= \frac{1}{2}\sqrt{\frac{\varepsilon\,\varepsilon_o}{\mu_o}}\ \frac{9N^2}{256}\ \frac{k_o{}^4 b^2}{k_4{}^2}\ \{\chi^{(3)}(-\omega_4;\omega_1,\omega_1,\omega_2)\}^2\ |E_{10}{}^2\, E_{20}|^2$$

$$x \left| \int_{-\zeta}^{\xi} \exp \left[-\frac{(ib/2)\Delta k(\xi'-\xi)}{(1+i\xi')^2} \right] d\xi' \right|^2$$

$$x \, (1+\xi^2)^{-1} \int_0^{\infty} 2\pi R \exp \left[-\frac{2k'R^2}{b(1+\xi^2)} \right] dR$$

Since $(1+\xi^2)^{-1} \int_0^{\infty} 2\pi R \exp \left[-\frac{2k'R}{b(1+\xi^2)} \right] dR = \frac{\pi b}{2k'}$

we find

$$P_4 = \frac{9}{16} \frac{N^2[\chi^{(3)}]^2\mu_o}{\pi^2\varepsilon_o} \frac{\varepsilon_4}{\sqrt{\varepsilon_2\varepsilon_1}} \frac{k_o^4 k_1^2 k_2}{k_4^2 k'} P_1^2 P_2 |I(\Delta k,\xi,\zeta)|^2 \qquad (4\text{-}24)$$

where $I(\Delta k,\xi,\zeta) = \int_{-\zeta}^{\xi} \frac{\exp\{-(ib/2)\Delta k(\xi'-\xi)\}}{(1+i\xi')^2} d\xi'$ (4-25)

Approximating the refractive indices by unity, we obtain

$$P_4 = \frac{72\pi^2N^2[\chi^{(3)}]^2 P_1^2 P_2}{c^2\varepsilon_o^2 (\lambda_1)^4} |I(\Delta k,\xi,\zeta)|^2$$

Thus the power of the fourth harmonic signal is proportional to the power of the second harmonic P_2 and to the square of the fundamental power, P_1. It is also related to the square of the modulus of the integral $I(\Delta k,\xi,\zeta)$ which is the integral defined by Ward and New (with Δk of opposite sign). In the tight focussing limit ($b/L \leq 0.1$) which is approached in the experimental configuration, b is short compared to the cell length, and the entire focal region is contained within the cell. In this case, we may take ξ and ζ to approach infinity, and the

integral may be solved analytically to obtain

$$I(\Delta k,\infty,\infty) = \pi b\Delta k \exp\left(\tfrac{1}{2} b\Delta k\right) \quad \Delta k \leqslant 0$$
$$= 0 \qquad\qquad\qquad\qquad \Delta k \geqslant 0 \tag{4-27}$$

The shape of the integral is shown in Figure 4-2a for the tight focussing limit, and the variation of the shape for differing values of b/L is also shown (Figure 4-2b). For the specific experimental configuration used, b/L was equal to 0.25,and f/L = 0.5, and so the tight focussing regime was not quite reached. However, the deviation of the expression $|I(\Delta k,\xi,\zeta)|^2$ for b/L = 0.25from the analytically derived expression above is quite small ($\sim$ 0.5) and so the following arguments may be justified using the analytic expression above.

As may be seen from Figure 4.2c,$|I(\Delta k,\infty,\infty)|^2$ is relatively unchanged as a function of $b\Delta k$ as long as the fundamental beam waist region is entirely contained within the cell. This is also the case, to within about 15%, for b/L = 0.25(see Figure 4-2d for the case with b/L = 0.3). The optimum value of $b\Delta k$ and the invariance with respect to focussing position in the tight focussing case may be explained by a simple model, which takes into account the additional phase shift caused by focussing, and which we will now consider.

If we examine Equations (4-13) and (4-18) we find that the amplitude of the driving polarisation strongly peaks in the region of the fundamental beam waists. We can define a region of significant generation as that which is bounded by values of z for which the driving polarisation falls to 10 per cent of its peak. For tight focussing, b << L, the fundamental beam waist region is located entirely within the cell, so the boundaries of the generating region may be regarded as z = f-b, and z = f+b, that is ξ = -2 and ξ = +2 .

Shape Of $F(b\Delta k, b/L, f/L)$ For Various Configurations (From Ref. [58])

$$F(b\Delta k, b/L, f/L) = |I(\Delta k, \xi, \zeta)|^2$$

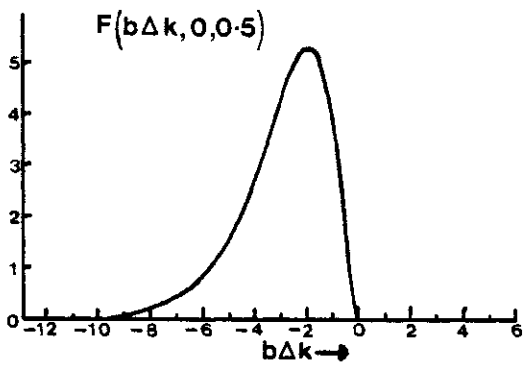

a. F versus $b\Delta k$ for $b/L \leq 0.1$, $f/L = 0.5$

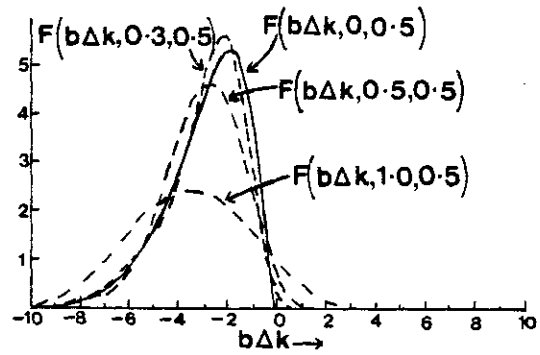

b. F versus $b\Delta k$ for $b/L = 0, 0{\cdot}3, 0{\cdot}5$, and $1{\cdot}0$, $f/L = 0{\cdot}5$

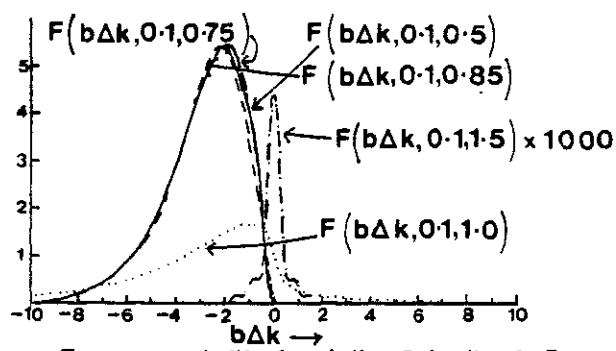

c. F versus $b\Delta k$ for $b/L = 0{\cdot}1$, $f/L = 0{\cdot}5$, $0{\cdot}75, 0{\cdot}85, 1{\cdot}0$, and $1{\cdot}5$

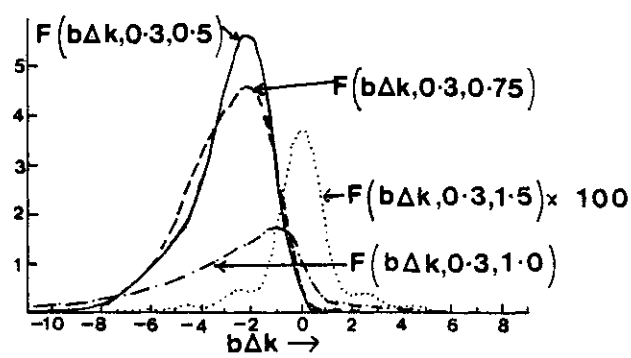

d. F versus $b\Delta k$ for $b/L = 0{\cdot}3$, $f/L = 0{\cdot}5$, $0{\cdot}75, 1{\cdot}0$, and $1{\cdot}5$

Fig 4-2

The term $(1+i\xi)^{-1}$ may be re-expressed as

$$(1+\xi^2)^{-\frac{1}{2}} \exp(-i \tan^{-1}\xi)$$

Thus the focussed T.E.M.$_\infty$ fundamental beam undergoes a shift in phase given by $\tan^{-1}\xi$ as it propagates through the waist region. The driving polarisation given by (4-18) undergoes a phase shift of $3 \tan^{-1}\xi$. The generated radiation, whose amplitude is given by (4-23), only experiences a phase shift of $\tan^{-1}\xi$. There is thus a phase slip of $2 \tan^{-1}\xi$ between the driving polarisation and the generated radiation. This slip in phase causes destructive interference between radiation generated in different parts of the generating region.

The wave-vector mismatch Δk, introduced by the dispersion of the non-linear medium, compensates to some extent for the slip in phase due to focussing. To exactly cancel the total slip in phase for the the tight focussing case (where $\xi = 2$, i.e. $\tan^{-1} \xi = 1.1$), we need a value for Δk given by

$$\Delta k_{opt} \simeq \frac{-2.2}{b} \qquad (4\text{-}28)$$

The actual optimum value of Δk which maximises the integral $I(\Delta k, \xi, \zeta)$ for the tight focussing case is

$$\Delta k = \frac{-2}{b} \qquad (4\text{-}29)$$

as may be readily derived from (4-27).

As significant generation only occurs in the generating region, the exact position of focus should have little effect on this behaviour as long as the entire generation region lies within this cell.

Thus, this simple argument leads us to the same conclusions as the rigorous theory.

Yet another approach is to consider the process from the point of view of matching moments of individual photons. For Δk negative, wave-vector match can be achieved for non-collinear plane wave components existing within the focussed fundamental beam. This is equivalent to the requirement that the momemtum of the photons taking part in the process be conserved. It is readily seen that the momenta of two fundamental photons at angles of $\theta/\sqrt{2}$ and $-\theta/\sqrt{2}$ to the beam direction, and the momentum of a second harmonic photon at zero angle are matched to the momentum of a fourth harmonic photon at zero angle to the beam direction, if $\Delta k = -\frac{2}{b}$ (see Figure 4-3).

We now turn to discussing optimisation of the total v.u.v. power for the case of tight focussing. Limiting processes such as pump depletion, absorption, breakdown, saturation, thermal defocussing and the quadratic Kerr effect are neglected for the time being, but will be discussed at a later stage. The generated power at $4\omega_1$ is then given by (4-24), and may be expressed as

$$P_4 \propto P_1^2 P_2 N^2 \chi^2 |I(\Delta k,\xi,\zeta)|^2 \qquad (4\text{-}30)$$

If we consider P_1, P_2 and χ as constants, the optimisation requires maximising $N^2 |I(\Delta k,\xi,\zeta)|^2$, and this may be achieved by varying the parameters N, $b\Delta k$, b/L and f/L. If N is independent of $b\Delta k$, b/L and f/L, we may simply maximise N to its largest possible value, and independently maximise $I(\Delta k,\xi,\zeta)$. Under tight focussing conditions, the integral $I(\Delta k,\xi,\zeta)$ reaches its maximum value for

$$b\Delta k_{opt} = -2$$

regardless of the exact values of b/L and f/L as has already been discussed.

The method of varying $b\Delta k$ experimentally is by varying Δk. By introducing another medium with negligible non-linearity but with

Matching Momenta Of Photons Participating In Fourth Harmonic Generation

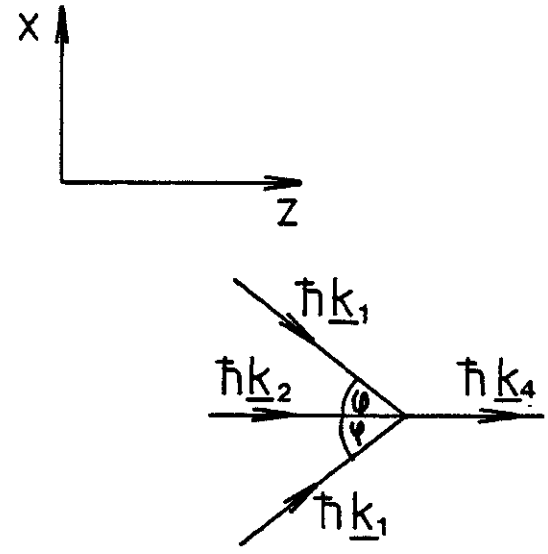

$k_1 = 2\pi/\lambda_1$, $k_2 = 2\pi/\lambda_2$, $k_4 = 2\pi/\lambda_4$, $\varphi = \Theta/\sqrt{2}$

$\Theta = \lambda_1/\pi w_{10} = (4/k_1 b)^{1/2}$

Input

Total x momentum $= \hbar k_1 \sin\varphi - \hbar k_1 \sin\varphi$
$= 0$

Total z momentum $= \hbar(k_2 + 2k_1 \cos\varphi)$
$= \hbar(k_2 + 2k_1[1 - \Theta^2/4])$ (Θ Small)
$= \hbar(k_2 + 2k_1 - 2/b)$

Output

Total x momentum $= 0$

Total z momentum $= \hbar k_4$

Momentum Conservation Requires
$k_4 = k_2 + 2k_1 - 2/b$, ie $\Delta k = -2/b$

Fig 4-3

appreciable dispersion Δk may be varied independently of N, simply by varying the concentration of the added medium.

If N is not independent of $b\Delta k$, we require a different procedure. Experimentally, this occurs if N is increased by raising the temperature of the oven, in which case Δk, being proportional to N, increases while b remains constant. Here, the quantity $(b\Delta k)^2 * |I(\Delta k,\xi,\zeta)|^2$ has to be maximised. In this case, we obtain maximum signal for

$$\Delta k = -\frac{4}{b} \qquad (4\text{-}31)$$

in the tight focussing regime. If we define the coefficient of proportionality α, such that

$$\Delta k = \alpha N \qquad (4\text{-}32)$$

$$\text{then N must be adjusted to } N_{opt} = -\frac{4}{b\alpha} \qquad (4\ 33)$$

Note that α must be negative. Further consideration of optimisation is undertaken in Section IV of this chapter.

III. Theory of the Susceptibility for Magnesium

We now turn to consider the nonlinear medium employed in the process, and give some outline to the calculation of the susceptibility.

The first general approach to the calculation of non-linear susceptibilities was given by Armstrong et al. in a classic paper published in 1962[61]. Since then many derivations have appeared and continue to do so e.g. Ducuing[62]. Butcher[63] has produced a compact formula for the general non-linear susceptibility making use of the density-matrix approach, which is used here. Very often it is possible to use the classical models of a forced harmonic and anharmonic oscillator to

describe the non-linear polarisation [64,65]. Briefly, the basis of the quantum mechanical theory is as follows; we write the electric dipole interaction V between matter and radiation as

$$V = - \underline{Q}.\underline{E}\ (\underline{r},t) \qquad (4\text{-}34)$$

Where $\underline{Q}$ is the electric-dipole-moment operator for the atom. If an atom in an unperturbed stationary state $|j\rangle$, evolves into a mixed state $|j\rangle'$, determined by time-dependent perturbation theory, the induced dipole moment $\underline{D}(t)$ is given by the expectation value

$$\underline{D} = '\langle j|\underline{Q}|j\rangle' \qquad (4\text{-}35)$$

The expectation value appears as a power series in V and thus of the applied field, and the terms may be sorted according to the powers. The macroscopic polarisation is given by

$$\underline{P}^n(\underline{r},t) = N\ \bar{\underline{D}}^{(n)} \propto N\ \chi^{(n)}\ \underline{E}^n$$

where N = no density of atoms, and the bar represents an orientation average.

The result is

$$\chi^n(-\omega_\sigma;\ \omega_1 \ldots\ \omega_n) = \frac{\zeta_T}{n!\hbar^n\varepsilon_o} \sum_{gb_1\ldots b_n} \rho(g)\ \frac{\mu_{gb_1}\ \mu_{b_1b_2}\ldots\ \mu_{b_ng}}{(\Omega_{b_1g}-\omega_1-\ldots-\omega_n)(\Omega_{b_2g}-\omega_2\ldots\omega_n)\ldots(\Omega_{b_ng}-\omega_n)} \qquad (4\text{-}36)$$

The meaning of the terms is as follows:

1) g refers to the ground state, and b_n refers to the n^{th} state

2) the transition frequencies Ω_{ij} are defined by

$$\Omega_{ij} = (E_i - E_j)/\hbar \tag{4-37}$$

where E_i and E_j are the atomic energy levels of the states $|i\rangle$ and $|j\rangle$.

3) The $\underline{\mu}_{ij}$ are matrix elements between stationary states of the unperturbed atoms

$$\underline{\mu}_{ij} = e\langle i|\underline{z}|j\rangle \tag{4-38}$$

where we assume the incident fields are linearly polarised in the z-direction, which we have ensured experimentally.

4) The summations $\sum_{g\, b_1..b_n}$ are over all of the atomic states.

5) $\rho(g)$ is the probability of occupancy of the ground state.

6) ζ_T is the overall permutation symmetry operator (Butcher[10]). This requires that the expression following it is summed over all permutations of $-\omega_\sigma, \omega_1 \ldots \omega_n$, though if some of the frequencies are equal, the number of distinct terms may be greatly reduced.

The use of diagrammatic representations is the easiest means of following all of the terms in (4-36) generated by ζ_T. Ward[66] has given a scheme for calculating the nonlinear polarisation using such diagrammatic perturbation theory.

The diagrams have obvious pictorial advantages as a notation, and lend themselves to an interpretation of the denominators in (4-36). The positive frequency $|\omega_i|$ is associated with the destruction of a photon, and the negative frequency $-|\omega_i|$ is, accordingly, associated with the creation of a photon. The denominator $\hbar(\Omega_{b_n a} - \omega_n)$ represents the net change in energy in the atom-field system as the atom undergoes the transition $a \to b_n$, and the field loses a photon of frequency ω_n through

absorption; the associated matrix element is $\mu_{b_n a}$. This may be visualised as a Raman-type process, where the states are virtual, that is, they are occupied for a time less than that determined by the uncertainty relation $\Delta E \Delta t \geq \hbar$. In this way, energy conservation is not required for the individual steps in the process, although the overall process obviously does conserve energy. Diagrammatically (4-36) becomes

$$\frac{1}{n!\hbar^n \varepsilon_o} \sum_g \rho(g) \quad \zeta_T$$

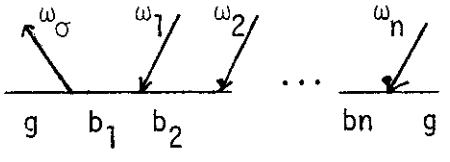

(4-39)

Where summation over the intermediate states $b_1 \ldots b_n$ is implied. A downward pointing arrow corresponds to absorption and a positive frequency, an upward pointing arrow to emission and a negative frequency. ζ_T generates the sum of all the $(n+1)!$ diagrams that result from permutations of the arrows in the diagram.

In the case of fourth harmonic generation, we are interested in the susceptibility $\chi^3(-4\omega_1; \omega_1, \omega_1, 2\omega_1)$. Figures 4-4(a) and (b) show the diagrammatic representation for this case. The ζ_T generates twelve distinct terms, each of which occurs twice from indistinguishable permutations of the ω arrows. The energy level diagrams of Figure 4-4(b) refer to the three permutations of the first subdiagram.

So the expression will read

$$\chi^{(3)}(-4\omega_1; \omega_1, \omega_1, 2\omega_1)$$

$$= \frac{2}{3!\,\hbar^3 \varepsilon_o} \sum_{gabc} \rho(g)\, \mu_{ga}\, \mu_{ab}\, \mu_{bc}\, \mu_{cg}\, A_{abc} \qquad (4\text{-}40)$$

Diagrammatic Representation Used In The Susceptibility Calculation

The Overall Sum Consists Of :-

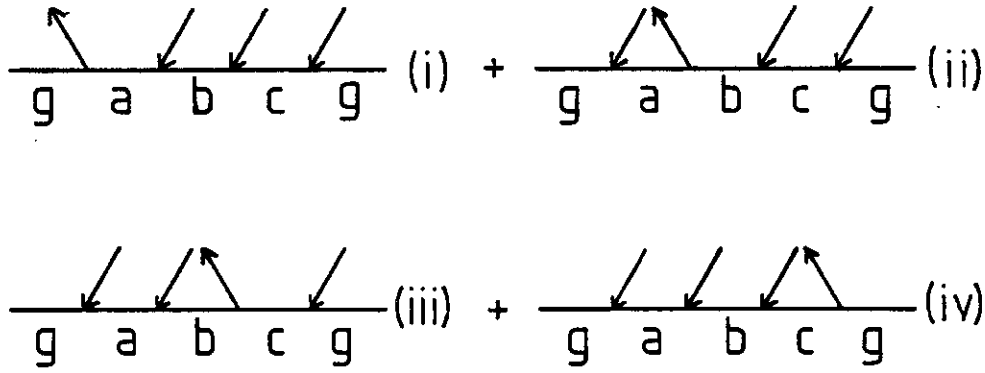

These Four Parts Are Made Up As Follows:

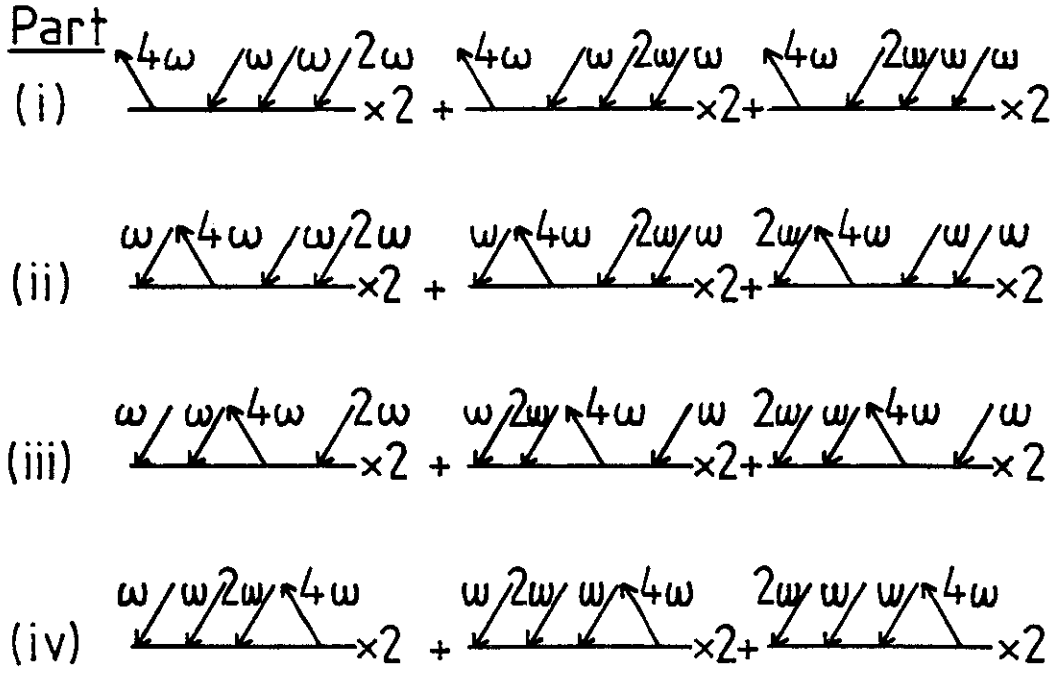

Fig 4-4(a)

Energy Level Diagram For Part(i)

Of Fig 4-4(a)

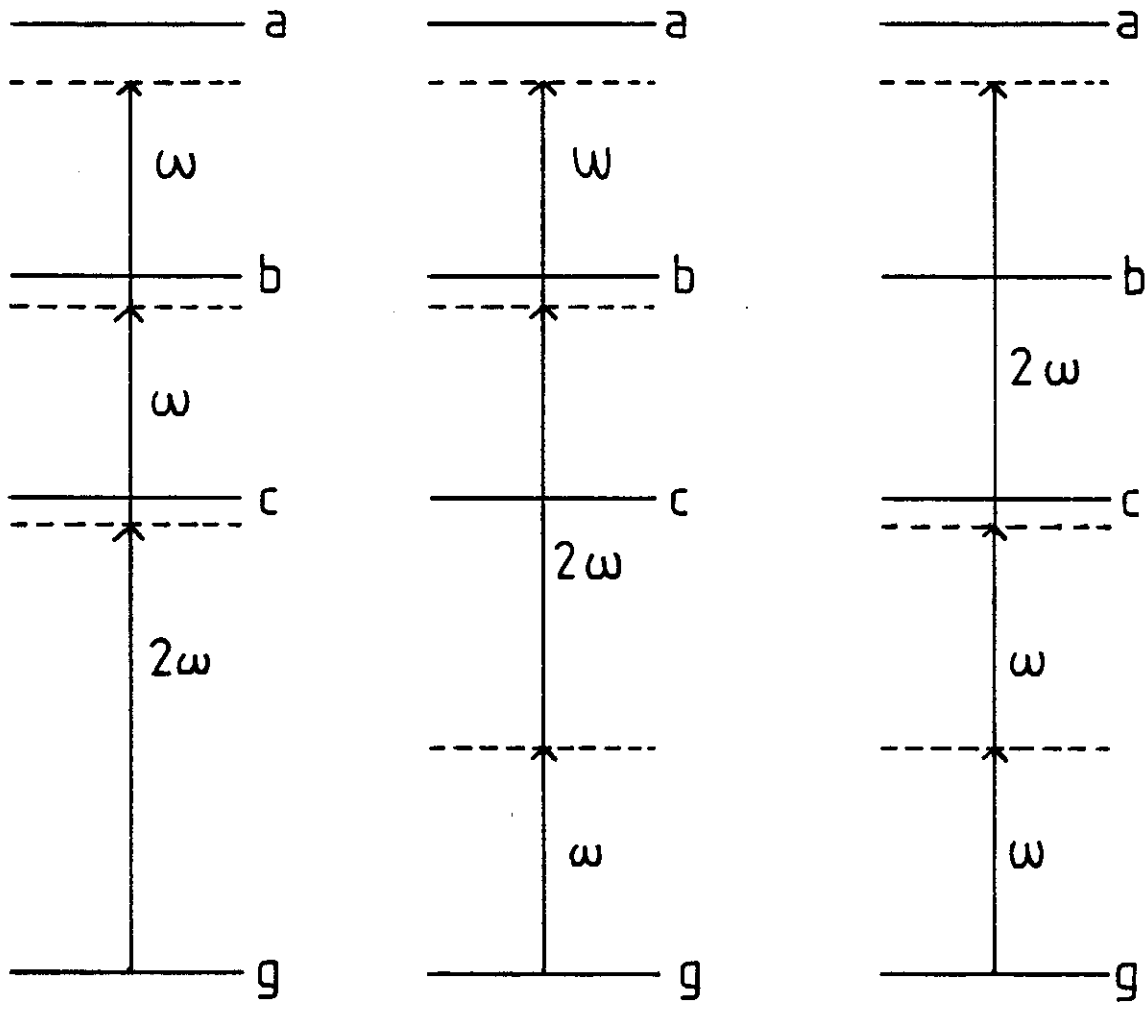

Fig 4-4(b)

where A_{abc} =

$$\frac{1}{(\Omega_{ag}-4\omega_1)(\Omega_{bg}-3\omega_1)(\Omega_{cg}-2\omega_1)} + \frac{1}{(\Omega_{ag}-4\omega_1)(\Omega_{bg}-3\omega_1)(\Omega_{cg}-\omega_1)}$$

$$+ \frac{1}{(\Omega_{ag}-4\omega_1)(\Omega_{bg}-2\omega_1)(\Omega_{cg}-\omega_1)}$$

$$+ \frac{1}{(\Omega_{ag}+\omega_1)(\Omega_{bg}-3\omega_1)(\Omega_{cg}-2\omega_1)} + \frac{1}{(\Omega_{ag}+\omega_1)(\Omega_{bg}-3\omega_1)(\Omega_{cg}-\omega_1)}$$

$$+ \frac{1}{(\Omega_{ag}+2\omega_1)(\Omega_{bg}-2\omega_1)(\Omega_{cg}-\omega_1)}$$

$$+ \frac{1}{(\Omega_{ag}+\omega_1)(\Omega_{bg}+2\omega_1)(\Omega_{cg}-2\omega_1)} + \frac{1}{(\Omega_{ag}+\omega_1)(\Omega_{bg}+3\omega_1)(\Omega_{cg}-\omega_1)}$$

$$+ \frac{1}{(\Omega_{ag}+2\omega_1)(\Omega_{bg}+3\omega_1)(\Omega_{cg}-\omega_1)}$$

$$+ \frac{1}{(\Omega_{ag}+\omega_1)(\Omega_{bg}+2\omega_1)(\Omega_{cg}+4\omega_1)} + \frac{1}{(\Omega_{ag}+\omega_1)(\Omega_{bg}+3\omega_1)(\Omega_{cg}+4\omega_1)}$$

$$+ \frac{1}{(\Omega_{ag}+\omega_1)(\Omega_{bg}+3\omega_1)(\Omega_{cg}+4\omega_1)} \qquad (4\text{-}41)$$

Since in free atoms, all states may be labelled by parity, and μ_{ij} is non-zero only for states of opposite parity, the states $|b\rangle$ and $|g\rangle$ must have equal parity. Hence, referring to the first six terms in (4.41), the susceptibility may be enhanced by choosing wavelengths such that there is a near two-photon resonance for either $\omega_1+2\omega_1$ or $\omega_1+\omega_1$.

Magnesium was chosen as the non-linear medium since it is found that the Mg 3s 4s 'S line exhibits a near two-photon resonance, having an energy corresponding to a wavenumber of 43504 cm^{-1} [68]. The wave-number for the frequency combination of $\omega+2\omega$ has a value of 43208.99 cm^{-1}, so differing by 294 cm^{-1} from the former. Thus the frequency combination lies 8.8 x 10^{12}Hz below the 3s 4s 'S line.* Figure 4.5 gives the energy level diagram of Magnesium (Mg is an atom consisting of two equivalent electrons in the $3s^2$ configuration, surrounding an inert Neon core. It thus demonstrates a Helium-like energy level structure composed of singlet and triplet states).

A two photon resonance has the advantage that there is not the limitation imposed of strong single photon absorption which would occur if we had a near single photon resonance say $\omega_1 \simeq \Omega_{ag}$, or the absorbtion of the generated radiation if we had a near three photon resonance $\omega_1+\omega_1+2\omega_1 \simeq \Omega_{ag}$. Both of these latter cases would still enhance the susceptibility.

The summation of equation (4-40) is over all possible atomic states. For two electron atoms, calculations of the matrix elements pose many difficulties, and it is simpler to use tabulated values of the oscillator strengths,[69,70] and relate these to the matrix elements, although, as will be seen, this leads to an uncertainty in their sign. Unfortunately, for magnesium, not all the oscillator strengths required are known, but an approximate value for the susceptibility may be obtained by calculating only the dominant terms in the summation. The oscillator strength is denoted by $f(\alpha\ J,\alpha'J')$, (where $\alpha\ J$ is the lower level and $\alpha'\ J'$ is the upper level) and is positive for absorption. J and J' refer to the quantum numbers for the total angular momentum in the lower and upper states, and α and α' to any other quantum numbers.

f is related to the line strengths $S(\alpha'\ J',\ \alpha J)$ by [71]

$$f(\alpha J,\alpha'J) = \frac{2m(E_{J'}-E_J)}{(2J+1)\ 3\ \hbar^2}\ S(\alpha'J',\alpha J) \qquad (4\text{-}42)$$

(M.K.S.)

---

* The bandwidth of the ruby pulses, is, at maximum $\sim$ 8 x 10^{10}Hz, so the bandwidth does not overlap with the atomic transition frequency. Under these conditions it is justifiable to use the expressions quoted for $\chi^{(3)}(-4\omega_1;\omega_1,\omega_1,2\omega_1)$ which are strictly for monochromatic light [67].

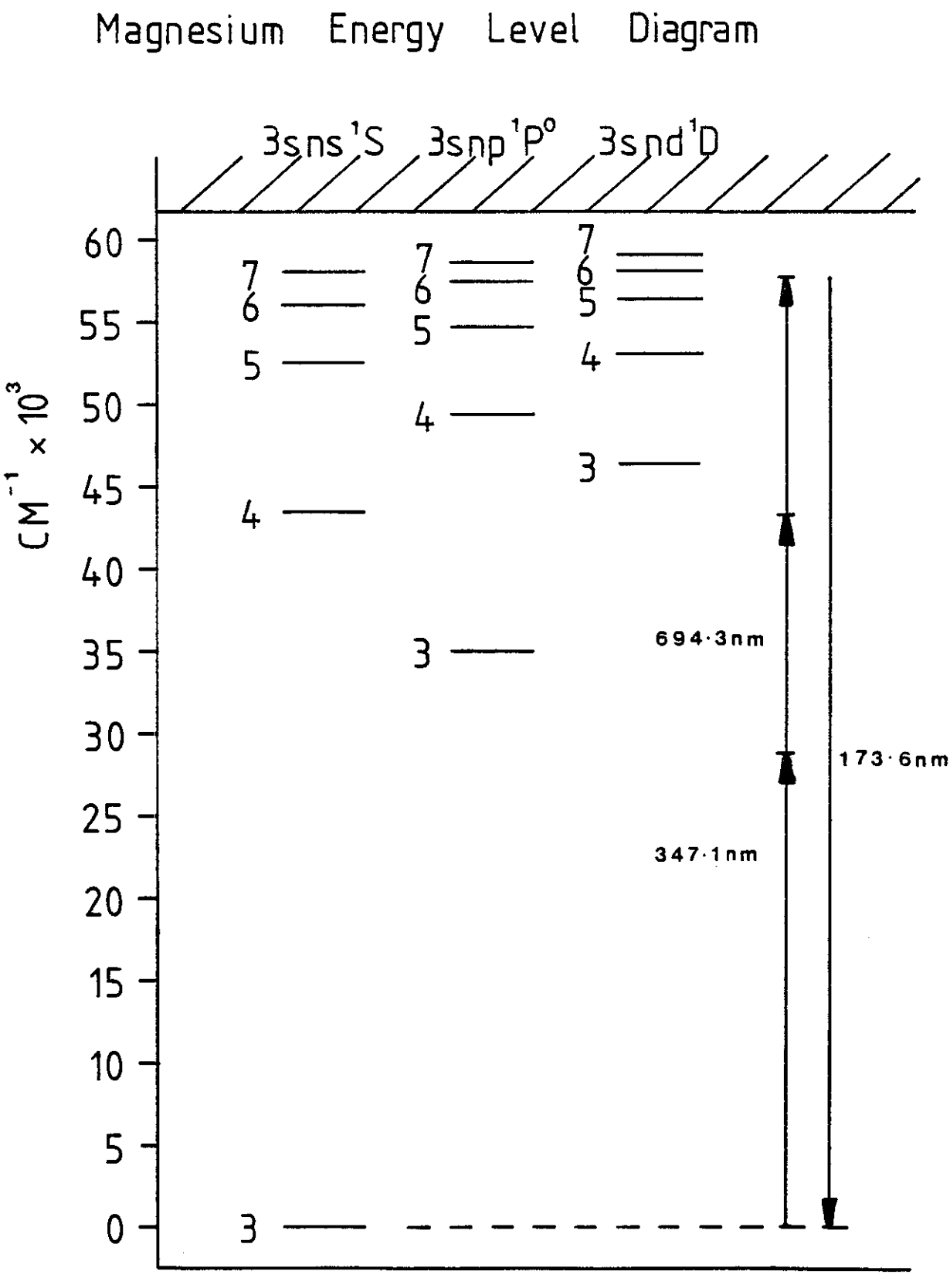
Magnesium Energy Level Diagram
3snsˡS
3snpˡP°
3sndˡD
CM⁻¹ × 10³
60
55
50
45
40
35
30
25
20
15
10
5
0
694·3nm
173·6nm
347·1nm

Fig 4-5

$S(\alpha' J', \alpha J)$ is given by

$$S(\alpha' J', \alpha J) = |< \alpha\ J\ ||\underline{Q}^{(1)}||\ \alpha'\ J'>|^2 \tag{4.43}$$

Where $\underline{Q}^{(1)}$ is, in general, a tensor operator of rank one. The matrix elements which appear in the summation (4-40) have the form

$$< \alpha\ J\ M|T^{(k)}_q|\ \alpha'\ J'M'>$$

Where $T^{(k)}_q$ represents the q^{th} component of the k^{th} rank tensor $\underline{T}^{(k)}$

By the Wigner-Eckart Theorem [72]

$$< \alpha\ J\ M|T^{(k)}_q|\alpha' J'M\ >$$

$$= (\ J'M',\ kq|JM)\ \frac{< \alpha\ J\ ||\ \underline{T}^{(k)}||\ \alpha' J'\ >}{\sqrt{2\ J+1}}$$

$$= (-1)^{J-M}\begin{pmatrix} J & k & J' \\ -M & q & M' \end{pmatrix} < \alpha\ J\ ||\ \underline{T}^{(k)}||\ \alpha' J'\ > \tag{4-44}$$

where $(J'M', kq|\,J\,M)$ is the Clebsch-Gordon coefficient and

$\begin{pmatrix} J & k & J' \\ -M & q & M' \end{pmatrix}$ is the Wigner coefficient.

Note that the Clebsch-Gordon coefficients have the property that they vanish unless

$$q = M - M' \tag{4-45}$$

For our particular case, we are interested in matrix elements like

$$< \alpha \; J M | z | \; \alpha' J' M' >$$

i.e. we have the dipole z-matrix elements only. Here, z (=rCosθ) is the zeroth component of the $\underline{r}$ vector (where θ is the angle between the z-axis and the $\underline{r}$ vector). Since a vector is a first order tensor, we have

$$\left.\begin{array}{l} k = 1 \\ \\ q = 0 \end{array}\right) \qquad (4\text{-}46)$$

and from (4-44)

$$\Delta M = M - M' = q = 0 \qquad (4\text{-}47)$$

Since we start in the ground state $^1S_0$ with M = 0, we must have M = 0 for all matrix elements, and so the Wigner coefficient becomes

$$\begin{pmatrix} J & 1 & J' \\ 0 & 0 & 0 \end{pmatrix}$$

and the sum over all values of M in Equation (4-40) vanishes. Thus our expression for the matrix element becomes

$$< \alpha \; J 0 | z | \; \alpha' J' 0 >$$

$$= (-1)^J \begin{pmatrix} J & 1 & J' \\ 0 & 0 & 0 \end{pmatrix} \langle \alpha J \| \underline{T}^{(k)} \| \alpha J' \rangle$$

$$= \pm (-1)^J \begin{pmatrix} J & 1 & J' \\ 0 & 0 & 0 \end{pmatrix} \sqrt{S(\alpha' J', \alpha J)}$$

$$= \pm (-1)^J \begin{pmatrix} J & 1 & J' \\ 0 & 0 & 0 \end{pmatrix} \sqrt{\frac{(2J+1)\ 3\hbar^2}{2m(E_{J'} - E_J)}\ f(\alpha J, \alpha' J')} \qquad (4\text{-}48)$$

We are now in a position to perform the summation in (4-40). The following approximations are used:

1) We ignore intercombination transitions singlet → triplet since the oscilator strengths for $^1S_o \rightarrow {}^3P_1$ are minute. Thus we assume LS coupling to apply.

2) As has already been discussed, the summation over M vanishes due to (4-47).

3) Only the most dominant terms in the summation are calculated. For the smaller ones, often the required oscillator strengths are untabulated anyway. The terms calculated are given in Table 4.1.

4) Due to the sign ambiguity in (4-48), there is an error in our estimate of the susceptibility since the two largest terms may add or subtract. As will be discussed later, a more consistent value with experiment is obtained if we assume that these two values subtract.

TABLE 4.1

Magnesium - Parameters for estimate of χ

$m_e = 9.1091 \times 10^{-34}$ Kg. $\quad \hbar = 1.0545 \times 10^{-34}$ J sec. $\quad c = 2.9979 \times 10^{8}$ m sec^{-1}

$\omega_1 = 2.713 \times 10^{15}$ Hz $\quad 2\omega_1 = 5.426 \times 10^{15}$ Hz $\quad 3\omega_1 = 8.139 \times 10^{15}$ Hz

$4\omega_1 = 10.852 \times 10^{15}$ Hz

$$\begin{pmatrix} 1 & 1 & 0 \\ 0 & 0 & 0 \end{pmatrix} = \begin{pmatrix} 0 & 1 & 1 \\ 0 & 0 & 0 \end{pmatrix} = -\frac{1}{\sqrt{3}}$$

Since

$$\begin{pmatrix} \ell & \ell & 0 \\ m & -m & 0 \end{pmatrix} = \frac{(-1)^{\ell - m}}{\sqrt{2\ell + 1}}$$ from Edmunds[73]

TRANSITION	f	ΔE(eV)	$\langle z \rangle$(Å)	Ω_{ig} (Hz)
$3s^2\,{}^1S_0 \rightarrow 3s3p\,{}^1P_1$	1.72	4.341	1.229	$\Omega_{cg} = 6.604 \times 10^{15}$
$3s3p\,{}^1P_1 \rightarrow 3s4s\,{}^1S$	0.18	1.047	1.403	$\Omega_{bg} = 8.193 \times 10^{15}$
$3s4s\,{}^1S \rightarrow 3s3p\,{}^1P$	0.18	1.047	1.403	$\Omega_{ag} = 6.604 \times 10^{15}$
$3s3p\,{}^1P \rightarrow 3s^2\,{}^1S_0$	1.72	4.341	1.229	

$\langle z \rangle_{ga} \langle z \rangle_{ab} \langle z \rangle_{bc} \langle z \rangle_{cg} = 2.973 \times 10^{-40}$ $\quad \sum$ Frequency Factors $= -2.63 \times 10^{-45}$

Product $= -7.82 \times 10^{-85}$

Table 4.1 (contd.)

TRANSITION	f	ΔE(eV)	<z>(Å)	Ω_{ig}(Hz)
$3s^2\ {}^1S_0 \rightarrow 3s3p\ {}^1P_1$	1.72	4.341	1.229	$\Omega_{cg} = 6.604 \times 10^{15}$
$3s3p \rightarrow 3s4s\ {}^1S$	0.18	1.047	1.403	$\Omega_{bg} = 8.193 \times 10^{15}$
$3s4s\ {}^1S \rightarrow 3s4p\ {}^1P$	1.24	0.726	2.55	$\Omega_{ag} = 9.295 \times 10^{15}$
$4s4p\ {}^1P \rightarrow 3s^2\ {}^1S_0$	0.107	6.128	0.258	

$\langle z\rangle_{ga}\langle z\rangle_{ab}\langle z\rangle_{bc}\langle z\rangle_{cg} = 1.134\times10^{-40}$ $\sum$ Frequency factors $= -11.49\times10^{-45}$

Product $= -13.03 \times 10^{-85}$

$3s^2\ {}^1S_0 \rightarrow 3s3p\ {}^1P_1$	1.72	4.341	1.229	$\Omega_{cg} = 6.604 \times 10^{15}$
$3s3p\ {}^1P_1 \rightarrow 3s4s\ {}^1S$	0.18	1.047	1.403	$\Omega_{bg} = 8.193 \times 10^{15}$
$3s4s\ {}^1S \rightarrow 3s5p\ {}^1P$	0.04	1.391	0.331	$\Omega_{ag} = 10.305 \times 10^{15}$
$3s5p\ {}^1P \rightarrow 3s^2\ {}^1S_0$	2.27×10^{-2}	6.792	0.113	

$\langle z\rangle_{ga}\langle z\rangle_{ab}\langle z\rangle_{bc}\langle z\rangle_{cg} = 0.06449 \times 10^{-40}$ $\sum$ Frequency factors $= -36.02\times10^{-45}$

Product $= -2.322 \times 10^{-85}$

$3s^2\ {}^1S \rightarrow 3s3p\ {}^1P$	1.72	4.341	1.229	$\Omega_{cg} = 6.604 \times 10^{15}$
$3s3p\ {}^1P \rightarrow 3s3d\ {}^1D$	0.28	1.4096	1.508	$\Omega_{bg} = 8.741 \times 10^{15}$
$3s3d\ {}^1D \rightarrow 3s3p\ {}^1P$	0.28	1.4096	1.508	$\Omega_{ag} = 6.604 \times 10^{15}$
$3s3p\ {}^1P \rightarrow 3s^2\ {}^1S_0$	1.72	4.341	1.229	

$\langle z\rangle_{ga}\langle z\rangle_{ab}\langle z\rangle_{bc}\langle z\rangle_{cg} = 3.435 \times 10^{-40}$ $\sum$ Frequency factors $= -0.240 \times 10^{-45}$

Product $= -0.824 \times 10^{-85}$

Assuming the above approximations to be valid, we obtain a value for the susceptibility of

$$\chi^{(3)}(-4\omega_1;\omega_1,\omega_1,2\omega_1) \simeq 6.3 \times 10^{-48} m^5 v^{-2}$$

Note that this could be written, taking into account the uncertainties in the sign, as

$$\chi^{(3)} = (6.3 + 21.2) \times 10^{-48} = 27.5 \times 10^{-48}\ m^5\ v^{-2}$$

or $$\chi^{(3)} = (6.3 - 2) \times 10^{-48} = 4.3 \times 10^{-48}\ m^5\ v^{-2}.$$

IV. Phase Matching Considerations

IV-1 Matching of Phase Velocities for constant magnesium number density

As discussed in Section II, we require (Equation 4-29)

$$b\Delta k = -2$$

for optimum conversion to fourth harmonic, assuming a constant number density of Mg, and a variable partial pressure of buffer gas. This gas is introduced as a normally dispersive medium to compensate for the anomalous dispersion of Mg at the frequencies in question, and for the experiments undertaken, Xenon was used.

We therefore require

$$k_4 - 2k_1 - k_2 = \frac{-2}{b}$$

$$\text{or} \qquad \frac{4\pi}{\lambda_1}\{\,2\,[n(4\omega_1)-1] \;-\; [n(\omega_1)-1] \;-\; [n(2\omega_1)-1]\,\} = \frac{-2}{b} \tag{4-49}$$

where n refers to the refractive index of the Magnesium vapour-Xenon gas mixture. This resultant index is found by adding the (n-1)'s of Xenon and Magnesium at the number densities relevant to each experimental configuration.

The refractive index of Mg is calculated using the standard Sellmeier equation:

$$n-1 = \frac{Nr_e}{2} \sum_i \frac{f_i}{(1/\lambda_i^2) - (1/\lambda^2)} \tag{4-50}$$

where N = no. of atoms/m^3

r_e = 2.818×10^{-15}m

f_i = oscillator strength of the i^{th} transition

λ_i = wavelength of the i^{th} transition in metres

λ = wavelength of incident light in metres

We assume that at the temperatures involved in the experiment ($\sim$ 700°C) only the ground state of Mg is populated and so only $3s^2\,{}^1S_o \rightarrow 3sn'p\,{}^1P^o_1$ ($n' \geq 3$) transitions are considered.

Table 4.2 gives the relevant f_i and λ_i. The oscillator strengths are taken from Mitchells' data [70].

The refractive index of Xenon is calculated using Koch's empirical equation [74]:

$$n_{xe} - 1 \simeq \left\{ \frac{393235}{46.3012\text{-}10^{-8}/\lambda^2} + \frac{393235}{59.5779\text{-}10^{-8}/\lambda^2} + \frac{7366100}{139.8310\text{-}10^{-8}/\lambda^2} \right\} \times 10^{-8} \tag{4-51}$$

TABLE 4.2

OSCILLATOR STRENGTHS FOR Mg

Transition	n	λ_{vacuum} (nm)	f
$3s^2\ {}^1S_0$	3	285.296	1.72
$- 3snp\ {}^1P_1{}^o$	4	202.647	0.107 ± 0.0019
	5	182.793	$(12.27 \pm 0.12) \times 10^{-2}$
	6	174.780	$(8.53 \pm 0.46) \times 10^{-3}$
	7	170.706	$(4.11 \pm 0.36) \times 10^{-3}$
	8	168.341	$(2.34 \pm 0.15) \times 10^{-3}$

TABLE 4.3

REFRACTIVE INDEX VALUES FOR Xe AND Mg

Frequency	n-1 for a number density N	
	Xenon	Magnesium
ω_1	N. 2.58×10^{-29}	N. 7.34×10^{-29}
ω_2	N. 2.75×10^{-29}	N.19.65×10^{-29}
ω_4	N. 4.24×10^{-29}	-N. 5.17×10^{-29}

where, here, λ is in centimeters. This equation holds at S.T.P., so it implies a number density of Xe atoms equal to Loschmidt's number, n_L, given by

$$n_L = 2.69 \times 10^{25}\ m^{-3}$$

The approximationsto the refractive indices of Xe and Mg are given in Table 4.3.

The condition for optimum conversion may be written

$$(b\Delta k)_{mix} = (b\Delta k)_{Mg} + (b\Delta k)_{Xe} = -2 \qquad (4\text{-}52)$$

and $b\Delta k$ for each gas may be calculated using the relevant refractive index in Equation 4-49.

Using the values from Table 4.3 and taking b = 2.15 cm,

$$(b\Delta k)_{Mg} = -1.45\ N_{Mg} \times 10^{-22} \qquad (4\text{-}53)$$

$$(b\Delta k)_{Xe} = 1.226\ N_{Xe} \times 10^{-23} \qquad (4\text{-}54)$$

Thus magnesium is negatively dispersive, and there must be some number density for which

$$(b\Delta k)_{Mg} = -2 \qquad (4\text{-}55)$$

This is obviously for a number density of

$$N_c = 1.38 \times 10^{22}\ m^{-3}.$$

Below this value, $(b\Delta k)_{Mg}$ will be more positive than -2. Thus, for working conditions below this critical number density, addition

of the positively dispersive Xe gas will make the $b\Delta k$ value for the mixture yet more positive, and its optimum value of $(b\Delta k)_{mix} = -2$ will never be reached. The ratio of number densities for optimum conversion for a Mg number density $N_{Mg} \geq N_c$ is found by substituting (4-53) and (4-54) into (4-52) and rearranging, to give

$$\left(\frac{N_{Xe}}{N_{Mg}} \right)_{OPT} = 11.83 - \frac{1.63 \times 10^{23}}{N_{Mg}} \qquad (4\text{-}57)$$

See Figures 4.6(a) and 4.6(b).

The number density for magnesium is calculated from the vapour pressure. For pressures of around 1 Torr, the vapour pressure may be written [75]

$$p(\text{Torr}) \cong \exp\left[-(A/T) + B\right] \qquad (4\text{-}58)$$

where T is in Kelvin

and $A = 16953.39$, $B = 19.53$.

The vapour pressure of Magnesium as a function of temperature is plotted in Figure 4.7(a).

Assuming the perfect gas laws to apply, the density of Mg atoms is given by

$$N_{Mg} = 9.66084 \times 10^{24} \frac{p(\text{Torr})}{T} \text{ atom/m}^3 \qquad (4\text{-}59)$$

The number density of Mg atoms as a function of temperature is plotted in Figure 4.7(b).

$(b\Delta k)_{Mg}$ Versus N_{Mg}

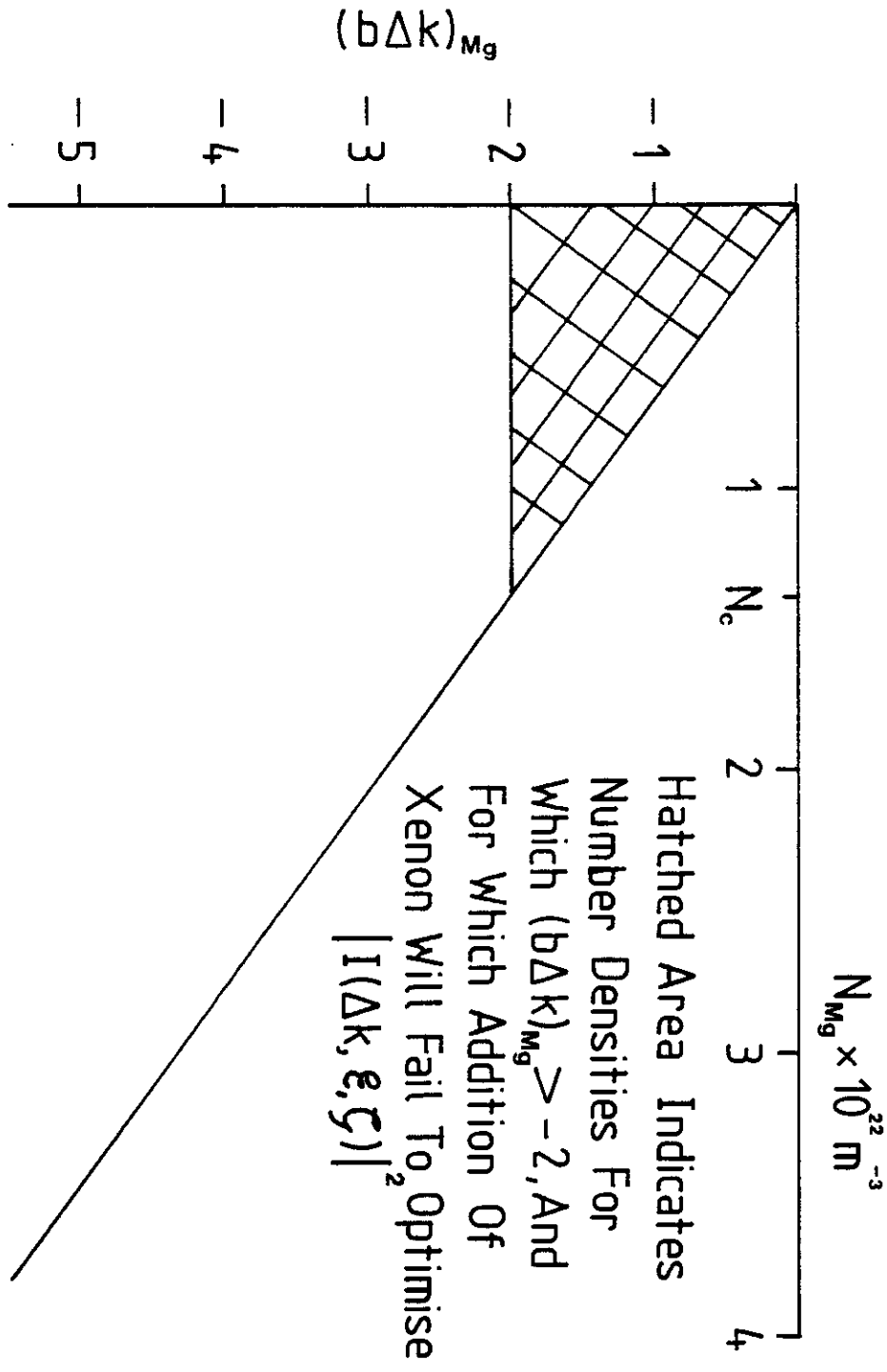

Fig 4-6(a)

Fig 4-6(b) $(N_{Xe}/N_{Mg})_{OPT}$ Versus N_{Mg}

MAGNESIUM VAPOUR PRESSURE CURVE

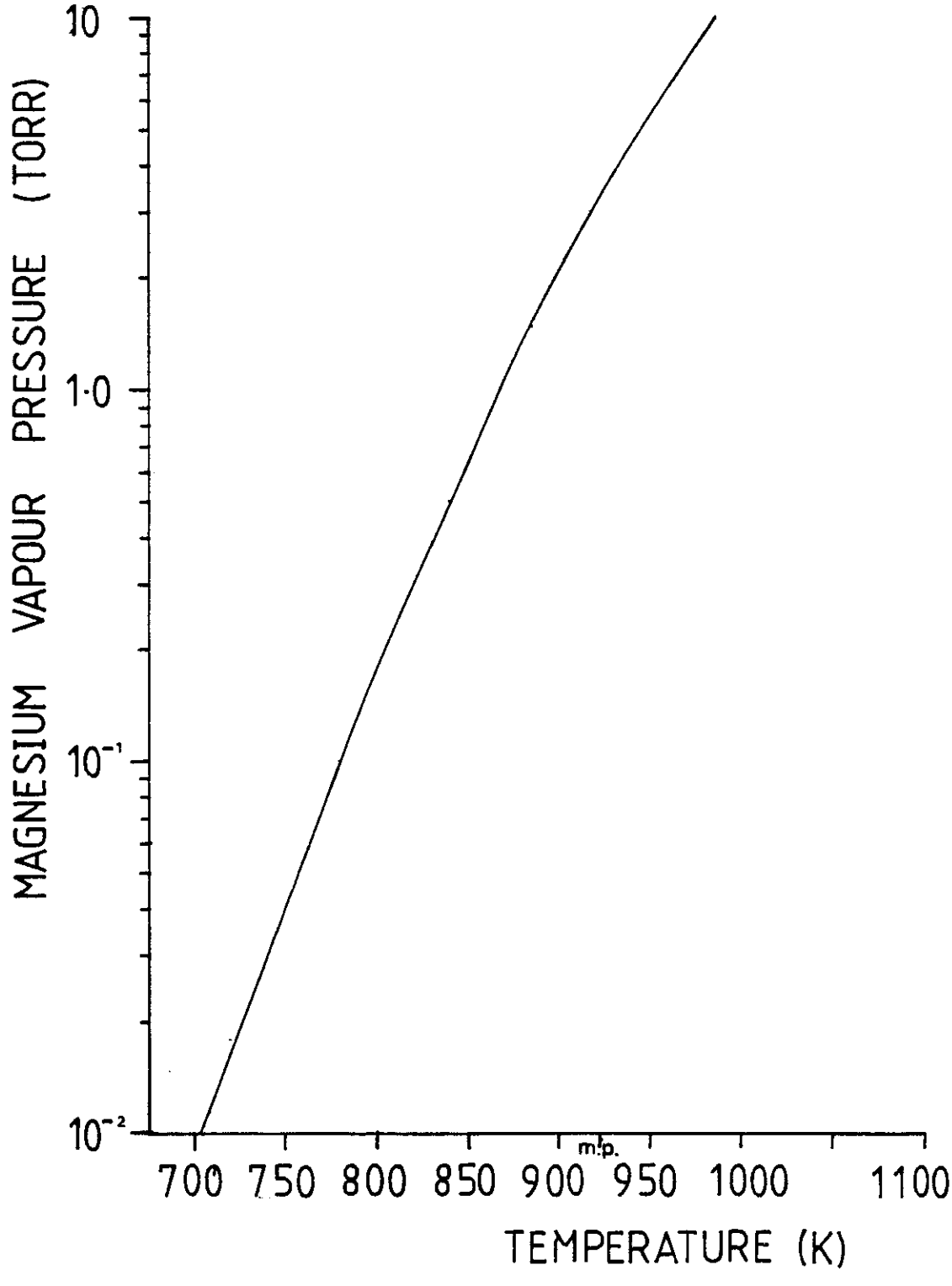

Fig 4-7(a)

N_{Mg} Versus Temperature

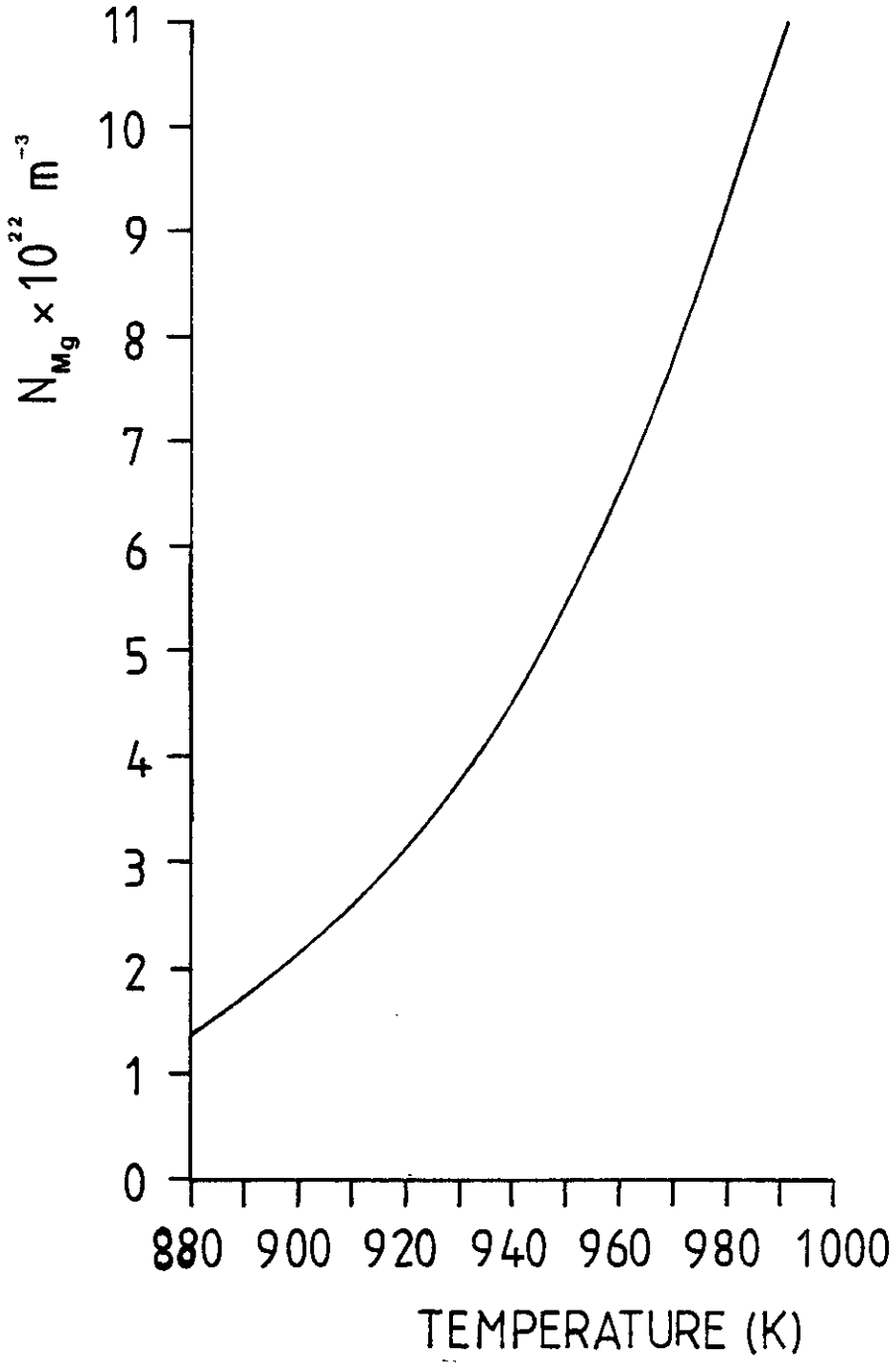

Fig 4-7(b)

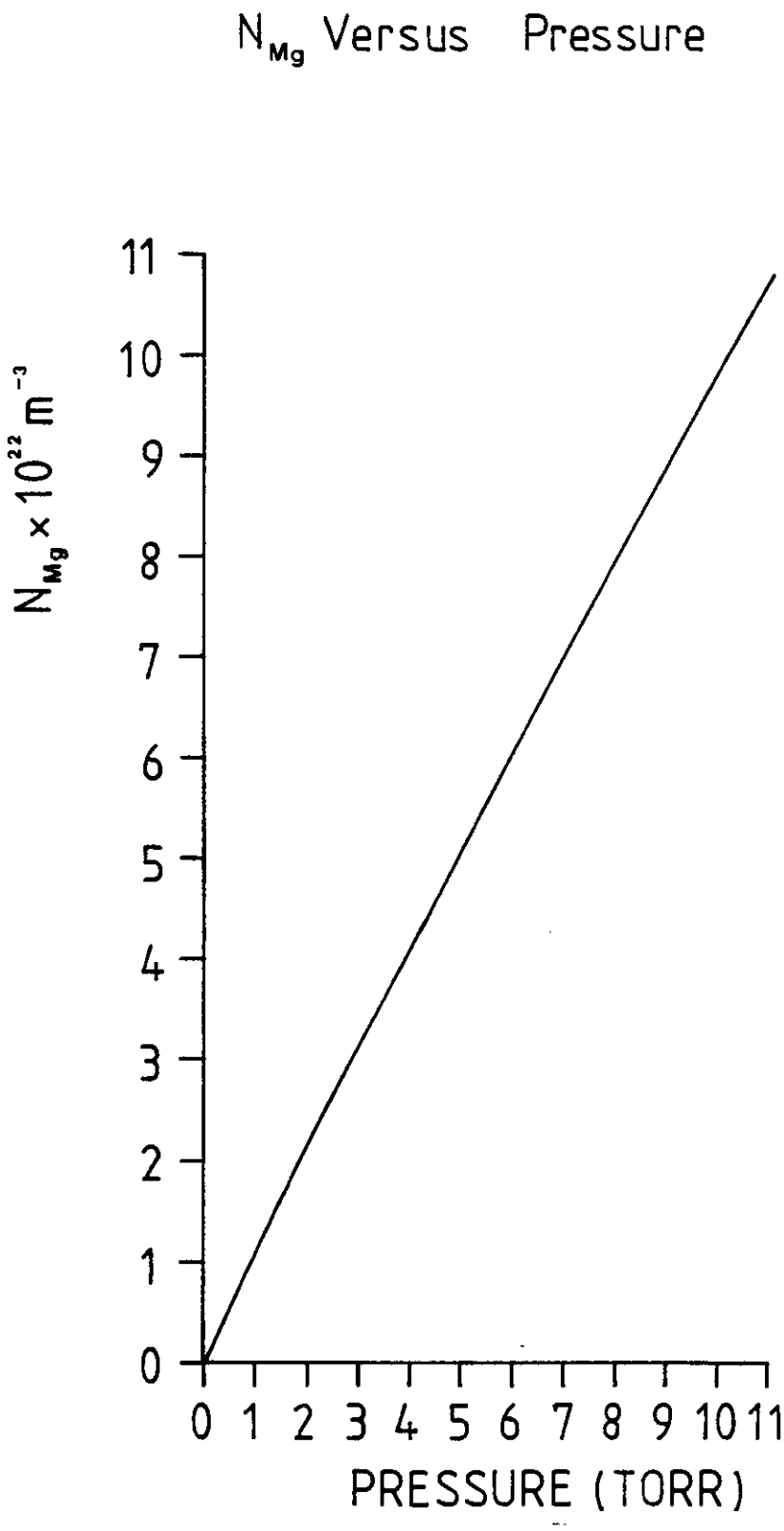
N_{Mg} Versus Pressure
$N_{Mg} \times 10^{22}\ m^{-3}$
11
10
9
8
7
6
5
4
3
2
1
0
0 1 2 3 4 5 6 7 8 9 10 11
PRESSURE (TORR)

Fig 4-7(c)

The number density of Xe atoms for optimisation at the corresponding temperature is then given by (4.57) and the partial pressure of Xe gas will be given by

$$\frac{P_o}{N_o T_o} = \frac{P_{Xe}}{N_{Xe} T_{Xe}} \qquad (4\text{-}60)$$

(Assuming perfect gas laws are valid)

Where $P_o = 760$ Torr, P_{Xe} = Pressure, $N_o = n_L = 2.69 \times 10^{25}$, N_{Xe} = Number Density } at T_{Xe}, $T_o = 273K$

This results simply in the ratio of the number densities of the two gases being equal to the ratio of their partial pressures at the temperature concerned.

From the knowledge of N_c, we find that the partial pressure of Mg below which phase matching will not occur is

$$P_c = 1.26 \text{ Torr} \qquad (4\text{-}61)$$

corresponding to a temperature of

$$T_c = 878.4K. \qquad (4\text{-}62)$$

Thus, whenever an experimental scan of relative fourth harmonic signal versus Xexon gas pressure was undertaken, it was ensured that the (constant) temperature chosen was above T_c.

IV-2 Matching of Phase Velocities for a variable magnesium number density

For the situation of a variable magnesium number density, in the absence of xenon buffer gas, we must satisfy the condition of

Equation (4-31), i.e.

$$b\Delta k = -4$$

as previously discussed. The situation is achieved experimentally by having magnesium alone in the oven, and varying the oven temperature.

Normally, however, some Xe was bled into the oven at room temperature before the beginning of the experimental run. This ensured Mg vapour did not coat the input and output windows of the oven. It is a simple matter to calculate the xenon number density present at the temperature at the beginning of the experiment. This temperature, typically, is at about 880°K. The temperature was normally taken up to about 980°K at most, so the variation of xenon number density will only be about 10%. Assuming then, a constant xenon number density, we have

$$(b\Delta k)_{mix} = (b\Delta k)_{Mg}+(b\Delta k)_{Xe} = - B\, N_{Mg}+ (b\Delta k)_{Xe} \quad (4\text{-}63)$$

where $B = 1.45 \times 10^{-22}$

and $(b\Delta k)_{Xe}$ is constant for change in N_{Mg}.

The electric field at the fourth harmonic frequency is then

$$E_{4\omega} \alpha N_{Mg}\chi^{(3)}E_{10}{}^{2}E_{20}\, I(\Delta k, \infty,\infty) \quad (4\text{-}64)$$

$$\alpha \left[\frac{-(b\Delta k)_{mix}+(b\Delta k)_{Xe}}{B}\right] I\,(\Delta k,\infty,\infty)\, E_{10}{}^{2}E_{20} \quad (4\text{-}65)$$

and the quantity to be maximised w.r.t. $(b\Delta k)_{mix}$ is

$$\left[\frac{(b\Delta k)_{Xe}-(b\Delta k)_{mix}}{B}\right] \pi(b\Delta k)_{mix} \exp\{\tfrac{1}{2}(b\Delta k)_{mix}\} \quad (4\text{-}66)$$

The resultant expression for $(b\Delta k)_{mix}$ corresponding to maximum conversion is

$$(b\Delta k)_{mix}^{OPT} = \frac{(b\Delta k)_{Xe} - 4 \pm [16 + (b\Delta k_{Xe})^2]^{\frac{1}{2}}}{2} \qquad (4\text{-}67)$$

We note that for no xenon present, $(b\Delta k)_{Xe}$ is zero, and the formula gives

$$(b\Delta k)_{mix}^{OPT} = -4,0 \text{ for } (b\Delta k)_{Xe} = 0 \qquad (4\text{-}68)$$

We therefore discard thepositive root as being unphysical. (It originates due to the fact that we have ignored the vanishing of $I(\Delta k,\infty,\infty)$ for values $b\Delta k \gtrsim 0$).

Thus our final expression reads

$$(b\Delta k)_{mix}^{OPT} = \frac{(b\Delta k)_{Xe} - 4 - [16+(b\Delta k_{Xe})^2]^{\frac{1}{2}}}{2} \qquad (4\text{-}69)$$

$(b\Delta k)_{mix}^{OPT}$ as a function of N_{Xe} is plotted in Figure 4.8.

Thus we see that how much X_e is originally bled into the oven will affect the temperature at which maximum conversion will be observed.

IV-3 Group velocity considerations

For ultrashort light pulses, we require that the condition for optimum conversion to fourth harmonic be satisfied over the entire frequency spectrum which comprises the pulses. We also require that this mismatch condition does not drastically affect the group velocities, i.e. that the fundamental, second harmonic and fourth harmonic pulses maintain at least 50 per cent temporal overlap through the entire length of the cell.

$(b\Delta k)^{OPT}_{Mix}$ Versus N_{Xe}

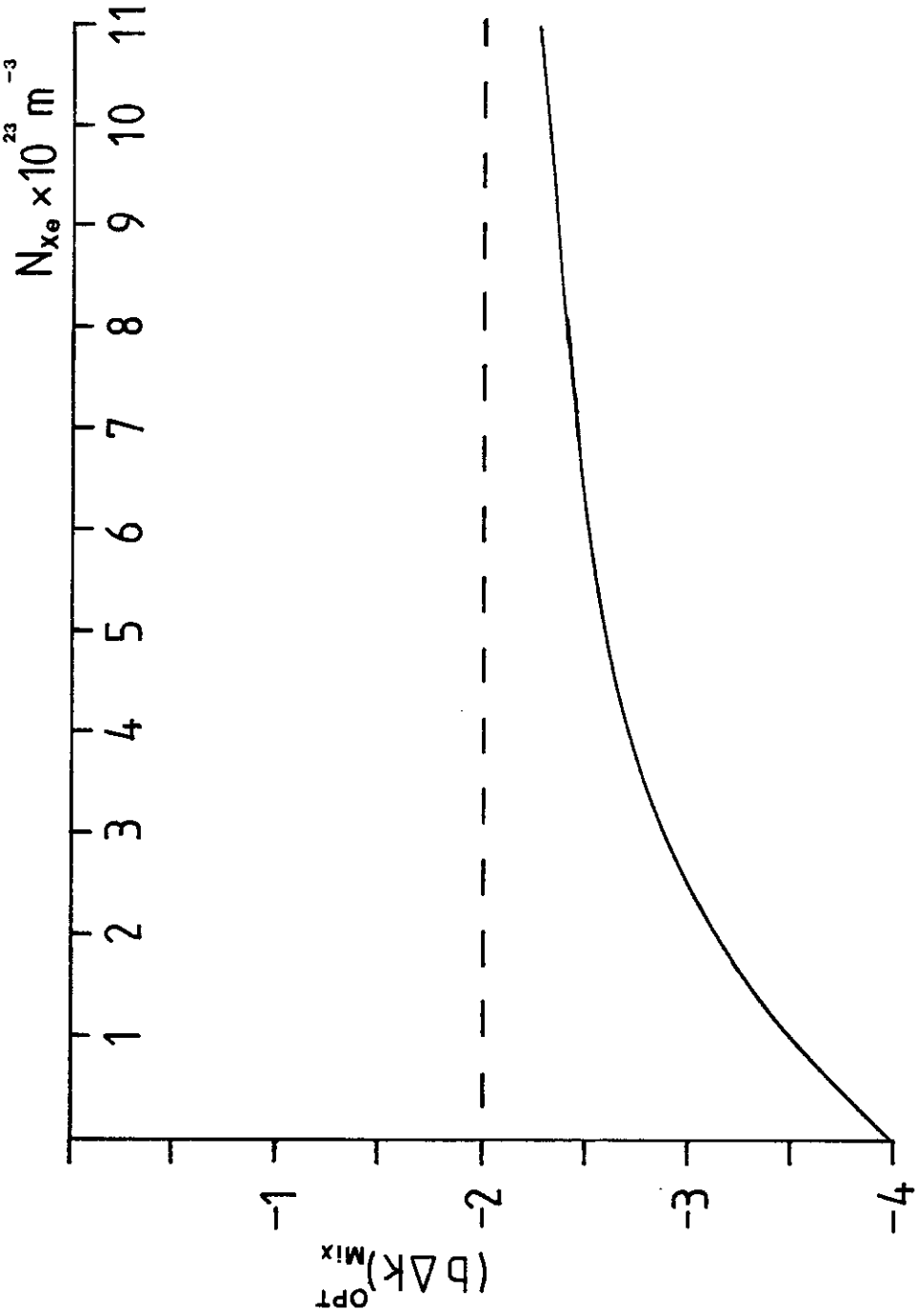

Fig 4-8

A minimum pulse length Δt_{min} which satisfies this condition may be defined by[14]

$$\Delta t_{min} = \frac{n_1 n_2 L}{c^2}\left[\frac{\partial \omega_2}{\partial k_2} - \frac{\partial \omega_1}{\partial k_1}\right] = \frac{n_1 n_2 L}{c^2}\,\Delta v_g$$

where L = cell length

Δv_g = group velocity difference

Obviously similar formulae apply for the various combinations of ω_1, 2ω, and 4ω pulses.

It is found in all cases that Δt_{min} is of the order of 10^{-15} seconds for our experimental conditions, and so group velocity mismatches present no problem.

CHAPTER 5

EXPERIMENTAL DETAILS OF FOURTH HARMONIC GENERATION

I. Introduction

This chapter gives details of the equipment and techniques used in order to produce the fourth harmonic of a mode-locked ruby laser. A description of the laser-amplifier system, and of generation of the second harmonic, have been given in earlier chapters and is not repeated here. The chapter is divided into five parts. Firstly the equipment pertinent to fourth harmonic generation is described. The design and operation of the heat pipe oven are considered in this section, as well as the use of an achromatic doublet and half-wave plate. This is followed by an outline of the experimental procedure adopted, and then the results obtained are presented. A discussion of the results, and their interpretation and explanation is given next, as well as a discussion of general factors limiting the efficiency of conversion to fourth harmonic. Finally, the conclusions to be drawn from the work are presented.

II. Equipment

II-1 The Heat-Pipe Oven

From the discussion in the previous chapter, we see that it is obviously necessary to ensure that phase matching takes place over the whole length of the non-linear medium. This can only occur if the magnesium vapour/xenon gas mixture is homogeneous and if the atomic number density of the magnesium is constant over the entire vapour column. For this to be the case, the column of Mg vapour must be at the same

temperature throughout, and, to this end, a concentric heat-pipe oven arrangement was employed. Before discussing this system, a brief review of heat-pipe operation is given.

A simple heat pipe is shown in Figure 5-1. It is composed of an evacuated chamber whose walls are lined with a mesh to form a capillary structure or "wick". This wick is saturated with a wetting liquid. By heating one end of the pipe, the liquid is made to evaporate and the vapour travels down the tube to a heat sink at the other end, where it condenses again. Capillary action returns the condensate through the wick to the hot end of the pipe. The original purpose of the heat-pipe design was to provide a device having a very large heat conductivity[76].

By introducing a non-condensable inert gas, the performance of the heat pipe may be considerably influenced. The active liquid will then boil at the temperature for which its saturated vapour pressure has a value equal to the partial pressure of the inert gas. On boiling, the vapour drives the inert gas down the tube to the cool region, thereby compressing it, its volume decreasing with rise in vapour temperature and hence pressure. When equilibrium is reached, the hot part of the pipe is filled with the vapour at a pressure determined by the inert gas pressure at the end of the pipe.

II-1.1 Principles of Design and Construction

Figure 5-2(a) shows a schematic of the concentric heat-pipe oven employed, and includes the dimensions. Both inner and outer pipes were made from stainless steel, and were concentric.

The outer pipe acted as a heat-pipe oven in the manner described by Vidal and Cooper[77]. The wick, made from stainless steel mesh, had one end welded to the outer surface of the inner pipe, and was wound in a fan-like structure consisting of several leaves. (In order that capillary action takes place, it is essential that there are at least two layers of mesh in near contact.) The outer pipe was

A Simple Heat Pipe

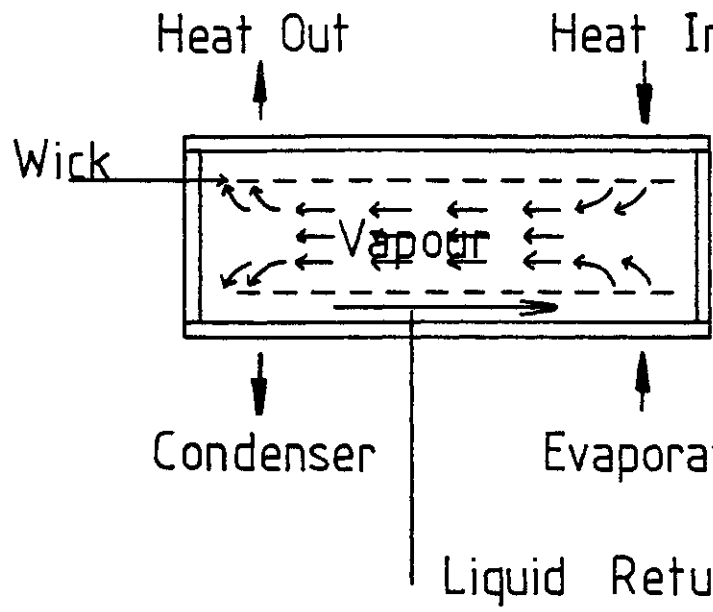

Fig 5-1

The Heat Pipe Oven

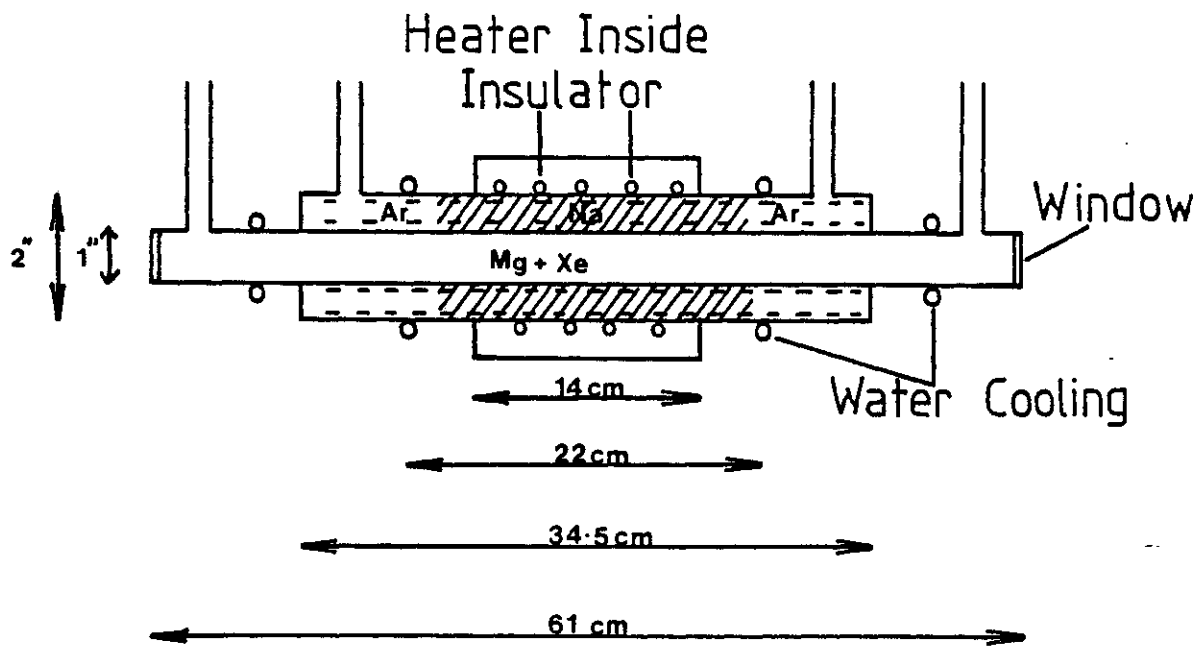

Fig 5-2

filled with sodium (argon gas was blown through the outer pipe whilst it was being loaded so that the sodium did not suffer oxidation). The sodium had been washed in alcohol to remove any traces of liquid paraffin, in which it was stored. Sufficient sodium was placed in the pipe such that when it melted down it would saturate the wick. Heat was applied centrally using a coil heater. Thus in this case the heat pipe action was symmetric, argon gas (which was the inert gas employed) being contained at both ends of the pipe at a pressure which determined the temperature of the pipe (when a steady state was established). It should be noted that the inert gas in any such a system will be completely separated from the sodium vapour except for a short transition region (whose thickness depends upon the pressure) where the temperature drops sharply. The vapour stores energy at the temperature at which it was created, and since evaporation and condensation take place at almost the same temperature, the temperature will be constant to within at most $1^{o}C$ over the whole metal vapour zone[76]. It may therefore be used to heat the inner pipe isothermally, which thus acts as an ideal oven for our purposes.

The magnesium, in chip form, was placed inside the inner pipe. This was partially filled with xenon gas which acted not only as the phase-matching medium but also as a buffer gas to prevent the Mg vapour condensing on the windows. The magnesium vapour passed towards the cooling coils where it condensed, reformed into the solid phase, and remained. Magnesium does not wet stainless steel mesh, and so it was pointless using such a wick to assist the return of the magnesium to the centre of the pipe through capillary action. Besides which, for nearly all the experiments carried out, the magnesium was below its melting point and would not therefore flow back even if a wettable wick were present.

At the typical operating temperatures (600-700°C) the heating coil and the outer surface of the outer pipe were both liable to oxidise rapidly on contact with air. For this reason, after winding the coil onto the outer pipe it was covered completely with a thick layer of white plaster made from an aluminium oxide/sodium silicate paste, which prevented any air reaching the coil or outer pipe. The plaster paste was applied layer by layer, and dried between successive applications using an infra-red lamp. Several sheets of mylar had been placed around the outer pipe and beneath the heating coil before plastering commenced, to prevent an electrical short between the heating coil and the pipe.

The heating wire used was 1.25mm diameter nichrome, and, for the power supply used, a length giving a total resistance of $\sim$ 2.5 ohms was required. The current to the heating coil was controlled using an auto-transformer which ran from a mains transformer delivering a 50V, 20 Amp supply from its secondary coil. The nichrome wire was pre-wound, using a lathe, onto a wooden former to facilitate its winding onto the outer pipe.

After construction the entire "hot" region of the outer pipe was finally enclosed in a ceramic box containing insulating material, to protect the experimenter and reduce heat losses. The protruding ends of the coil were covered with ceramic beads up to their connections with the power supply, in order, as before, to reduce oxidation.

A half-metre long, commercial, Nickle Chromium/Nickle Aluminium calibrated thermocouple was used in conjunction with a digital voltmeter to monitor the temperature. This thermocouple was placed along one side of the inner pipe, and passed through one of the window holders to which it was silver soldered. The difference temperature it measured corresponded to the temperature of the inner pipe compared to room temperature, the latter being continuously monitored. Typical operating temperatures were between approximately 600°C and 700°C. A

quartz (Spec A) input window was used to transmit the incident ruby and second harmonic radiation, and a Barium Fluoride exit window to transmit the generated fourth harmonic (this material also has a high damage threshold). Both windows were $\frac{1}{2}$" in diameter and sealed with "O"-rings onto stainless steel mounts attached to each end of the heat pipe.

II-1.2 Operation

The system was evacuated using a mechanical rotary pump and simple mercury diffusion pump. A schematic of the gas handling system is shown in Figure 5-3. Speedivac vacuum guages were used to determine the pressures within the xenon and argon supply lines and the inner and outer pipes. With the diffusion pump, a pressure of typically $\sim 10^{-4}$ Torr was achieved. This was measured using a Penning gauge connected into the inner pipe's gas handling system. When the pumping was completed, the three valves interconnecting the inner and outer pipes and the pumping line were closed. A certain amount of argon gas was then bled into the outer pipe using a needle valve. The quantity bled in depended upon the ultimate temperature required - see Figure 5-4. Typically pressures between 20 and 120 Torr were used. The heating coil was then turned on, and the system was allowed to reach equilibrium. It was checked whether or not the outer pipe was acting as a heat-pipe by bleeding in more argon gas and observing an immediate rise in temperature in the inner pipe. Such behaviour was taken as indicative of heat-pipe action. Failure to observe this usually indicated that the quantity of sodium present was insufficient to saturate the wick. The desired final temperature was obtained by careful fine adjustment of the argon pressure (either addition or removal) and of the power supply current. The heat pipe oven is shown in Plate 5.

Gas Handling System

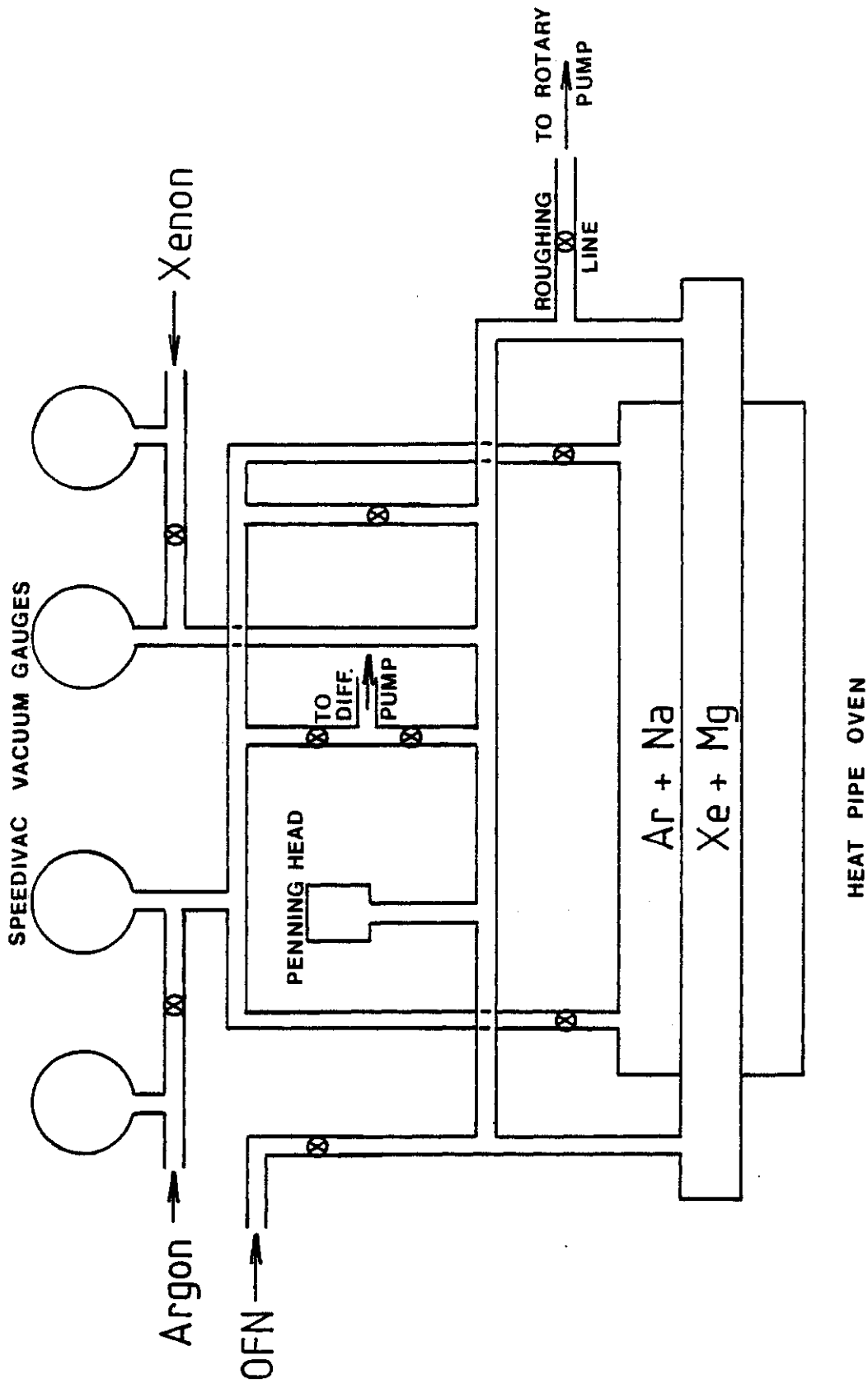

Fig 5-3

Sodium Vapour Pressure Versus Temperature

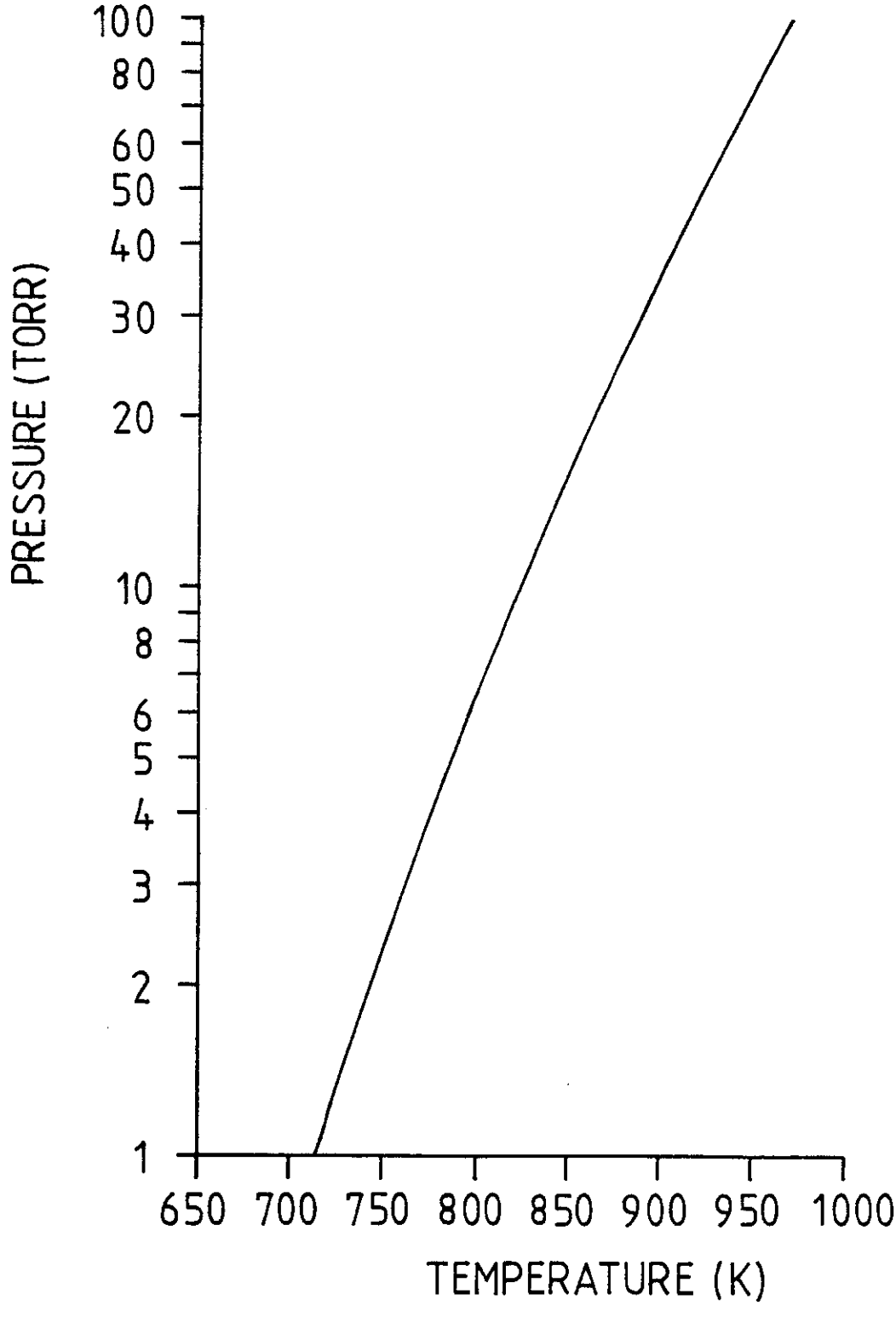

Fig 5-4

PLATE 5

The Heat-Pipe Oven

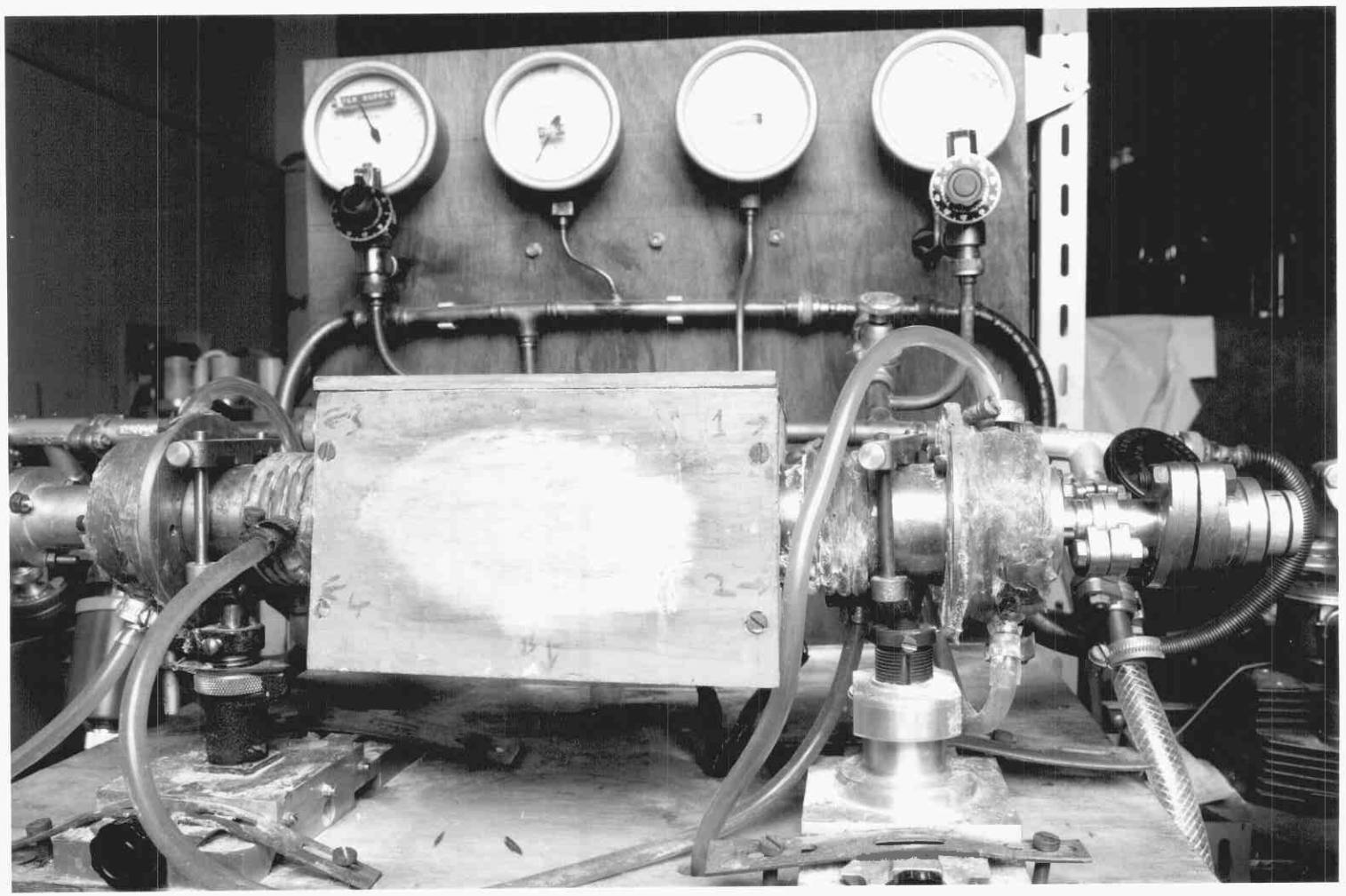

On the whole, the heat pipe functioned reasonably well over a period of several years. The major problem was the heating coil which burnt out several times, and rewinding a replacement and setting it in plaster proved a lengthy task. A more suitable alternative would be a heating arrangement whereby the heat source may be clipped over the outer pipe and may readily be removed. Such designs are now commercially available. It would also be advantageous to have a demountable system such that the flanges at the ends of the outer pipe and the cooling coils are removable.

II-2 The Achromatic Doublet

It has been shown that a small displacement in the focal spot position of the beams at the interacting frequencies can drastically reduce the conversion efficiency to the higher harmonic[59]. For this reason, an achromatic doublet for the ruby and second harmonic wavelengths (6943Å and 3471.5 Å respectively) was used to focus the two beams to the centre of the heat-pipe oven. The doublet consisted of an equi-convex fused silica lens and a lens made of LF5 glass, separated in air. The combination had a focal length of 44.1 cm. The relevant parameters are as below:

Doublet for 6943, 3471 Å

Radius	Clear Rad	Separation	Material
18.4cm	1.25cm		
		0.235cm	Fused silica
-18.4cm	1.25cm		
		0.1 cm	
-17.9197cm	1.25cm		
		0.25cm	LF5
-111.633cm	1.25cm		

II-3 The Half-wave Plate

Due to the technique used for phase matching in the ADP crystal for second harmonic generation, the emergent second harmonic is polarised perpendicularly to the incident ruby laser radiation. For maximum conversion of the fundamental and second harmonic to the fourth harmonic, it is necessary that the two polarisations are parallel. To this end, a half-wave plate for 6943Å was placed immediately after the A.D.P. crystal. This was set up using a Glan-Thomson prism to polarise the He-Ne alignment laser in the same direction as the ruby (i.e. horizontally). The polarised light was passed through crossed polarisers which were adjusted for zero output. The half-wave plate was then placed between the crossed polarisers and rotated for maximum transmission . It was then attached to the mount of the A.D.P. crystal in this orientation.

It should be noted that we assume the half wave plate is full wave plate for the second harmonic, so the polarisation of the latter remains unchanged whilst the fundamental is rotated through $\pi/2$. This requires the birefringence of the material to be the same at the fundamental and second harmonic wavelengths, which is obviously unlikely. However, for the material used (the plate was a mica sheet of 72μm thickness) the birefringence is constant to approximately 10% over this range of wavelength, so we may assume about 90% of the emergent second harmonic beam is linearly polarised in a direction parallel to the fundamental.

III. Experimental Technique

III-1 Magnesium Handling

Before any experimental "run" was carried out (either a scan through temperature for constant Xe pressure, or a scan through Xe pressure at a constant temperature), the inner pipe was "baked" at

typically 300-400°C for several hours whilst being constantly pumped out by the mercury diffusion pump and backing pump. This was primarily to reduce the oxygen level present, as magnesium is a "getter" for oxygen and rapidly forms a covering of Mg O over its surface, which affects its properties and its vapour pressure. After baking, oxygen-free-nitrogen (OFN) was passed into the inner pipe up to a pressure slightly in excess of atmospheric. The end windows of the pipe were then removed, and the constant stream of OFN out of the oven ensured little or no air could pass into the system. Magnesium, in chip form, was loaded into the pipe using a small aluminium scoop to deposit the Mg at one end. The charge was then pushed into the centre of the inner pipe using a dural rod, and a rod of smaller diameter was used to press the charge down so that the He-Ne alignment beam could pass unobstructed along the central axis of the pipe.

The end windows were then replaced and the inner pipe was slowly evacuated (rapid evacuation caused dispersal of the light magnesium chips to both ends of the pipe). When a pressure of $\sim 10^{-4}$ Torr was attained the system was again baked for several hours. After being alllowed to cool again,the inner pipe was filled to a predetermined pressure with xenon gas, and was then raised to the desired temperature to begin the experimental run, in the manner described in the previous section.

The magnesium used was spectroscopically standarised and obtained from Johnson Matthey Chemicals Limited. It was necessary at all stages in the loading procedure to observe strict cleanliness. Plastic gloves were worn at all times when handling the magnesium chips and the dural rods, the latter having been already thoroughly polished and washed with alcohol, followed by Inhibisol. It was found that very small amounts of grease from the hands or oil vapour from pumps could result in the formation of a black coating over the magnesium when its temperature was raised to the required value (600-700°C), preventing

vapourisation of the magnesium. Consequently no fourth harmonic signal would be observed on these occasions. This was made particularly evident after one incident, in which the backing pump failed whilst roughing the system, and oil was sucked back into the inner pipe's gas handling system. Despite repeated thorough cleanings of the inner pipe and associated gas lines, the black deposit re-appeared continuously. Finally, the source of the contamination was traced to the speedivac vacuum guage, whose inside was found to have a very light covering of oil. It was clear that this small quantity of oil was responsible for the problem, since after its removal, the magnesium successfully vapourised and this effect did not occur again, as long as the handling procedures outlined above were followed.

Magnesium, as has already been discussed, does not wet stainless steel, and was usually below its melting point. Because of this, the magnesium vapour condensed on reaching the cool ends of the pipe and there formed "stalactite" and "stalagmite" structures which grew in size as the experiment progressed and eventually partially or completely blocked the path of the input and/or output beams. Normally, by this time, the magnesium in the oven centre would be virtually exhausted, but this effect gave a maximum time limit to any possible experimental run of about five hours, regardless of the quantity of Mg originally present. With a minimum time between shots of 5 minutes (see Chapter 2) this gave an upper limit of about sixty shots for a "scan". The areas of condensation marked the ends of the vapour column, and this was measured to be $\sim$ 9 cm in length.

One possible solution to this problem, it is suggested, is the use of a rotating inner-pipe similar to that described by Hessel and Lucatorto[78]. This is suspended in slip seals and spun at about 600 r.p.m. A 2° double conical taper on the inside wall ensures that a component of the centrifugal force will drive the condensed fluid back

towards the centre of the oven. Even if the temperature is below the melting point, the centrifugal force component will reduce the rate of vapour flow to the cool ends of the oven and thus reduce the rate of deposition of solid magnesium.

At the end of the experiment, the pipe would be allowed to cool, and the inner pipe was cleaned using hydrochloric acid, distilled water, alcohol and acetone in that order. It was then rebaked as before in preparation for another "run".

III-2 Alignment and Detection Procedure

The full experimental arrangement and the two detection systems used are shown in Figures 5-5 and 5-6 respectively. Alignment of the ruby laser and amplifier, and of the second harmonic crystal was as previously described. After removing the achromatic doublet and mount, an exposed sheet of polaroid film was placed in front of the entrance window of the heat-pipe oven, and the laser-amplifier combination was fired. The burn mark obtained on the polaroid was examined for quality. Usually the burn mark was slightly displaced from the red spot formed where the He-Ne laser beam was incident on the polaroid. A parallel plate of glass was introduced in the He-Ne beam (to displace the beam parallel to its original direction) and was adjusted to an angle such that the burn mark of the ruby laser and the red spot from the He-Ne laser were coincident. It was then assumed that the He-Ne beam was following the same path as the ruby laser beam. After removing the polaroid, the heat-pipe was translated horizontally and vertically so that the He-Ne beam passed centrally through the entrance and exit windows and along the axis of the oven. The achromatic doublet was then placed in position so that the He-Ne beam passed through the pole of the lenses. In this position the He-Ne beam was therefore undeviated. By adjusting the position of the doublet the beam was brought to a focus at approximately the centre of the oven.

Experimental Lay-Out

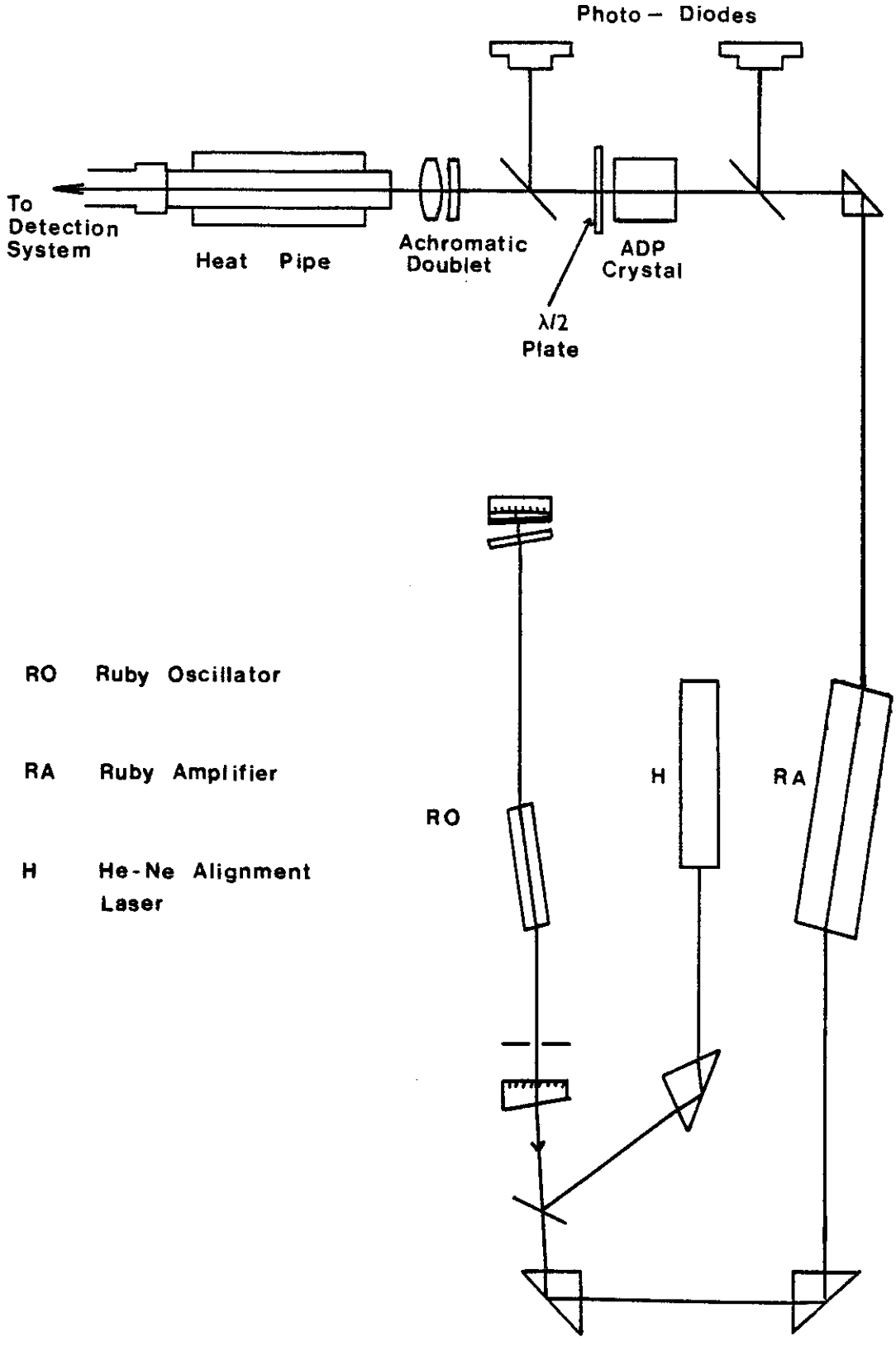

Fig 5-5

Detection Systems Used

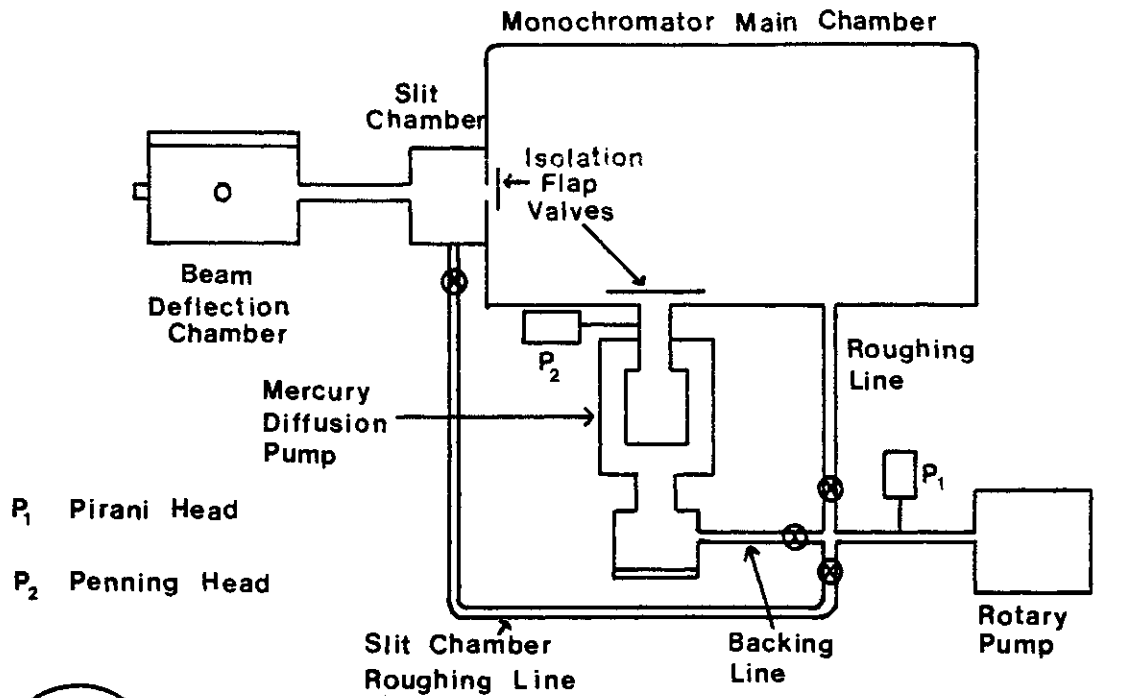

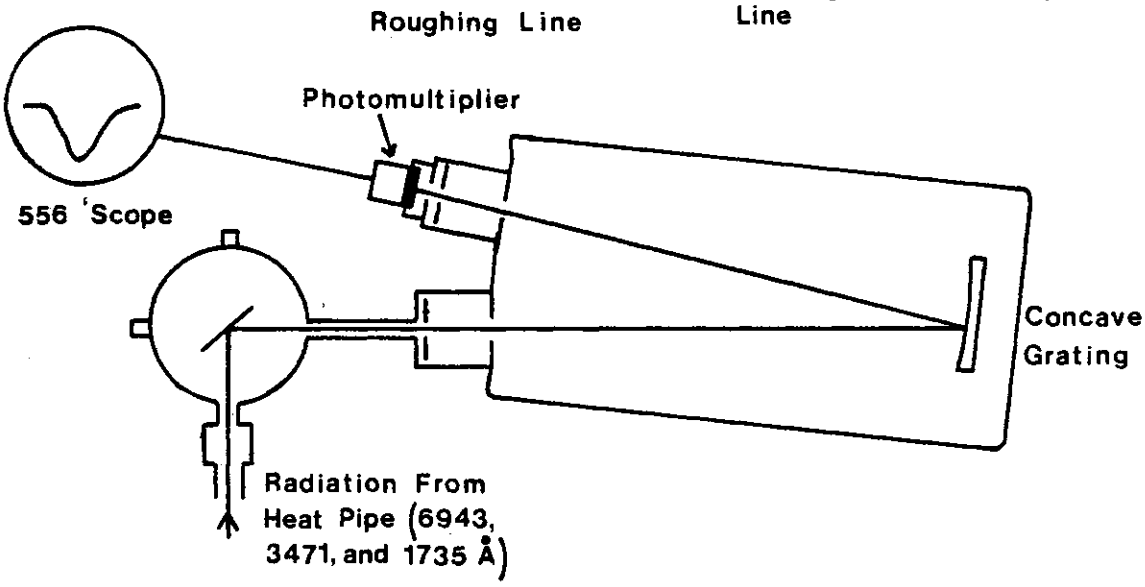

a) Monochromator And Photomultiplier

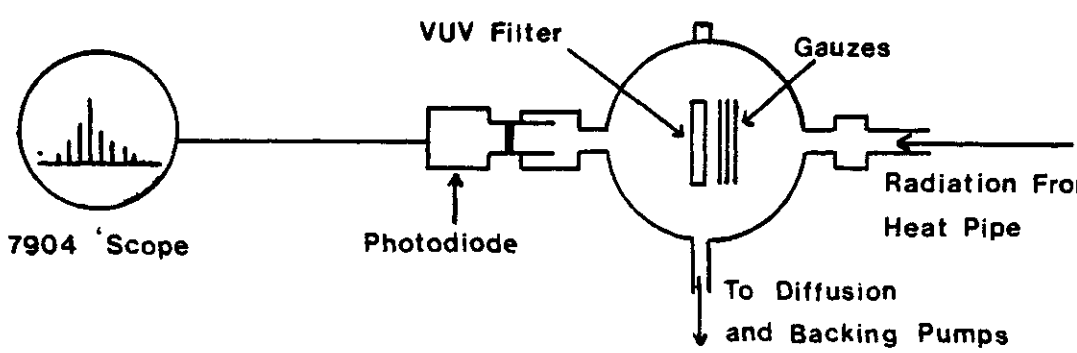

b) V.U.V. Filter And Photodiode

Fig 5-6

The glass plate was then removed, and another shot was fired, this time burning polaroid placed after the exit window of the oven. In this way it was ensured that the ruby beam did indeed pass unobstructed and centrally through the apparatus. Typical burn marks obtained from the ruby oscillator, amplifier (single pass) and after the exit window of the oven are shown in Plate 6.

III-2.1 Use of Monochromator for discrimination purposes

In the preliminary experiments, low magnesium number densities were used (1-2 Torr) and it was not known what size of signal could be reasonably expected. Because of this, a solar blind E.M.R. photomultiplier, model 541G-08-18, was used in conjunction with a McPherson scanning monocromator, model 225, to detect the fourth harmonic radiation produced and to discriminate between it and the second harmonic signal. To direct the beam to the monochromator a dielectric beam splitter with peak reflectivity in the vacuum ultra-violet (v.u.v.) was used, this being placed in the path of the He-Ne beam (leaving the heat-pipe) at an angle of 45°. It was necessary to use this method, since allowing the ruby beam to fall directly onto the input slit of the monochromator would cause damage. The beam splitter was mounted in a circular chamber which could be evacuated, and connections to this chamber from the heat-pipe and monochromator was made via one-inch, easily removable, brass piping. All detection after the heat-pipe had to be done in vacuum, since the fourth harmonic, being in the vacuum ultra-violet, is easily absorbed in air.

The reflected beam from the beam-splitter was made to pass centrally through the monochromator entrance slit and to fall centrally upon the concave diffraction grating. The vacuum piping and seals were then positioned and the deflection chamber and monochromator evacuated.

PLATE 6

Burn Marks on Polaroid

a - After Oscillator and before amplification

b - After amplification

c - After exit window of heat-pipe oven
(Note mode-shape is still well preserved at this stage)

All photographs are twice actual size.

a

b

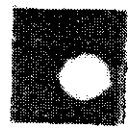

c

The concave diffraction grating, ruled with 1200 lines mm^{-1}, had a radius of one metre and was blazed at 1500 Å in the first order. This was mounted within the scanning monochromator, which had an automatic focussing device to maintain correct focus throughout the wavelength range. The instrument was calibrated for use with a 600 lines mm^{-1} grating and so all scale readings represented double the actual wavelength observed. The setting used for detection of the fourth harmonic at 1735.75 Å was 3482, which included a zero scale reading of 0011.

Evacuation was achieved using mechanical rotary and mercury diffusion pumps, as shown schematically in Figure 5-6(a). The rotary pump was used firstly to evacuate the monochromator and beam deflection chamber through the roughing line. At a pressure of approximately 0.05 Torr, the backing line was switched in. Cooling water was turned on and the cold trap was filled with liquid nitrogen. The diffusion pump was switched on, and when this had warmed up, the main chamber flap valve was opened. The pressure, as read directly above the diffusion pump, fell typically to a value of 2×10^{-5} Torr. During evacuation, the exit slit chamber was sealed using a transparent inspection cover. Both entrance and exit slits were used at the maximum width of 2mm. The alignment was checked by setting the monochromator to zero order and verifying that the He-Ne reference beam emerged from the exit slit. Having established correct alignment the slit chamber flap-valve was closed and the chamber was let up to atmospheric pressure. The inspection cover was removed and replaced with the photo-multiplier, and the chamber was evacuated once more through the slit chamber roughing line.

A Tektronix 556 oscilloscope was used in conjunction with the photomultiplier. This combination had too slow a rise-time to resolve the individual pulses at 1735 Å, and so only the envelope of the mode-locked train was observed. The photomultiplier was operated with an

applied voltage across it of 3 KV, giving a current amplification of 9×10^6. Published data also indicates a discrimination of the order of 10^5 between second and fourth harmonic. The scatter of 3471 Å into the output slit of the monochromator has been quoted as approximately 10^{-5} of the signal passing through in the zero order, and it was therefore expected that only fourth harmonic would contribute to the photomultiplier signal.

As shown in Figure 5-5, glass plates were used to split off part of the incident ruby and second harmonic beams and to deflect them onto biplanar photodiodes (ITT). These were used in conjunction with fast Tektronix 519 oscilloscopes. Filters were used to discriminate against the fundamental beam, when detecting second harmonic, as mentioned previously. The 'scope monitoring the fundamental beam was used to externally trigger the 556 'scope, since it was found that the latter triggered off noise relatively easily. The results obtained are shown and discussed in the first part of the next section.

III-2.2 Use of Filter for Discrimination Purposes

It became apparent that there was sufficient signal at slightly higher magnesium number densities (pressures of 3 Torr and above) to use a photo-diode and transmission filter at 1735 Å to detect the generated fourth harmonic. A fast solar blind photodiode, model F4115, was used, with a Tektronix 7904 oscilloscope. This enabled the individual pulses of the mode-locked train at 1735 Å to be resolved, and so power dependencies and conversion efficiencies could be calculated. The filter used to discriminate between the second and fourth harmonics was an Acton Research Corporation, model 172-N, filter with a peak transmission of 24% at 1735 Å. This was mounted in the circular chamber used previously to hold the dielectric beam splitter. The filter was held in a gimbal mount which was adjusted so that the reflected He-Ne beam from the filter's front face was sent back at a very small angle

(about half a degree) to its incident path, in order to prevent feedback occurring.

The photo-diode was mounted directly behind the filter, as shown in Figure 5-6(b). Several circular, 1" diameter, stainless steel gauzes were placed in front of the front surface of the filter, to prevent the incident ruby beam from burning a hole in the filter. Usually three were used, but five were employed in some of the later experiments. The transmission of each gauze was estimated to be approximately 30%.

One outlet of the chamber was connected to a small oil diffusion pump and rotary pump, which were used to evacuate the chamber. A cold trap was used to isolate the chamber from the diffusion pump. Pressures of typically 10^{-4} Torr were reached, at which point the experiments commenced.

As before, the 519 'scope monitoring the fundamental was used to externally trigger the 7904 'scope, since this was extremely prone to noise pick-up, especially on very sensitive scales (10 mV/cm). To ensure that no second harmonic was detected, a shot was fired with the system up to air, and the trace on the 7904 'scope for a scale sensitivity of 10mV/cm was observed. No signal was ever observed, and so it was concluded that the discrimination factor was satisfactory. When a fourth harmonic signal was observed, the chamber would be filled with air, and another shot fired, so ensuring that the observed signal was in the v.u.v. This was always found to be the case.

The results recorded in this way formed the main body of the data collected, and are discussed in the following section.

III-3 A Note on Phase-Matching Technique

The problem of inadequate mixing of the phase-matching gas with the non-linear medium has been mentioned by several authors [79,6]. To ensure that proper mixing did indeed take place when scans of Xe pressure were undertaken, the following technique was used. For the operating temperature required, the expected phase-matching ratio was calculated using the method described in the previous chapter. Approximately double the expected pressure of xenon for optimum signal was bled in at room temperature, and the heat-pipe was then turned on. This consequently meant that the partial pressure of xenon in the hot region of the pipe was well above the optimum when the desired temperature was reached, but because it had warmed up with the magnesium vapour, it was felt that proper mixing was ensured. The scan consisted, then, of slowly bleeding out xenon and recording the fourth harmonic signals at various decreasing values of xenon pressure. In this way, the point of optimum ratio of Xe:Mg was always passed, and mixing was always guaranteed in a way that need not necessarily occur if cold xenon gas were bled into the system when the desired temperature had been reached. In the latter case, it may have been necessary to wait for an indeterminate period before proper mixing had taken place.

IV. Results

The results taken fall naturally into two parts, those taken at low magnesium number densities (Mg partial pressures of below 3 Torr) and those which were taken for higher number densities (Mg partial pressures above 3 Torr). As will be discussed, saturation effects occurred at the higher number densities. These higher pressures were first used in an effort to increase the conversion efficiency, since according to the simple theory of the previous chapter the relative

fourth harmonic power should scale with the square of the number density (see Equation 4-26). This theory omits consideration of any competing processes or saturation effects.

IV-1 Low Number Densities ($N_{Mg} < 3.5 \times 10^{22}$ atoms/m^3)

The preliminary experiments were all carried out at low number densities, and, as indicated, the monochromator/photomultiplier combination was first used for detection purposes.

Plate 7 shows a series of three typical ruby mode-locked trains and their corresponding fourth harmonic signals (note the individual fourth harmonic pulses are not resolved because of the slow rise time of the detection system). These three results are not at the optimum conditions, but are chosen because they show well the extreme non-linearity we should expect from the harmonic process, especially shot (b), where the slightly lower second maximum in the fundamental train is shown up as a much smaller second peak in the fourth harmonic signal. Also shown in (d) is the effect of "detuning" the monochromator 20 Å away from its normal setting, which resulted in no recorded signal and demonstrated conclusively that fourth harmonic was being observed.

Whilst the monochromator was in use, a spectrum of the radiation at 1735 Å was also taken. An entrance slit width of 25μm was used, and the line was photographically recorded as Kodak SC7 film. The mercury line at 1849.68 Å was used for calibration purposes. A typical result is shown in Plate 8. The dispersion of the monochromator was measured to be 8.46 Å/mm[80]. The linewidth (full width half maximum) was estimated to be 0.35 Å. There is reasonable evidence[44,25] to suggest that the bandwidth of the ruby pulses increases from ∿ 0.5Å at the beginning of the train to ∿ 1.2 Å at the end. The measured bandwidth of the fourth harmonic should be one-eighth of the maximum of the fundamental, if no complicating factors are considered. The bandwidth obtained was approximately double the expected value, so some self-phase modulation in the Mg vapour may have occurred.

To gain more quantitative information, it was necessary to

PLATE 7

Fundamental Trains and the corresponding Fourth Harmonic Harmonic signal recorded using Monochromator and Photo-Multiplier

a)
b) $N_{Mg} = 2.9 \times 10^{22}\ m^{-3}$
c) $N_{Xe} = 1.92 \times 10^{23} m^{-3}$

d - Monochromator detuned by 20 Å - all other conditions identical.

L.H.S.		R.H.S.	
Fundamental		Fourth Harmonic	
Vertical Scale:	10V/cm	Vertical Scale:	0.1V/cm
Timebase :	50 nsec/cm	Timebase :	100nsec/cm

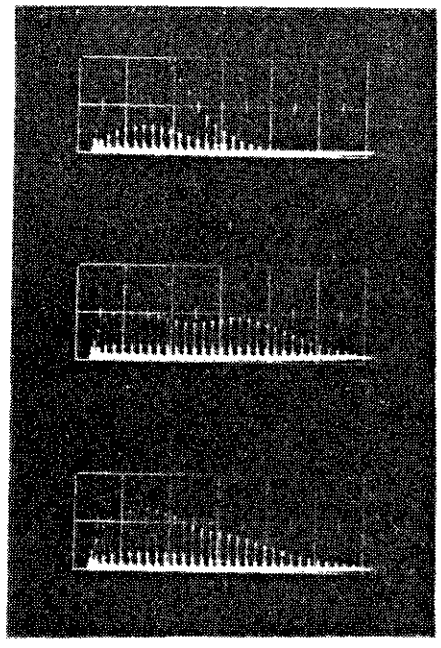

a

b

c

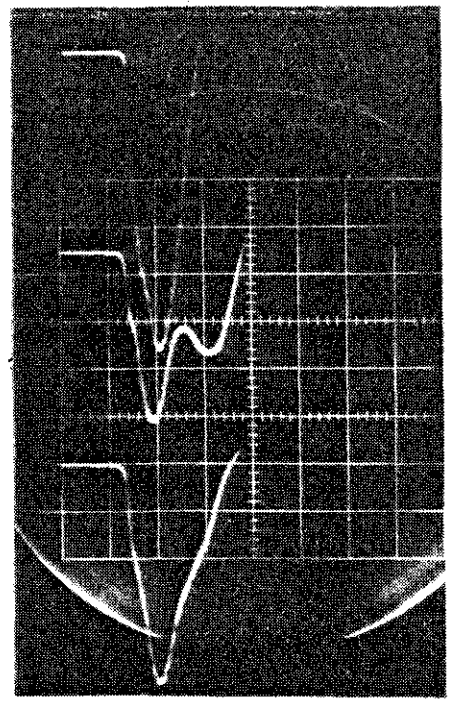

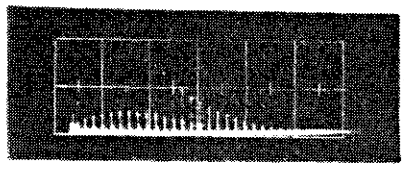

d

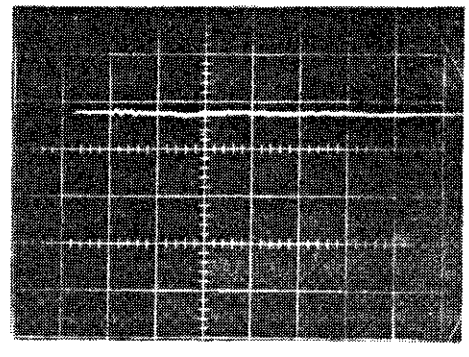

PLATE 8

Spectrum of Fourth Harmonic (inset) and corresponding microdensitometer trace using 10:1 ratio arm.

L.H.S.

Mercury Calibration Line at 1849.68 Å

R.H.S.

Fourth Harmonic Line at 1735.75 Å

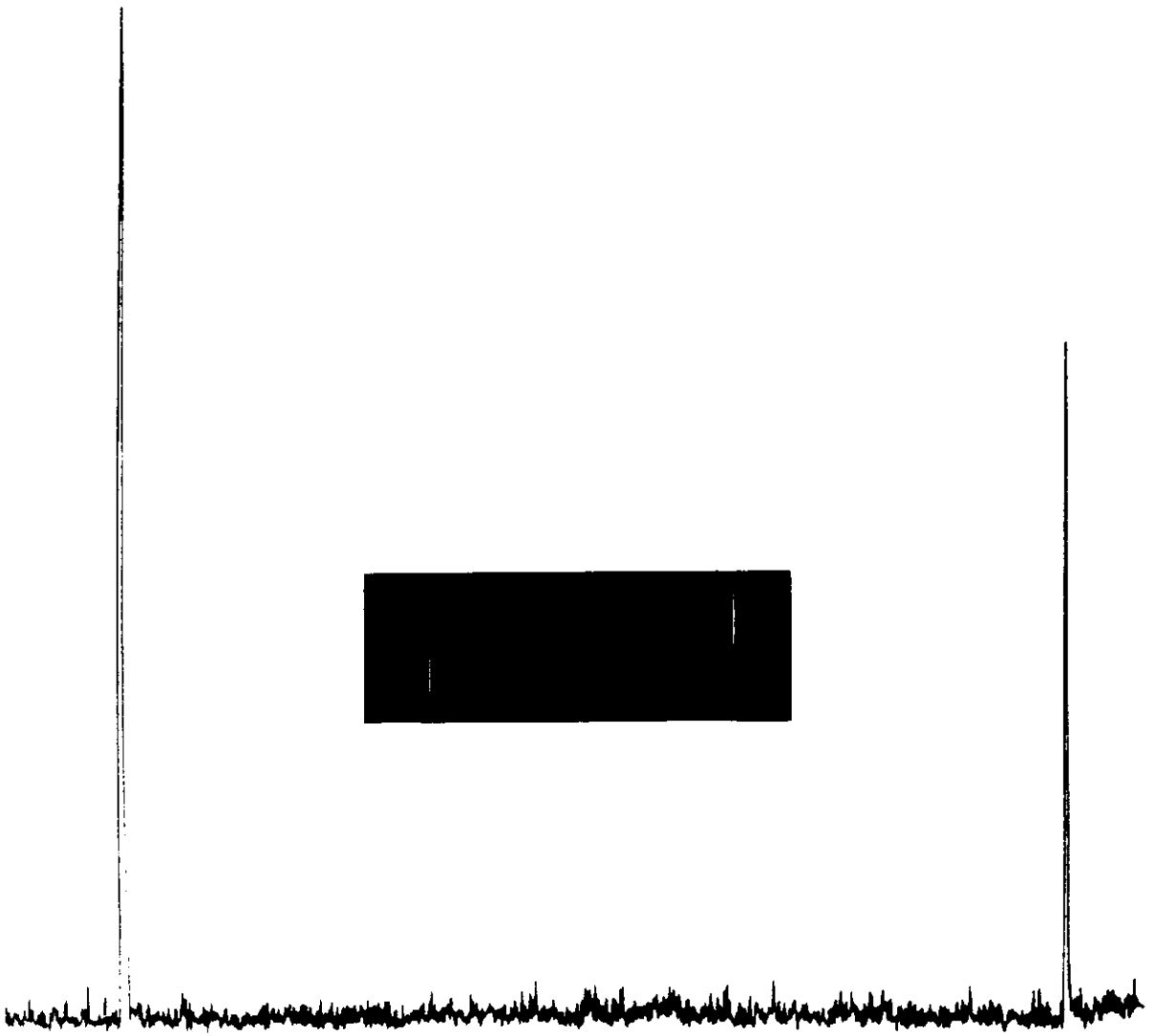

use the photodiode/filter combination for detection. Scans of relative fourth harmonic versus xenon pressure were taken. The appearance of the pulse trains at the fundamental and fourth harmonic wavelengths is shown in Plate 9, and the extreme non-linearity of the process again is evident. It should be noted that the pulses as photographed represent the total energy in each light pulse, as their width is limited by the rise-time of the photo-diode oscilloscope pair. This width was estimated to be approximately four nanoseconds. The area of the photographed pulse is proportional to the total number of fourth harmonic photons detected, and so the height is proportional to the energy of the light pulse. It may be taken as proportional to the power of the pulse if we assume the pulse duration is a constant.

A graph of fourth harmonic power as a function of fundamental power on a log-log scale is given in Figure 5.7. These results were typical for a Mg number density of $3.2 \times 10^{22}\ \bar{m}^3$. Each point is the average of several shots, the points being taken from measurements of the heights of the third, fourth and fifth pulses in the ruby train, the fifth being the largest. (It was assumed that the largest pulse in the fourth harmonic train corresponded to the largest pulse in the fundamental train, in the results analysis.) It is of interest to note that the value of the gradient implies a power dependence for the fourth harmonic of the form

$$P_4 \quad \alpha \quad P_1^{3.55} \qquad (5\text{-}1)$$

This is readily understood when the second harmonic power dependance is investigated. From Figure 5-8, which is also plotted on a log-log scale, we find

$$P_2 \quad \alpha \quad P_1^{1.55} \qquad (5\text{-}2)$$

PLATE 9

Fundamental and corresponding Fourth Harmonic trains

(detected with Solar Blind Photodiode + 7904 'Scope)

a - $N_{Mg} = 3.15 \times 10^{22}\ m^{-3}$

Xe Partial Pressure = 9.1 Torr

b - $N_{Mg} = 3.15 \times 10^{22}\ m^{-3}$

Xe Partial Pressure = 5.9 Torr

L.H.S.	R.H.S.
Fundamental	Fourth Harmonic
Vertical Scale: 10V/cm	Vertical Scale: 20mV/cm
Timebase : 50nsec/cm	Timebase : 20nsec/cm

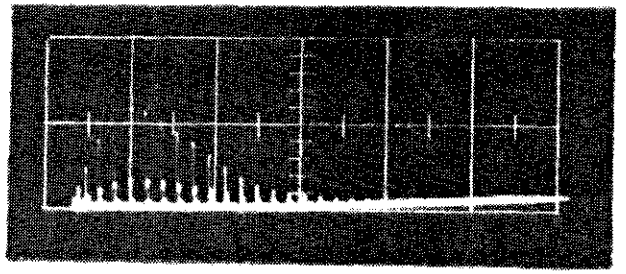

a

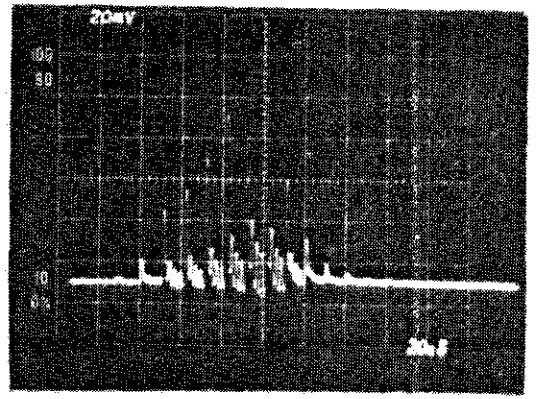

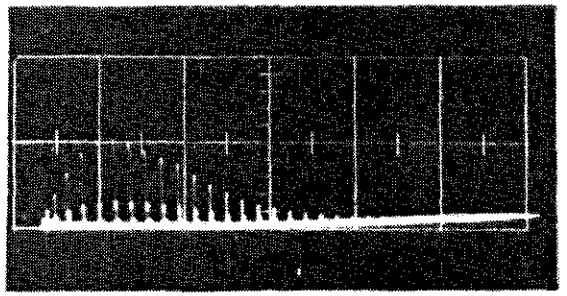

b

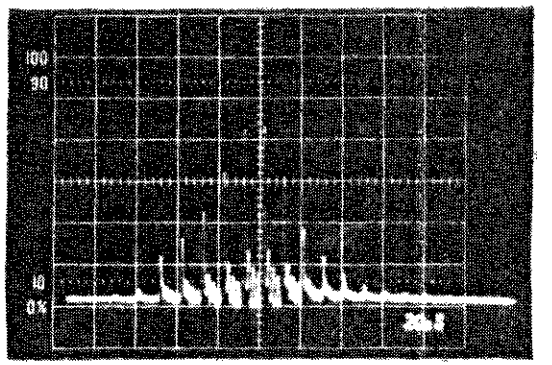

Power Dependance Of Fourth Harmonic On Fundamental (For 3rd, 4th, And 5th Pulses In Train)

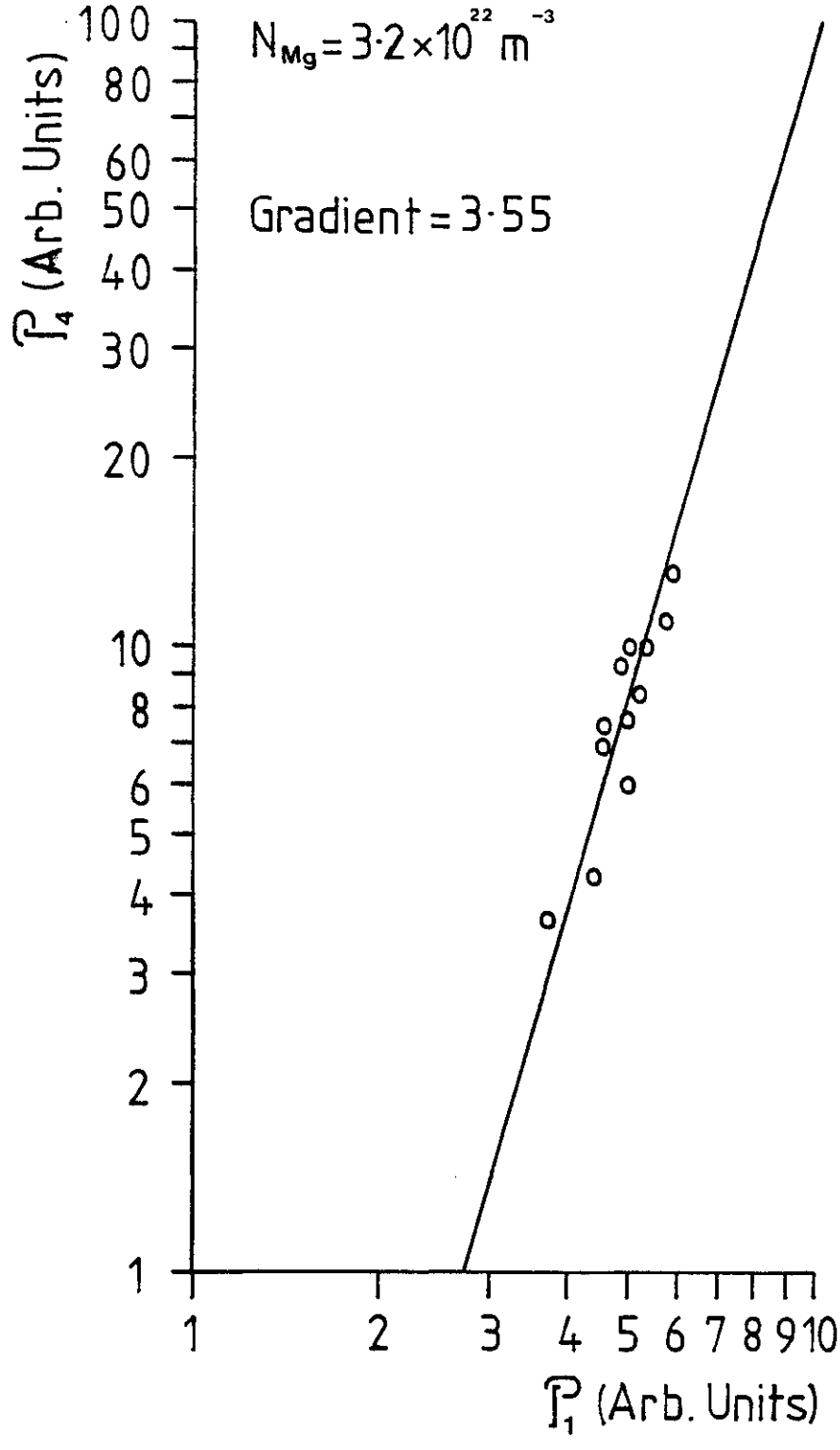

Fig 5-7

Power Dependance Of Second Harmonic On Fundamental

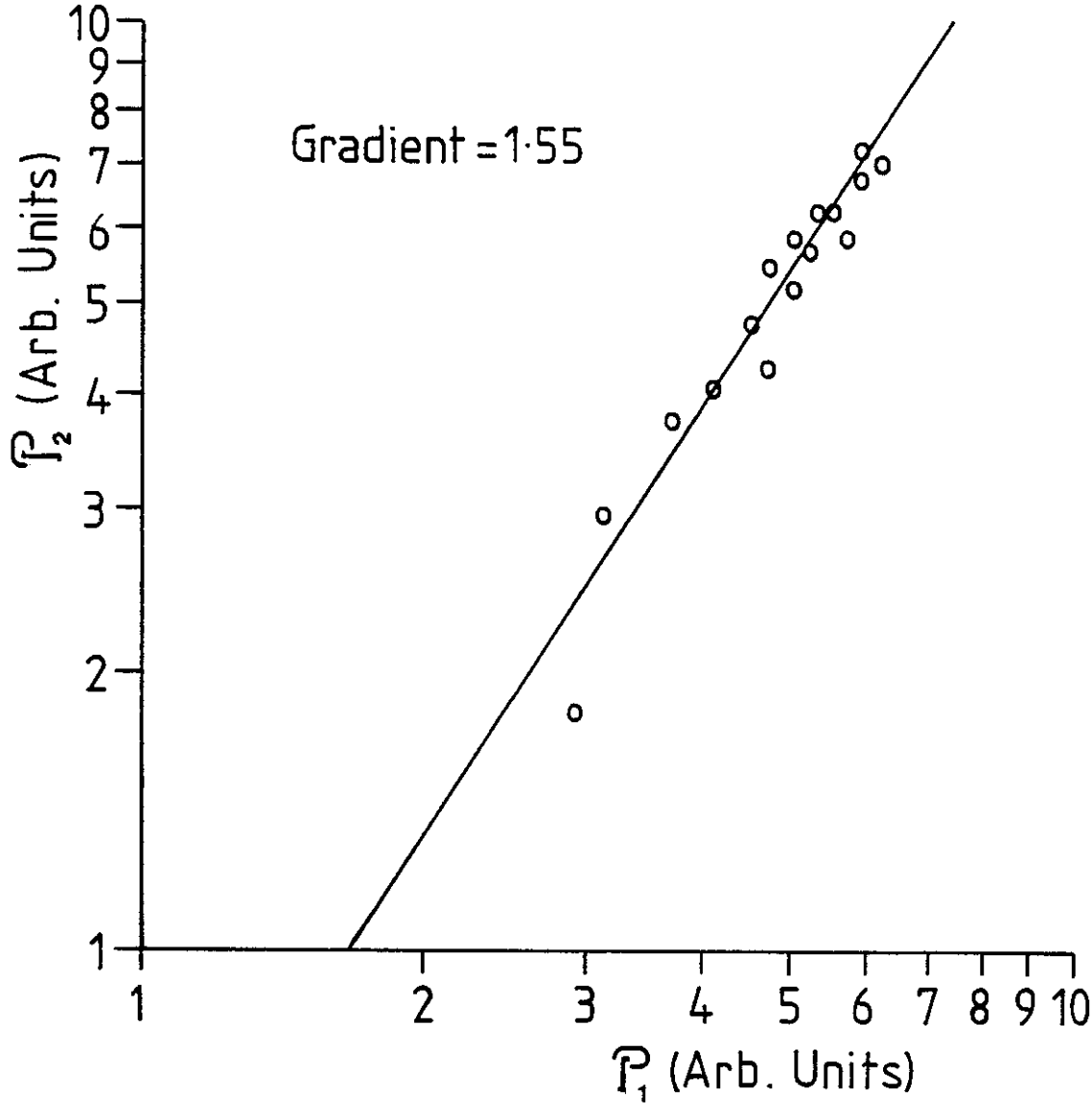

Fig 5-8

for the results taken at the time of this particular experiment. The simple theory of the previous chapter predicts a power dependance of

$$P_4 \quad \alpha \quad P_1^{\,2} P_2 \qquad (5\text{-}3)$$

and so, using (5-2) in (5-3) we recover (5-1), which is thus in exact agreement with the theory.

A typical scan of relative fourth harmonic signal versus xenon pressure is shown in Figure 5-9. Again the points plotted are an average of several shots. The graph is normalised to a maximum value of one. If instead the graph is normalised to a maximum value of 5.78, and the relative signal plotted against the $b\Delta k$ value for the mixture, as in Figure 5-10, very close agreement is obtained with the theoretically predicted curve. This theoretical curve was calculated using a computer program for a value of $b/L = 0.25$. This program is discussed in the Appendix. A maximum is obtained for a xenon partial pressure of $19(\pm 1)$Torr, indicating a number density ratio for optimum signal of $6.3\ (\pm\ 0.3):1$, and a $b\Delta k$ value for optimum of $-2.1\ (\pm\ 0.2)$. This is in close agreement with the theory as indicated in Figures A-1 and 4.6(b), especially when it is considered that the vapour pressures used in the calculations are not accurately known, and that the calibration of the thermocouple is also subject to some error ($\pm$ 5°C).

The maximum fourth harmonic power obtained at these low number densities was 40.3×10^3 watts,* assuming the pulse at 4ω to be ten picoseconds in duration. This represents, with a fundamental power of 165.7×10^6 watts,* a conversion efficiency of 2.4×10^{-4} and implies

---

* These values are calculated taking into account reflection losses.

Relative Fourth Harmonic Power

Versus Xenon Partial Pressure

$N_{Mg} = 3{\cdot}15 \times 10^{22}\ m^{-3}$

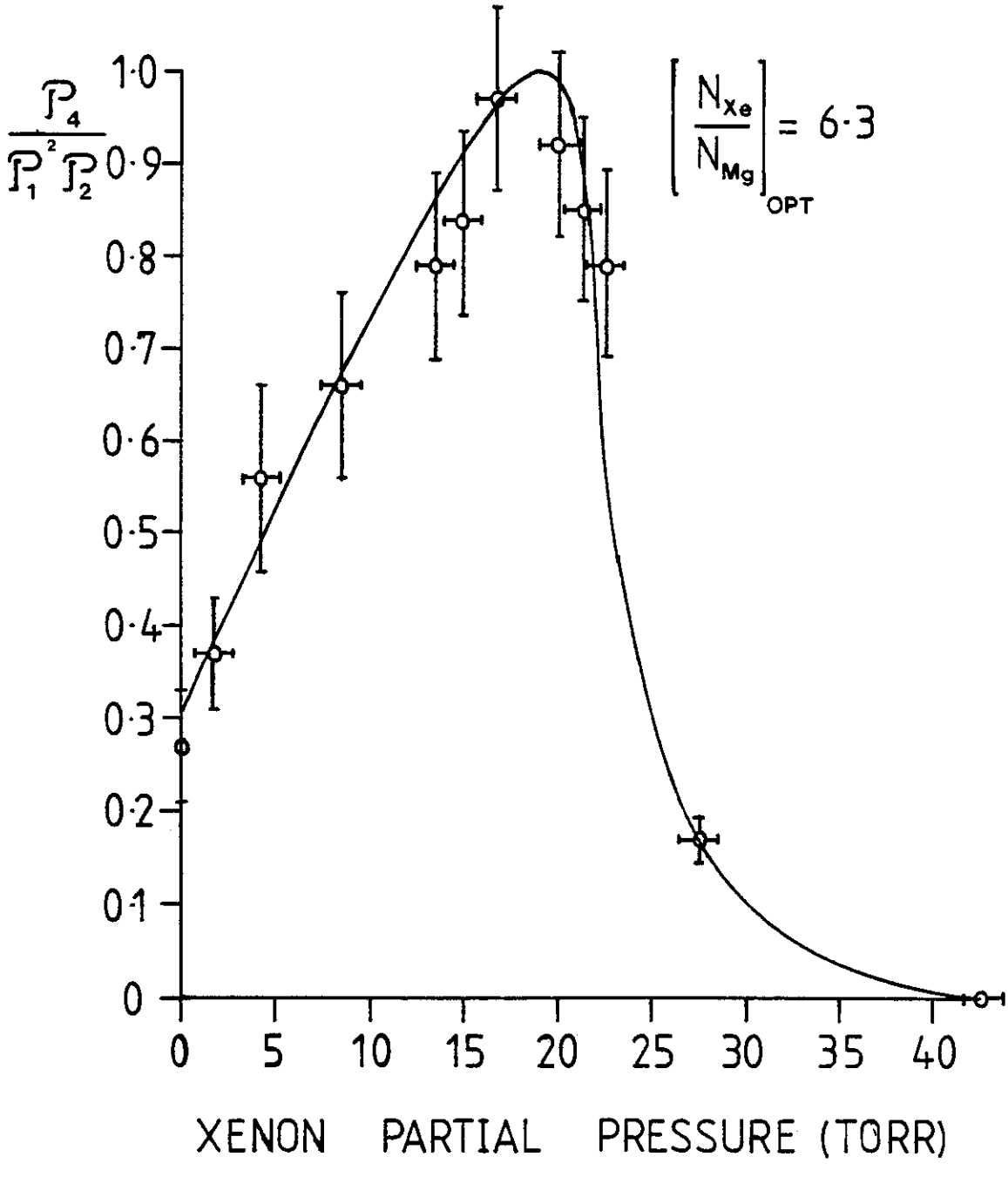

Fig 5-9

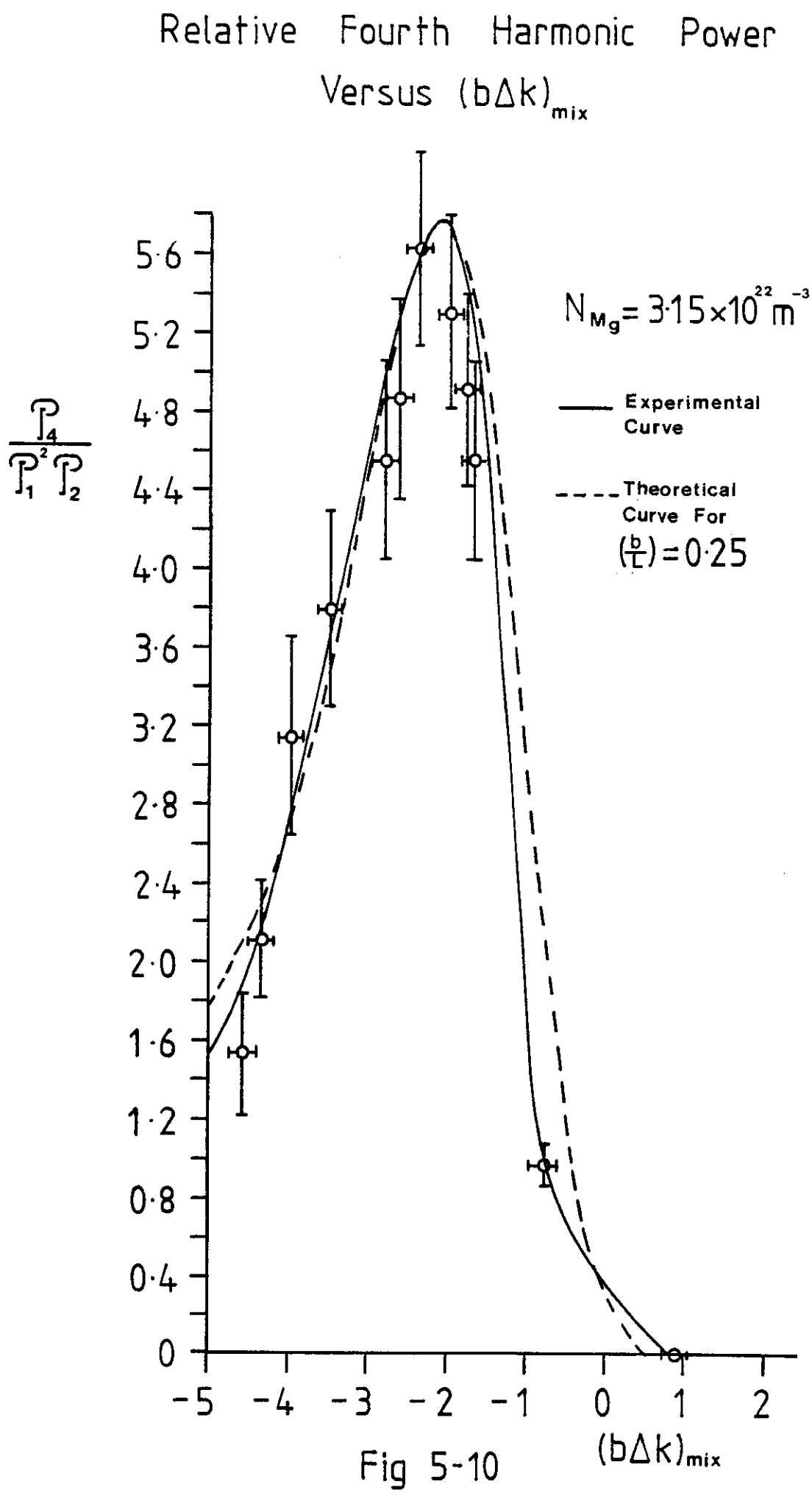
Relative Fourth Harmonic Power
Versus $(b\Delta k)_{mix}$
$\frac{\Gamma_4}{\Gamma_1^2\Gamma_2}$
$N_{Mg} = 3{\cdot}15 \times 10^{22}\ m^{-3}$
Experimental Curve
Theoretical Curve For $(\frac{b}{L}) = 0{\cdot}25$
5·6
5·2
4·8
4·4
4·0
3·6
3·2
2·8
2·4
2·0
1·6
1·2
0·8
0·4
0
-5
-4
-3
-2
-1
0
1
2
$(b\Delta k)_{mix}$

Fig 5-10

a non-linear susceptibility of approximately 5×10^{-49} m^5V^{-2} (Equation 4-26). The discrepancy between this value and the theoretical one is discussed in the next section.

One last point of interest is the rapid fall-off of fourth harmonic with fundamental intensity once the peak of the ruby mode-locked train has been passed (i.e. after the fifth pulse). This was an effect which was observed at all number densities and for all shots. It can be seen in the photographs of Plate 9, and the log-log plot of power dependency is given in Figure 5-111, for number densities of 3.2×10^{22} m^{-3}. These points were taken from measured heights of the sixth, seventh, eighth and ninth pulses of the ruby train. Evidently, from the gradient, a power dependence is implied for the fourth harmonic of the form

$$P_4 \alpha P_1^{5.55} \qquad (5\text{-}4)$$

This effect can be explained quite simply in terms of the pulse broadening which occurs in the second half of the fundamental train due to self-phase modulation in the ruby rod. This is discussed in Chapter 2. Since the pulse heights measured are really proportional not to the power, but to the energy of the light pulses, the power of the pulses in the second half of the train is overestimated. (It is implicitly assumed that the pulse duration remains constant throughout the train when using this measurement technique). As the pulse duration increases, so the realpower decreases more quickly than the photographs would imply, and consequently the fourth harmonic power drops more quickly than would be expected. It also follows that the fourth harmonic pulses in the second half of the train should be longer, and so the power of these is also overestimated from the photographs. This effect (self-phase modulation) increases the bandwidth of the pulses, so

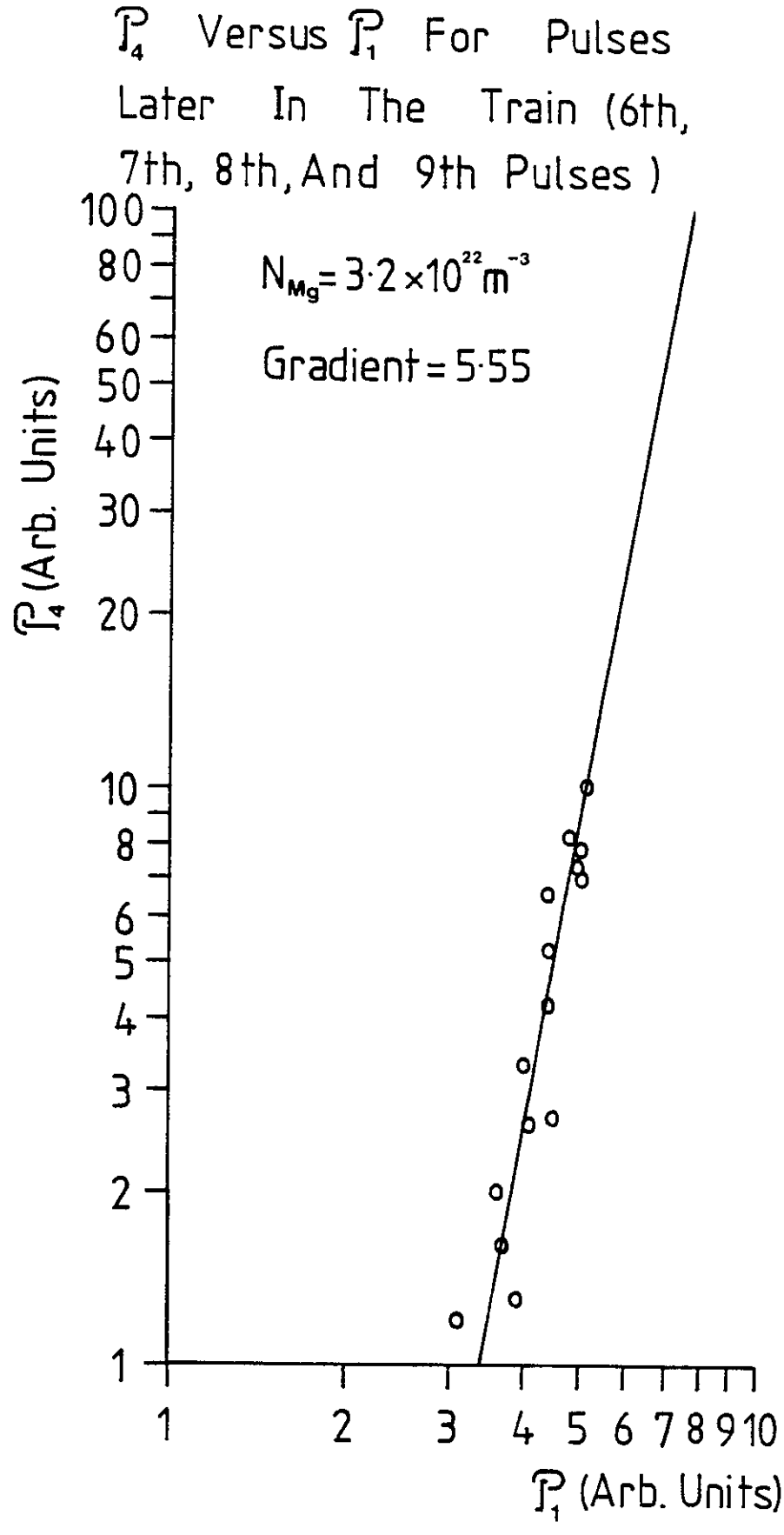
P_4 Versus P_1 For Pulses Later In The Train (6th, 7th, 8th, And 9th Pulses)
$N_{Mg} = 3{\cdot}2 \times 10^{22} m^{-3}$
Gradient = 5·55
P_4 (Arb. Units)
100
80
60
50
40
30
20
10
8
6
5
4
3
2
1
1
2
3
4
5
6
7
8
9
10
P_1 (Arb. Units)

Fig 5-11

the spectral brightness decreases, and this will also lower the power of fourth harmonic generated.

IV-2 Higher Number Densities. ($N_{Mg} > 3.5 \times 10^{22}$ m^{-3})

In an attempt to obtain higher conversion efficiencies, higher magnesium number densities were used. This led to the unexpected observation of saturation effects, which became more pronounced with increasing number density. Fourth harmonic trains observed for number densities of 3.85×10^{22} m^{-3}, 7.35×10^{22} m^{-3}, and 9.8×10^{22} m^{-3} are shown in Plate 10. The power dependencies for number densities of 3.85×10^{22} m^{-3}, 5.2×10^{22} m^{-3} and 7.35×10^{22} m^{-3} are plotted in Figures 5-12 to 5-14. The corresponding pressure scans are plotted in Figures 5-15 to 5-17. All these graphs are normalised to a maximum value of unity (this value does not indicate their relative magnitudes). As before, the points are all averages of several shots, and were taken from the third, fourth and fifth pulses in the train, the fifth being the largest.

The relative power of the fourth harmonic, which is the ordinate in Figures 5-15 to 5-17, was calculated using the respective power dependancies deduced from the log-log plots of Figures 5-12 to 5-14. It is noted that at the highest number densities, the fourth harmonic has become insensitive to change in the fundamental or second harmonic intensity.

The relative fourth harmonic signal as a function of magnesium number density is shown in Figure 5-18. The expected scaling with the square of the number density is followed.

At the highest number densities (7.35×10^{22} m^{-3}) the maximum power obtained was 297×10^{3} watts (again assuming a ten picosecond pulse at 4ω and taking into account reflection losses at the exit window).

PLATE 10

Fundamental and corresponding Fourth Harmonic trains at various Magnesium atomic number densities

a - $N_{Mg} = 3.8 \times 10^{22}\ m^{-3}$
Xe Partial Pressure = 44 Torr

b - $N_{Mg} = 7.35 \times 10^{22}\ m^{-3}$
Xe Partial Pressure = 112 Torr

c - $N_{Mg} = 9.8 \times 10^{22}\ m^{-3}$
Xe Partial Pressure = 140 Torr

L.H.S.

Fundamental

a.	Vertical Scale: 10V/cm	Vertical Scale: 10mV/cm
	Timebase : 50nsec/cm	Timebase : 20nsec/cm
b.	Vertical Scale: 10V/cm	Vertical Scale: 50mV/cm
	Timebase : 50nsec/cm	Timebase : 20nsec/cm
c.	Vertical Scale: 10V/cm	Vertical Scale: 100mV/cm
	Timebase : 50nsec/cm	Timebase: 20nsec/cm

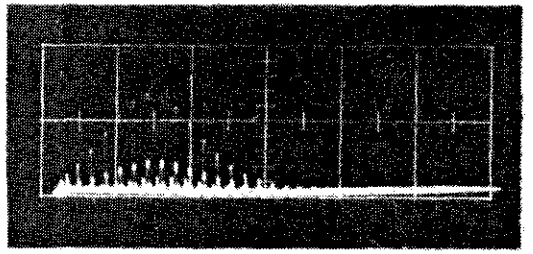

a

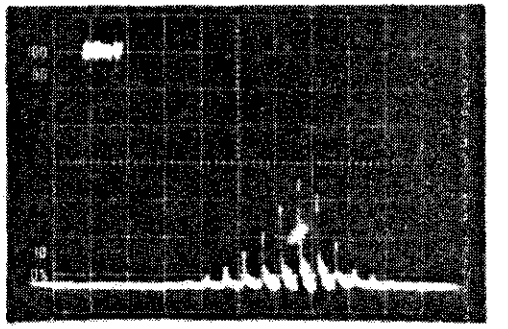

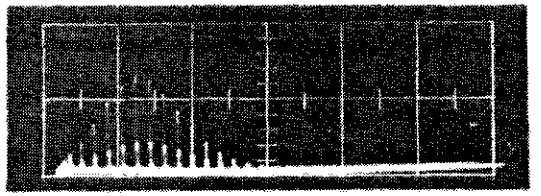

b

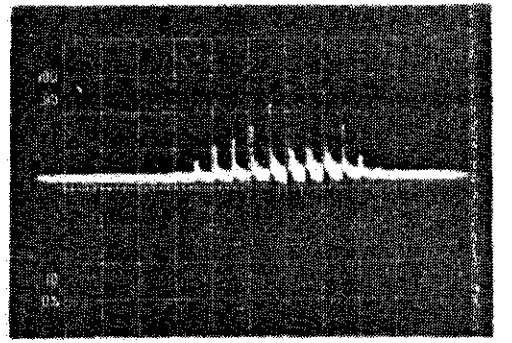

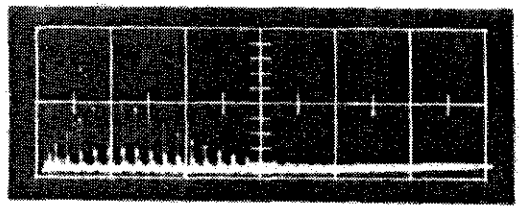

c

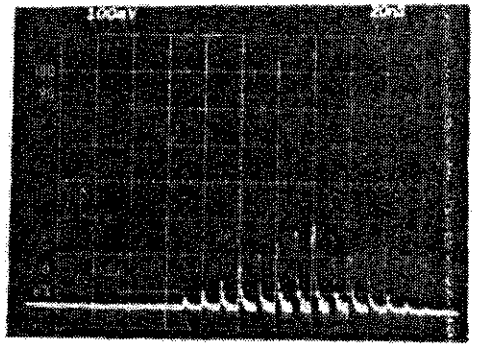

P_4 Versus P_1

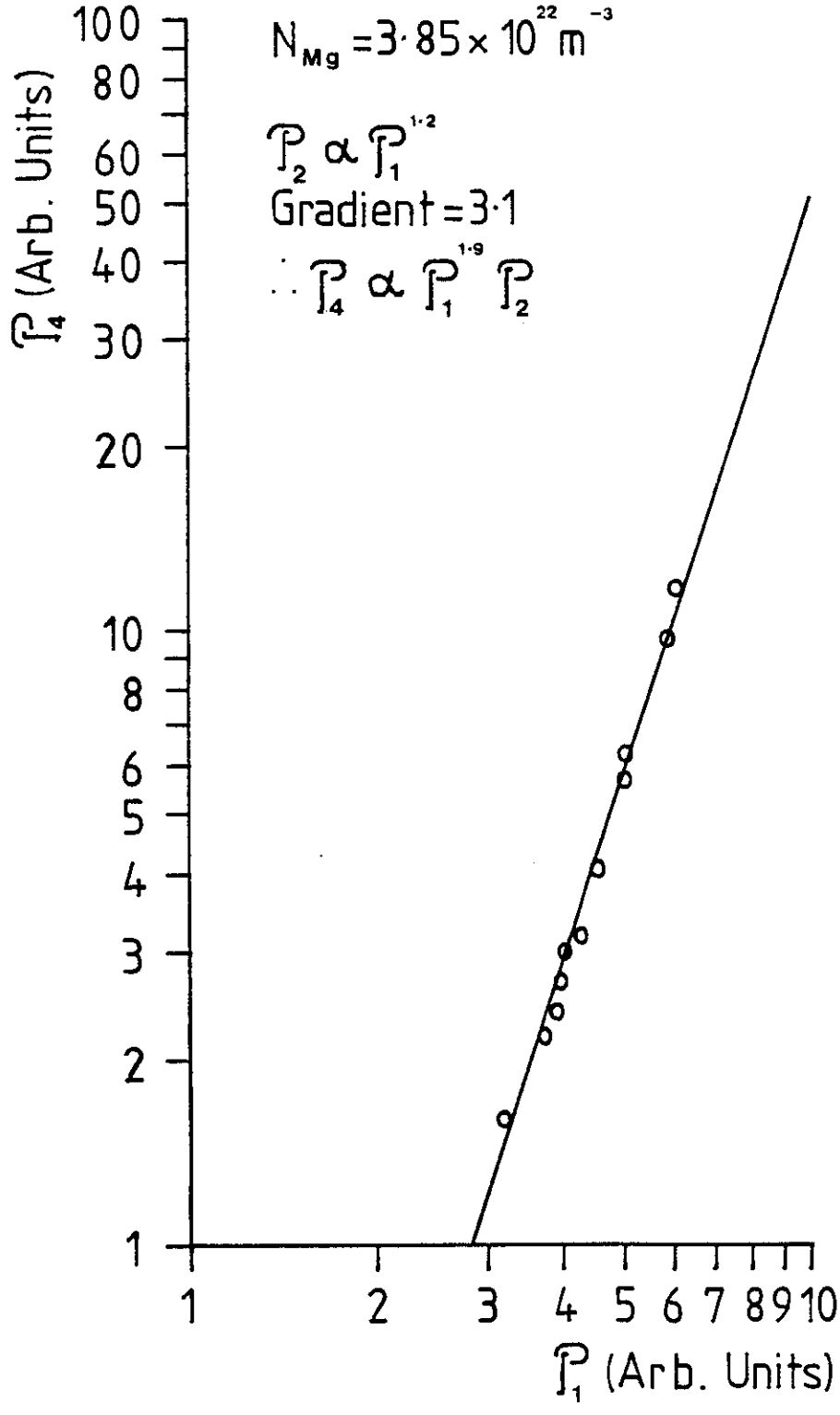

Fig 5-12

P_4 Versus P_1

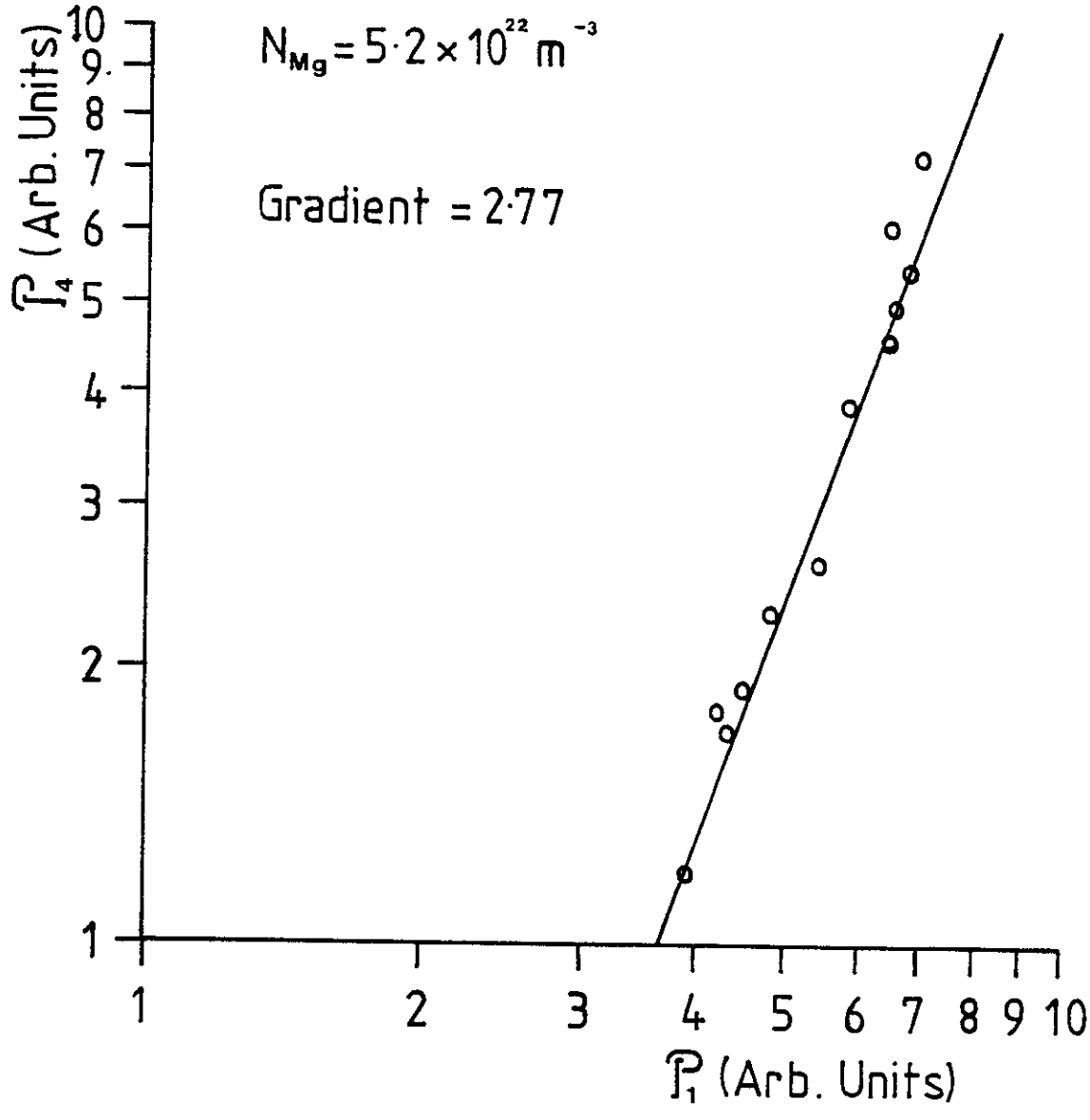

Fig 5-13

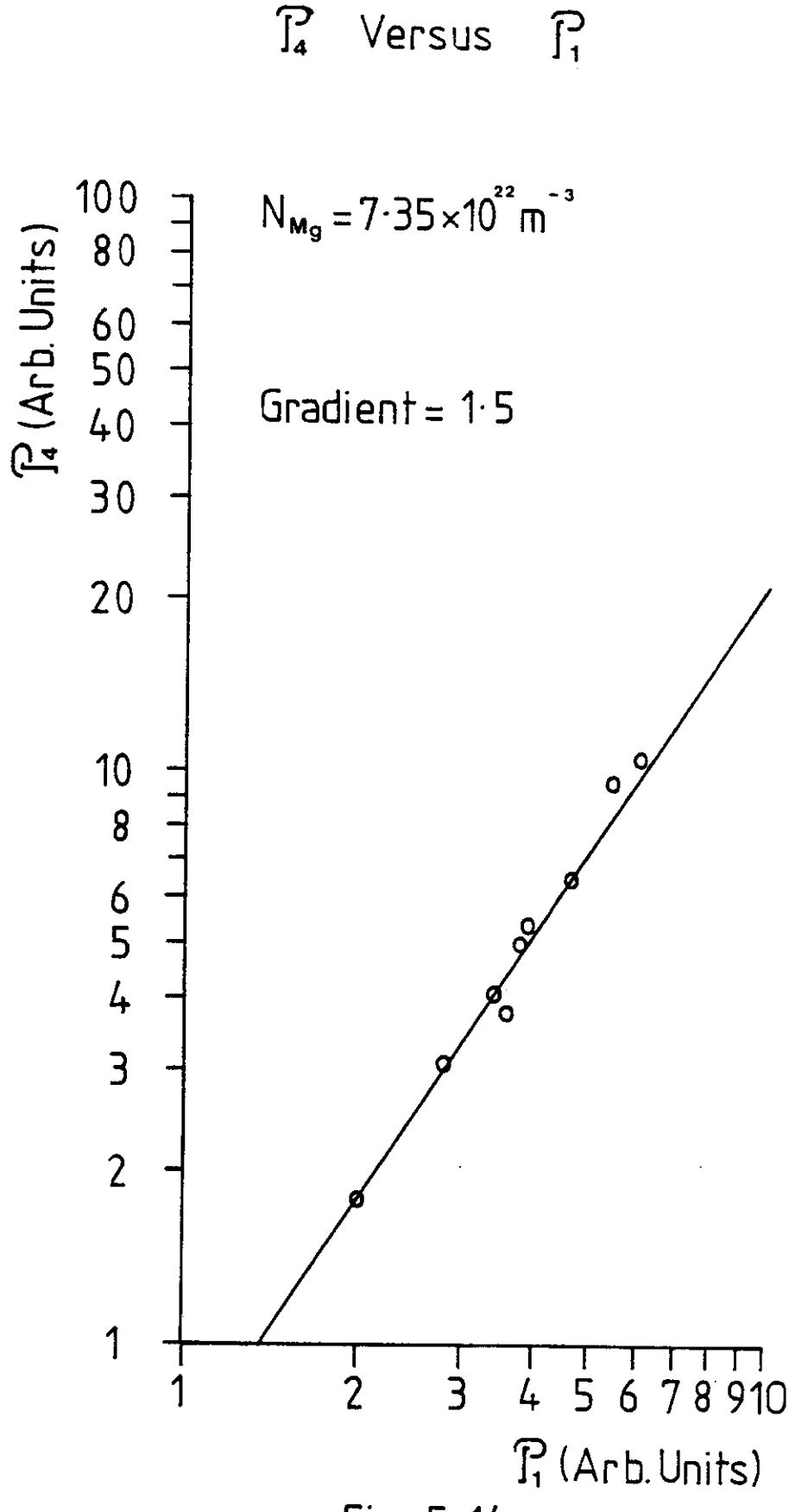
P_4 Versus P_1
$N_{Mg} = 7{\cdot}35 \times 10^{22}\ m^{-3}$
Gradient = 1·5
P_4 (Arb. Units)
100
80
60
50
40
30
20
10
8
6
5
4
3
2
1
1
2
3
4
5
6
7
8
9
10
P_1 (Arb. Units)

Fig 5-14

Relative Fourth Harmonic Power
Versus Xenon Partial Pressure

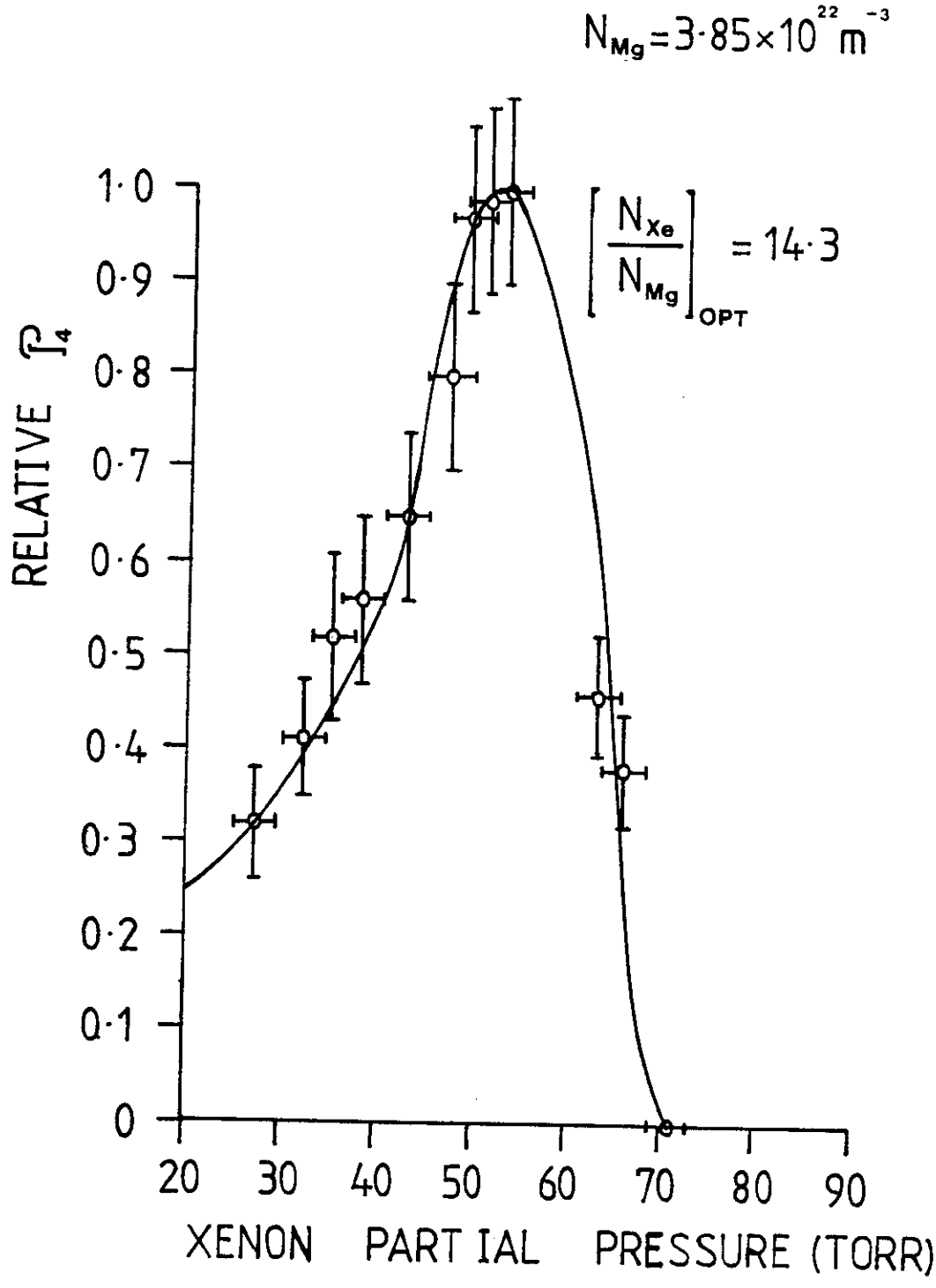

Fig 5-15

Relative Fourth Harmonic Power

Versus Xenon Partial Pressure

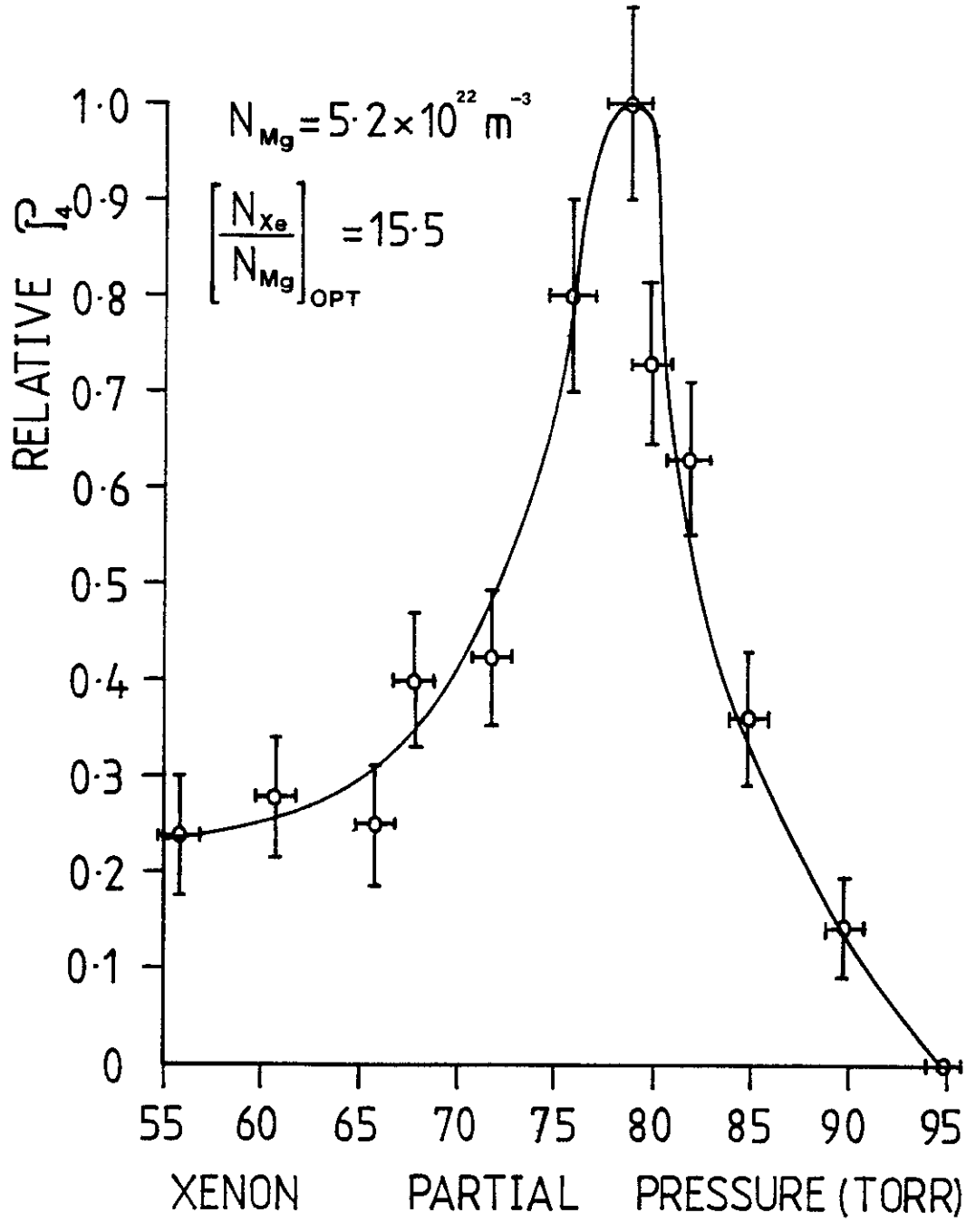

Fig 5-16

Relative Fourth Harmonic Power
Versus Xenon Partial Pressure

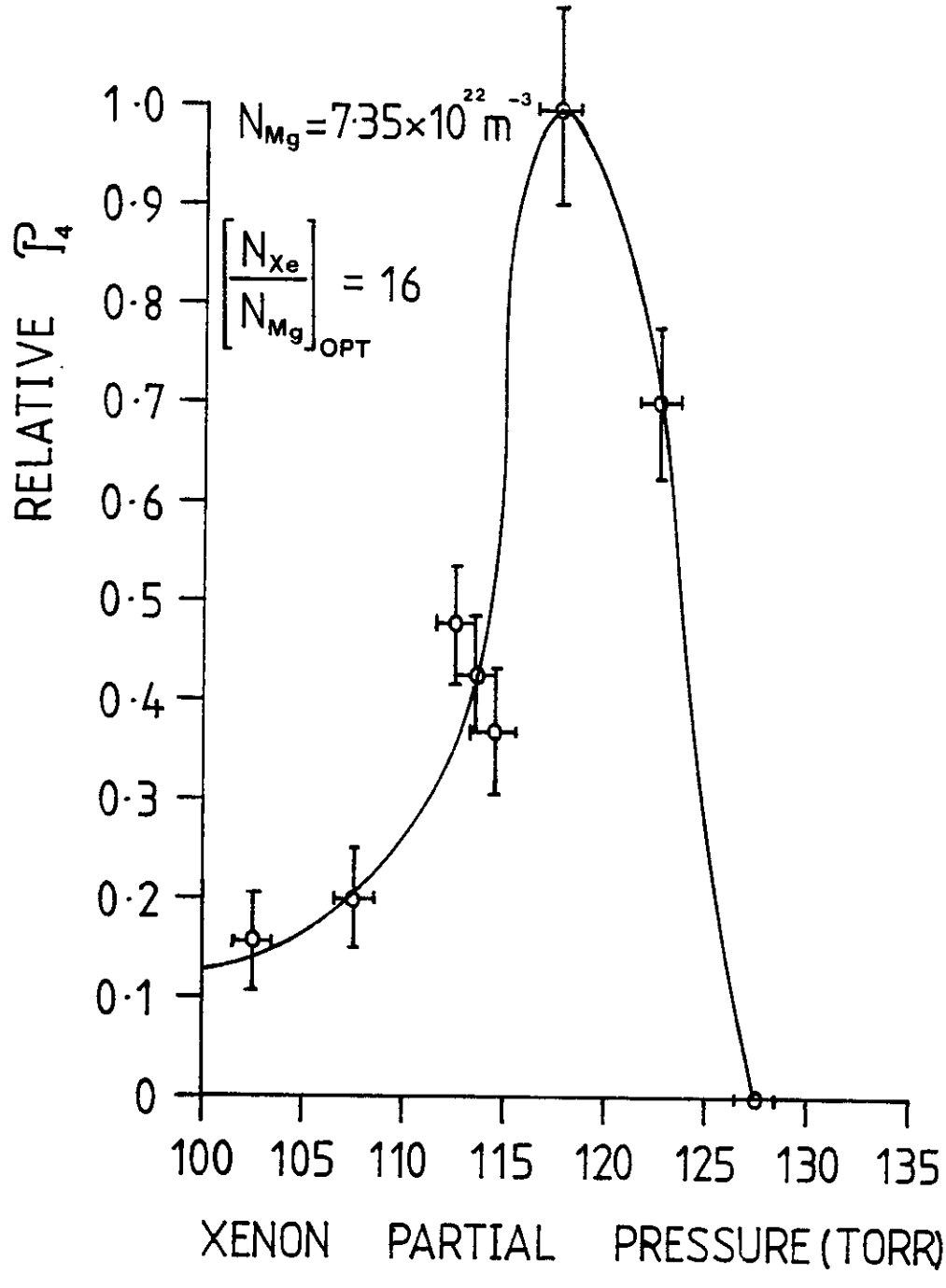

Fig 5-17

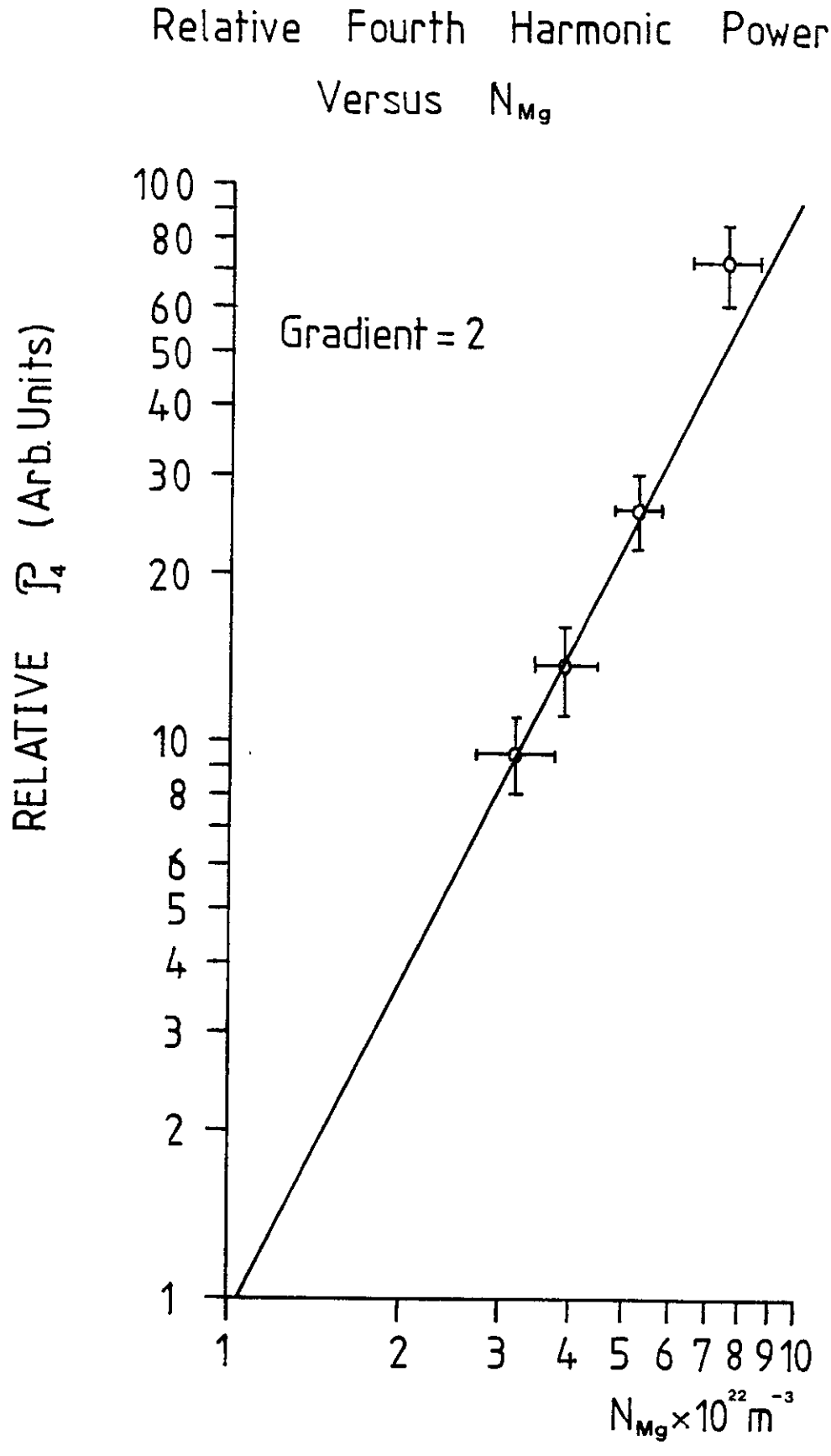
Relative Fourth Harmonic Power
Versus N_{Mg}
RELATIVE P_4 (Arb. Units)
Gradient = 2
100
80
60
50
40
30
20
10
8
6
5
4
3
2
1
1
2
3
4
5
6
7
8
9
10
$N_{Mg} \times 10^{22} m^{-3}$

Fig 5-18

This implies a power conversion efficiency of approximately 1.8×10^{-3} (or 0.18%) and a non-linear susceptibility of $5.8 \times 10^{-49} m^5 v^{-2}$, in good agreement with the earlier results. Since all the points of Figure 5-18 lie reasonably well on the line with gradient two, this value of the susceptibility is confirmed over the range of number densities used. Taking into account the errors involved in the experiment, the experimental value of the susceptibility may be quoted as $5.5\ (\pm\ 0.7) \times 10^{-49}\ m^5\ v^{-2}$.

Two scans of the relative fourth harmonic signal with temperatures for a constant xenon pressure are shown in Figure 5-19 and 5-20. Again saturation effects showed up at the temperatures for which maximum relative signal was observed.

The inconsistencies of these results with the theory of Chapter IV are discussed next.

V. Discussion of Results

From the results presented, it can be seen that at low number densities, agreement between theory and experiment is good. The power dependancies are as predicted, as are the phase matching curves. There is a disparity between the theoretical value of $\chi^{(3)}(-4\omega_1,\omega_1,\omega_1,2\omega_1)$ and the experimentally obtained one, but this value was found to be consistent at all number densities. The expected scaling of relative signal with increasing number density was also observed.

Two features of the experimental results requiring further clarification are:

a) The fall off of the power dependency of the fourth harmonic with increasing Mg number density

Relative Fourth Harmonic Power
Versus Temperature

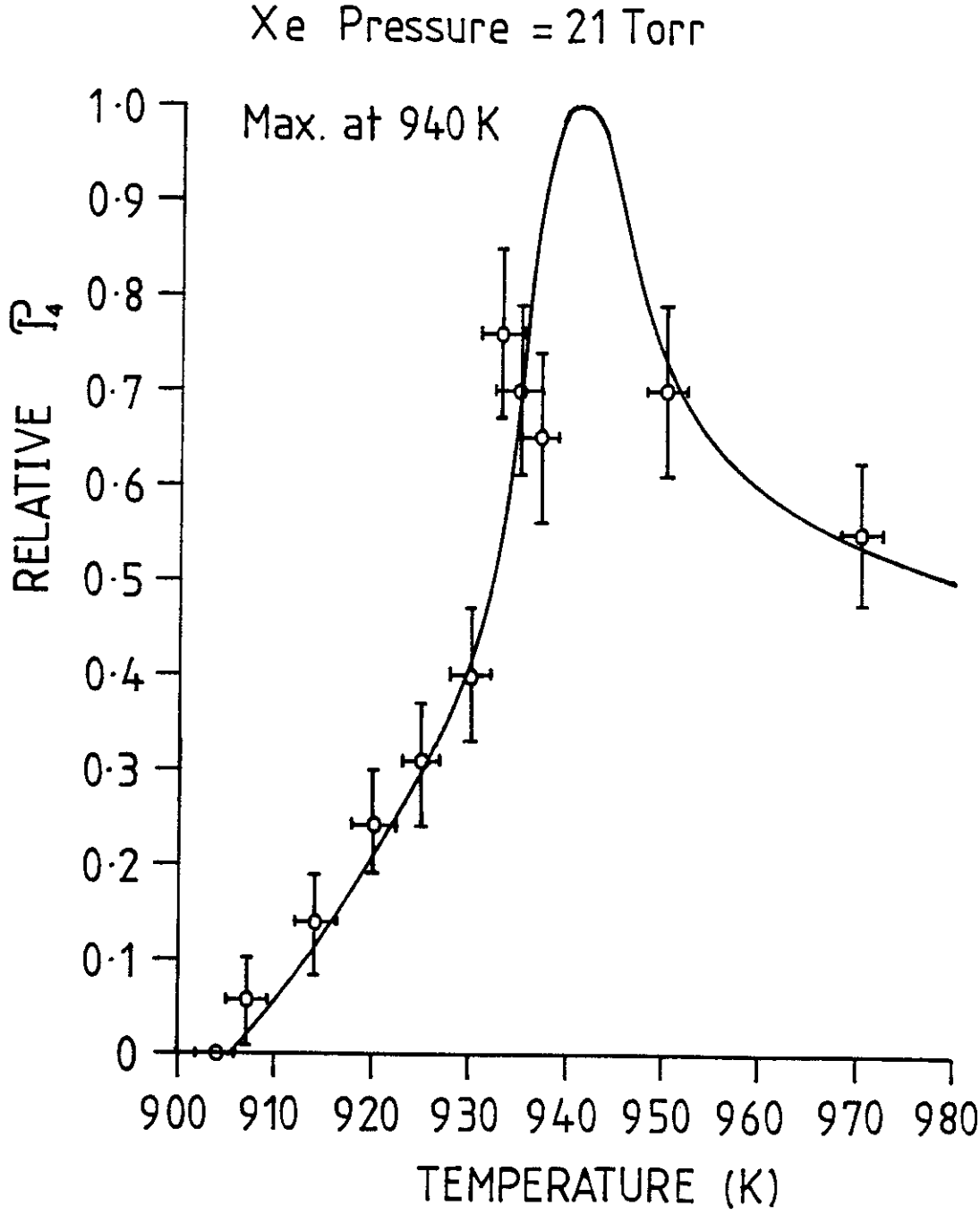

Fig 5-19

Relative Fourth Harmonic Power
Versus Temperature

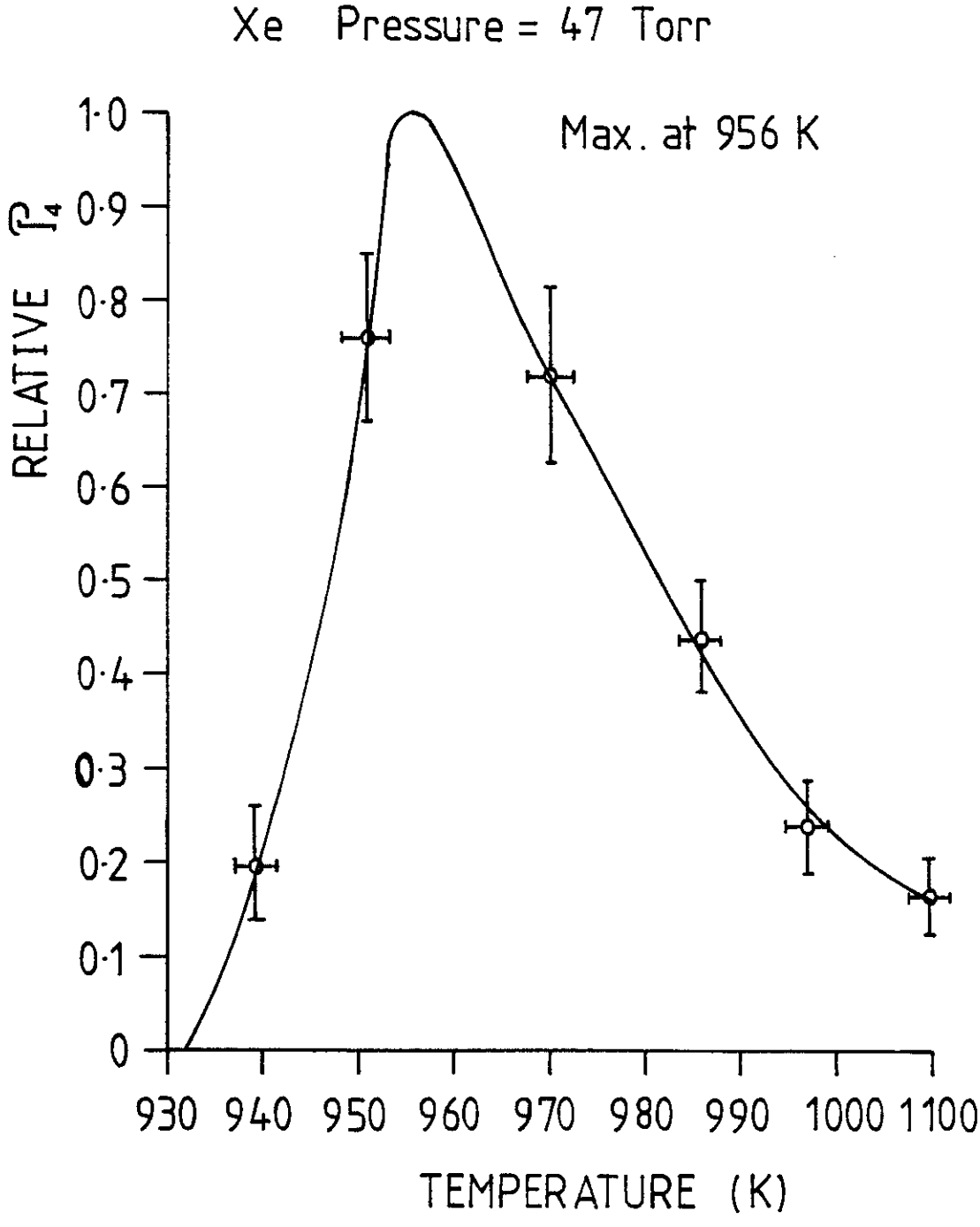

Fig 5-20

b) The low value of the susceptibility, $\chi^{(3)}$, compared to the theoretical prediction ($5.5 \times 10^{-49} M^5 V^{-2}$ compared with $6.3 \times 10^{-48} M^5 V^{-2}$).

With a maximum conversion efficiency of about 0.2%, it is unlikely that depletion of the fundamental or second harmonic beam occurs. This may not be entirely discounted due to possible absorption effects. Other workers with Magnesium[81] have found that large amounts of MgO are liberated when any test sample is heated up to the temperatures used in this work. It is thought that anything up to one third of the vapour pressure could be attributable to the presence of this impurity. MgO has broad absorption bands in the ultra-violet and vacuum-ultraviolet, so it is likely that some absorption of the second harmonic beam and the generated fourth harmonic beam will occur. Quantitative values for the absorption cross-section are sparse in the literature however, and it is difficult to put a value to either of these absorptions. This obviously will reduce the second harmonic intensity taking part in the process, and the intensity of the recorded fourth harmonic, so the conversion efficiency may well be higher than the experimentally measured one. However, a reduction in the fourth harmonic intensity of about 400 is required if depletion of the fundamental beam is to take place, and cause such a fall-off in the power dependency. An absorption of this magnitude by what would be only a few torr of gas at most seems unlikely. However, such absorption may help to explain the low experimental value of the susceptibility. In the absence of any quantitative information, it is difficult to be more precise on this point. A large absorption would also significantly affect the overall refractive index at $4\omega_1$, and change the phase matching conditions. Since at low number densities good agreement between theory and experiment was obtained, the implication is that amounts of absorbing media present in the Xe:Mg vapour mixture are small.

A possible cause of the fall off in power dependency is the intensity-dependent refractive index. A simple explanation of this effect is that, with intense fields, the ground state population is

depleted, and so the refractive index changes. The change in population across the incident beam is non-uniform because of the Gaussian distribution of intensity. Thus a radially varying refractive index profile is created which acts as a lens-like medium, and either focusses or defocusses the beam, depending on the sign of the refractive-index change. Usually the incident frequency has a refractive index greater than one, as is the case with magnesium, which decreases with depletion of the ground state. In this case a defocussing results, since the medium acts as a negative lens. This defocussing obviously will reduce the intensity of the pulse, and the most intense pulses will be affected most, leading to the fall-off observed. Since the intensity-dependent refractive index is number density dependent, its effects are more likely to become apparent at higher number densities.

Thus the defocussing is a result of the radial profile of the gaussian beam. The pulse has a temporal profile as well, and each point of this will have a different intensity from its neighbour and so experience a different refractive index change. If we write the polarisation at ω_1 by

$$P\omega_1 = \varepsilon_0 \chi^{(1)}(-\omega_1;\omega_1)\, E\omega_1 + \tfrac{3}{4}\, \varepsilon_0\, \chi^{(3)}(-\omega_1;\omega_1,-\omega_1,\omega_1)\,|E\omega_1|^2 E\omega_1 + \tfrac{5}{8}\varepsilon_0\chi^{(5)}(-\omega_1;\omega_1,-\omega_1,\omega_1,-\omega_1,\omega_1)(E\omega_1)^4\, E\omega_1 + \ldots \qquad (5\text{-}5)$$

Then the change in refractive index at ω_1 is given by [82]

$$\partial n_{\omega_1} = \frac{3/4\ \chi^{(3)}(-\omega_1;\ \omega_1,\ -\omega_1,\omega_1)\ I\omega_1}{\varepsilon_0 c\ n_0^2} \qquad (5\text{-}6)$$

where $I\omega_1$ is the intensity at the fundamental frequency. At very high intensities, the next higher order term $\chi^{(5)}$ should be included.

If the fourth harmonic field grows to a significant level, there will be an optical Kerr-effect contribution $\chi^{(3)}(-\omega_1; 4\omega_1,-4\omega_1,\omega_1)|E_{4\omega_1}|^2$ to ∂n_{ω_1}. Similarly there are contributions

$$\chi^{(3)}(-4\omega_1; \omega_1,-\omega_1, 4\omega_1)|E\omega_1|^2 \text{ and}$$

$$\chi^{(3)}(-4\omega_1; 4\omega_1, -4\omega_1, 4\omega_1)\ |E_{4\omega_1}|^2 \text{ to } \partial n_{4\omega_1}$$

There will also be changes at the second harmonic frequency, involving terms such as

$$\chi^{(3)}(-2\omega_1; 2\omega_1, -2\omega_1, 2\omega_1)\ |E_{2\omega_1}|^2 \quad \text{etc.}$$

The effect is that each point on the corresponding fourth harmonic pulse will require different conditions for phase matching and it will be impossible under any usual conditions to phase match for the entire pulse [83]. Thus in general the resulting harmonic temporal pulse will be reduced in intensity and altered in temporal profile compared to a pulse generated under perfect conditions. A full investigation of this effect requires numerical analysis, using calculations for a large number of points on the pulse, and is beyond the scope of this thesis.

A comparison between the theoretical curve of 4-6(b) and experiment (see Figure 5-21) shows that there is disagreement at higher number densities for the phase-matching ratios, these being higher than predicted. The above explanation would predict a change in the phase-matching ratios, but does not directly explain the observations. These ratios may however only reflect the unreliability of the vapour pressure data at higher pressures (the exponential behaviour is strictly only valid for pressures of around one Torr), and uncertainties in the thermocouple calibration .

$(N_{Xe} / N_{Mg})_{OPT}$ Versus N_{Mg}

— Experimental Results

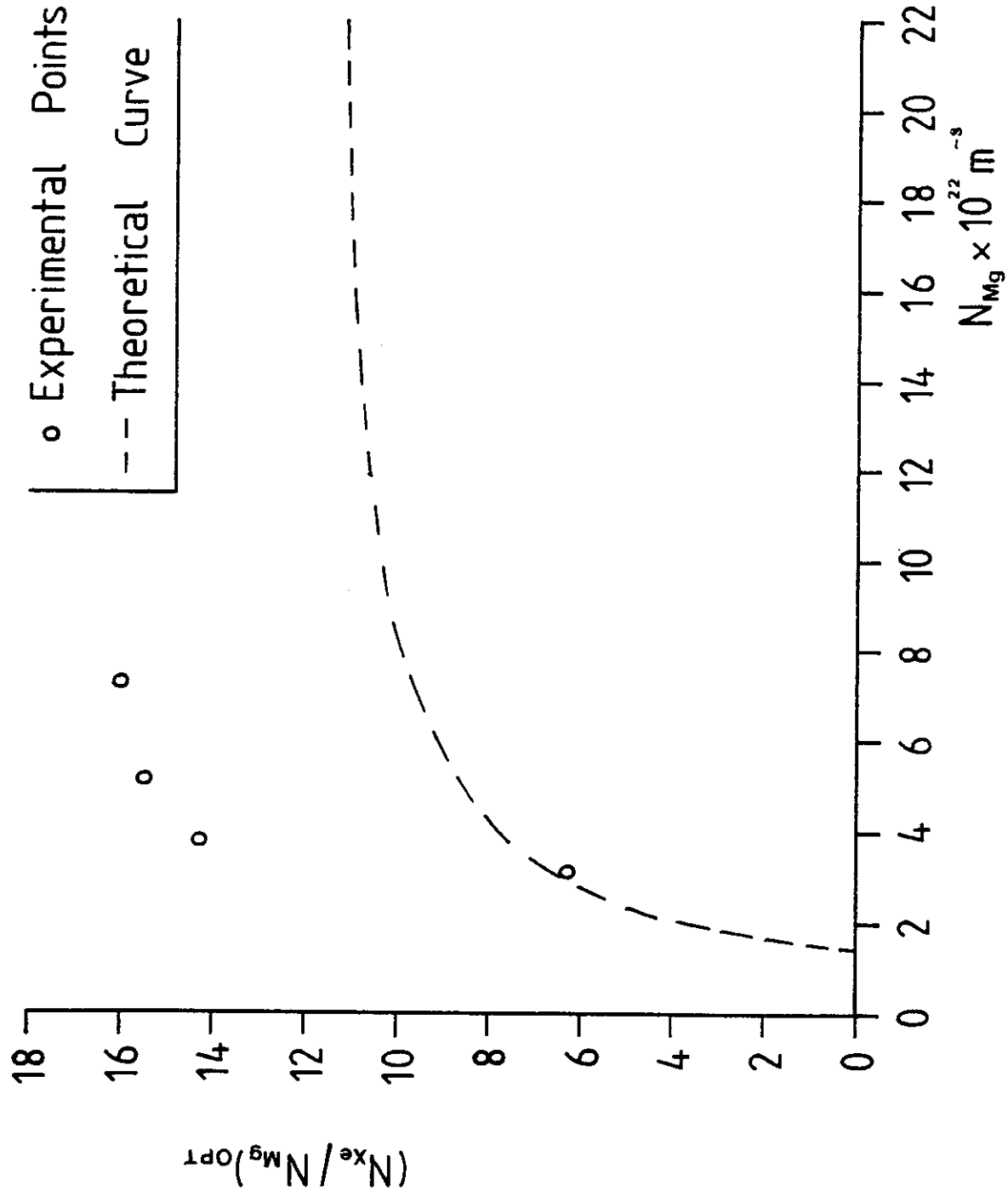

Fig 5-21

Mechanisms which can reduce the efficiency of conversion include:

a) Single photon absorption. This is probably insignificant since all frequencies considered are well away from any resonance.

b) Two photon absorption. Again this is probably small, since the two photon virtual state is $\sim 300\ cm^{-1}$ away from the atomic level.

c) Multiphoton ionisation. This may be considerable. The photon combination

$$\omega_1 + 2\omega_1 + 2\omega_1$$

is sufficient to lift one outer electron into the ionisation continuum. Other authors [84, 85] have shown that it is possible to ionise completely a 10 torr-ion column of Na vapour using only a 1 MW dye-laser beam.

d) The a.c. stark shift. This can cause considerable shifts in the energy levels and this will obviously affect the conversion efficiency via the susceptibility and the refractive index.

Finally it should be emphasised that due to the lack of phase information in the calculation of the susceptibility, the quoted theoretical value has a large error associated with it. If the smallest value is taken, it is possible that other contributions in the sum (4-40), which were not calculated, may become significant and reduce the susceptibility still further.

VI. Conclusions

It has been shown that fourth harmonic generation of ruby laser pulses in magnesium is possible, and that phase matching and relatively high conversion efficiencies (0.2%) may be achieved using a concentric heat-pipe arrangement. This conversion efficiency is as high as has been quoted by other workers in the field[18, 86, 87], and considerably higher than some. It is probably due to the very intense fields, particularly in the region of focus, employed in this series of experiments, compared to those of others (power densities of up to 2×10^{12} watts cm^{-2} were being used).

At low number densities, the behaviour was as predicted by straightforward theory, although the experimental susceptibility was lower than the theoretical value. This theoretical susceptibility ($6.3 \times 10^{-48} m^5 V^{-2}$) has a large error associated with it due to a lack of phase information. Taking into account the known errors in the experiments, a value for the susceptibility of $5.5 (\pm 0.7) \times 10^{-49}$ m^5 V^{-2} was deduced. At higher number densities (73.5×10^{22} m^{-3}) saturation effects were observed and it is believed that these were due mainly to the intensity-dependent refractive index variations in the magnesium vapour, which affected the overall index at 6943 Å and 3471.5 Å. This effect is one of the few saturation mechanisms which is both number density dependent, and intensity dependent.

This experimental method is thus capable of producing fourth harmonic pulses of high power (up to 3×10^5 Watts). For increased reliability, a more demountable heat-pipe design is required. A higher repetition-rate source at 6943 Å and 3471.5 Å is also a necessity for more detailed and searching investigations into this process.

CHAPTER 6

APPLICATIONS OF THE FOURTH HARMONIC

I. Introduction

One of the potentially most interesting applications of the fourth harmonic pulses which have been generated is their possible amplification in an inverted Xe_2^* medium. At the present time Xe_2^* cannot be mode-locked, for two main reasons. The first is the fact the upper state lifetime is so short that the Xe_2^* lases only for the duration of the pumping pulse (which is a relativistic electron beam). There are no suitable pump sources at the present time of sufficiently long duration for mode-locking to build up. Secondly there are no suitable dyes available which exhibit saturable absorption in the vuv.

Consequently, the only way of obtaining picosecond pulses from xenon is to use it as an amplifier for injected pulses. Furthermore, it may be anticipated that by using xenon in such a way, information may be obtained about the nature of the broadening (homogeneous or inhomogeneous) that occurs on a picosecond time-scale. A fuller description of the xenon molecule and the principles behind such an amplification experiment are given in the next section. The third section deals with the way such an experiment may be carried out, and its feasibility using the equipment described in this work is then assessed in the final section. Other possible applications are briefly outlined.

II. Brief Background Theory

II-1 Structure of the Xenon Molecule

Houtermans[88] was the first to realise that transitions from bound molecular states to loosely bound states could be exploited for laser action. Two distinct advantages are offered by a transition from a bound to a dissociative state in diatomic molecules. Firstly, if the final (ground) state is strongly repulsive, then this lower state will remain almost unpopulated, the ground state of the molecule flying apart as it is formed. Secondly a broad band emission results because of the repulsive ground state and the laser is thus tunable over a wide range.

Basov[89] first proposed the use of xenon to achieve vuv laser action, the ground molecular state potential being repulsive due to the "closed shell" structure of the ground state atoms[90]. By colliding an excited state atom with a ground state atom a stable bound molecule can be formed. The transitions from this molecule to the ground state result in a broad continuous emission spectrum around 170nm. Figure 6-1 shows the potential curves of xenon. The ground state atoms of xenon have the configuration $(\ldots 5s^2\ 5p^6)\ ^1S_0$, which results in a repulsive ground state except for a weak Van der Waal's force. By exciting one of the $5p^6$ electrons to the first s orbital, the configuration $5s^2\ 5p^5\ 6s$ is obtained, which gives rise to four atomic states: $^3P_1$, $^3P_2$, $^1P_1$, and $^3P_0$. Although L-S coupling notation is used here, the coupling is in fact j-j with the spin-orbit interaction of the five p electrons dominating the spin-spin interaction between 6s and $5p^5$.

The $^3P_1$ and $^1P_1$ states both radiate to the ground state ($^1S_0$) with lifetimes of about 4 ns[91], with wavelengths of 147 nm and 129 nm respectively. The other two levels cannot radiate due to the selection

POTENTIAL CURVES OF XENON

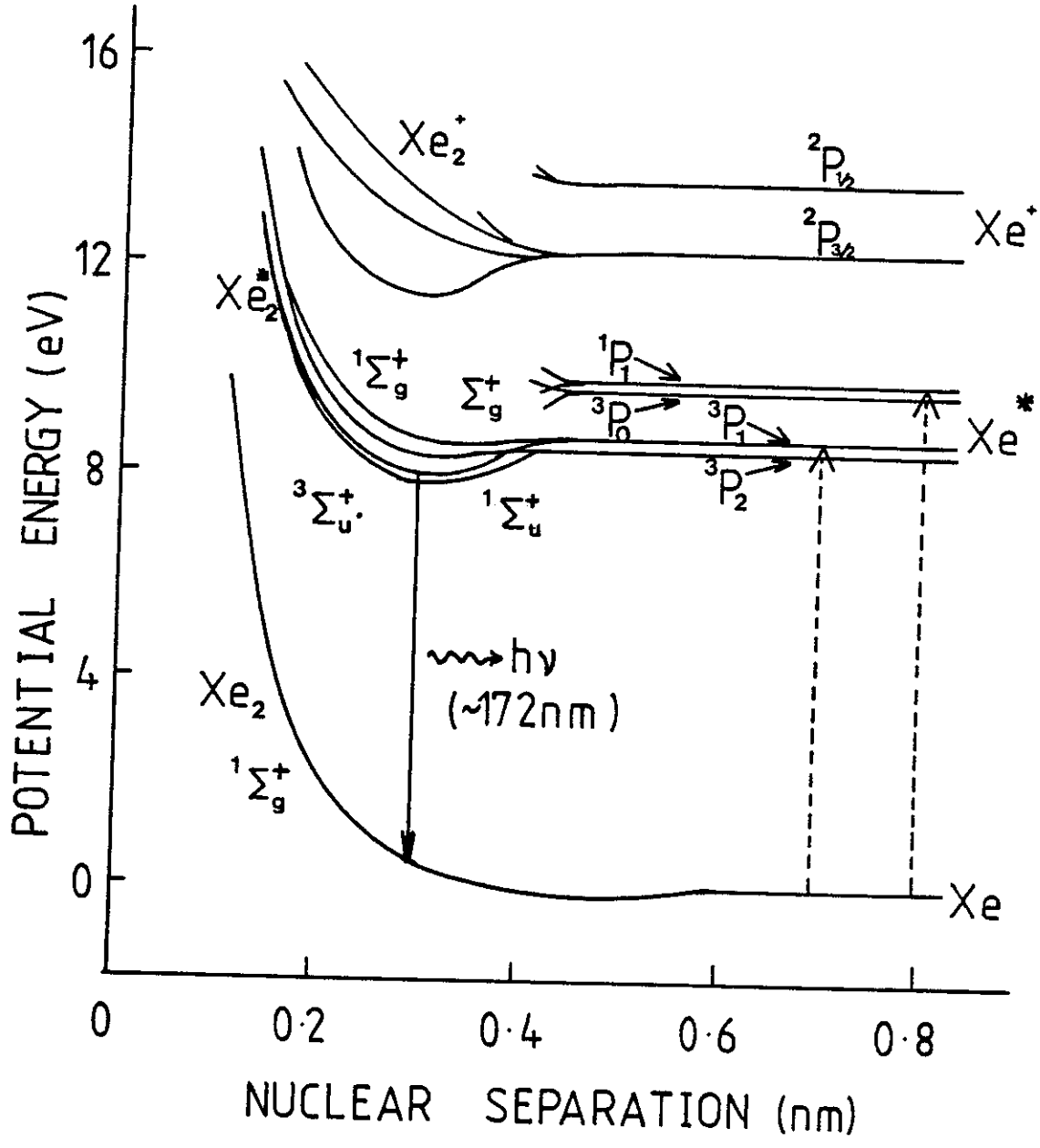

----- Atomic Resonance Lines
At 147·0 and 129·6nm

Fig 6-1

rule

$$\Delta J = 0, \pm 1 \qquad \text{and } J = 0 \not\leftrightarrow J = 0.$$

Collision of atoms in the $^3P_1$ and $^3P_2$ states form the $^1\Sigma_u^+$ and $^3\Sigma_u^+$ states of the xenon molecule respectively. Hund's case (c) coupling is applicable[92], and consequently the selection rule $\Delta S = 0$ is not strictly obeyed. In this case, the triplet state, as well as the singlet, may radiate to the $^1\Sigma_g^+$ ground state.

Transitions from the high vibrational levels of the $^1\Sigma_u^+$ and $^3\Sigma_u^+$ states to the $^1\Sigma_g^+$ ground state result in the so-called "first continuum". The "second continuum" is due to transitions from the lower vibrational levels of these states, and is favoured at higher pressures. This is because molecules in high vibrational levels are collisionally relaxed to the lower vibrational levels by ground state atoms. At the typical operating pressures for the xonon laser (5 to 15 ktorr) only the second continuum is observed. These high pressures are required to make the formation and relaxation processes of the excited molecule fast compared to the fluorescence decay time[93].

II-2 Formation Processes

It may be shown[93] that the majority of the species formed as a result of the interaction of high energy electrons with high pressure xenon gas are ions. The atomic ion is removed in the 3-body reaction

$$Xe^+ + 2\ Xe = Xe_2^+ + Xe \qquad (6\text{-}1)$$

The formation rate (which is proportional to the square of the pressure) was measured by Smith et al.[94] to be 3.6×10^{-31} cm^6 sec^{-1}.

The molecular ions are then in turn removed by dissociative recombination

$$Xe_2^+ + e = Xe^{**} + Xe \qquad (6\text{-}2)$$

where Xe^{**} is a highly excited atomic state. Bates[95] first proposed this type of process in an attempt to account for the fast ionic recombination observed in certain species. These atoms are then thought to radiatively decay to the $^3P_2$ or $^3P_1$ states:

$$Xe^{**}(^2P_n) = Xe^* (^3P_2 \text{ or } ^3P_1) + h\nu \qquad (6\text{-}3)$$

These lower states may also be filled after collisions with electrons or ground state atoms:

$$Xe^{**} + e \text{ (or Xe)} = Xe^* + e \text{ (or Xe)} \qquad (6\text{-}4)$$

Electron-induced reactions have been used in models for fluorescence from high pressure xenon developed by Georges et al.[97].

The molecular states $^1\Sigma_u^+$ and $^3\Sigma_u^+$ are then formed via the 3-body reaction

$$Xe^* + 2\,Xe = Xe_2^* + Xe \qquad (6\text{-}4)$$

and both these states can radiate to the ground state.

The role of these two states is still the subject of some controversy. Earlier studies assumed only a single radiative decay rate and formation rate[98], but later experimental results indicated two

separate radiating levels may occur[99]. In modeling fluorescence from xenon, Fournier [97] assumed values of 4nsec and 16nsec for the lifetimes of the two radiating levels and a different formation rate for the singlet and triplet. The cause of the shift in the peak of the spectrum towards the red with increasing pressure[93,99] is still not exactly understood. Koehler et al.[99] and Gerado et al.[100] suggested firstly that the shift was due to increasing absorption from the ground state molecules. However, it could also be due to the distribution of the population in the upper state[101], which is determined by vibrational relaxation in collision with ground state atoms [102], and subsequent mixing of the $^1\Sigma_u^+$ and $^3\Sigma_u^+$ states.

The xenon molecules are originally formed in high vibrational levels, which at high pressures relax to the lower vibrational states:

$$Xe_2^*(\nu_i) + Xe = Xe_2^*(\nu_f) + Xe + \Delta E \qquad (6\text{-}5)$$

where
$Xe_2^*(\nu_i)$ denotes the molecules in the intial vibrational state
$Xe_2^*(\nu_f)$ denotes the molecules in the final vibrational state

ΔE is the energy which is carried away with the ground state atom.

Fink et al.[102] estimate the rate constant for vibrational relaxation out of the initial levels to be $6.6 \times 10^{-10} \tau_f^{-1}$ cm sec^{-1}. For a pressure of 10 ktorr and a lifetime of 10 nsec[93], the vibrational relaxation time should be about 40 psec.

II-3 Amplification and Requirements for Saturation

It is well established now [93,103] that there is gain over about 80 Å in xenon, centred on ∿ 172 nm. Evidently pulses of 1735.35 Å

will experience amplification on passing through an inverted Xe_2^* medium. To measure the vibrational relaxation time, it is first necessary to saturate the gain at some point in the xenon cell, and then monitor the build up of gain. For picosecond pulses, the saturation intensity (required to deplete the population inversion to e^{-1}) is given by

$$I_s = \frac{h\nu}{\sigma\tau} \qquad (6\text{-}6)$$

where ν = frequency of the pulse

σ = cross-section for transferring molecules out of the excited state (either by stimulated emission or photo-ionisation)

τ = duration of the pulse

Using a value for the photo-ionisation cross-section of $\sim 4.2 \times 10^{-18} cm^{-2}$, and a value for the stimulated emission cross-section of $\sim 7 \times 10^{-18}\ cm^{-2}$, gives a saturation power density of

$$I_s = 10^{10}\ W/cm^2 \qquad (6\text{-}7)$$

assuming a pulse duration of 10 psec. This is the intensity which must be reached, in order that the vibrational relaxation time may be measured.

III. The Proposed Experiment

The schematic of a possible experimental arrangement for amplification is shown in Figure 6-2. A Febetron 706 would be used to pump the xenon, in the coaxial arrangement described by Hull[93].

Proposed Arrangement For Amplification

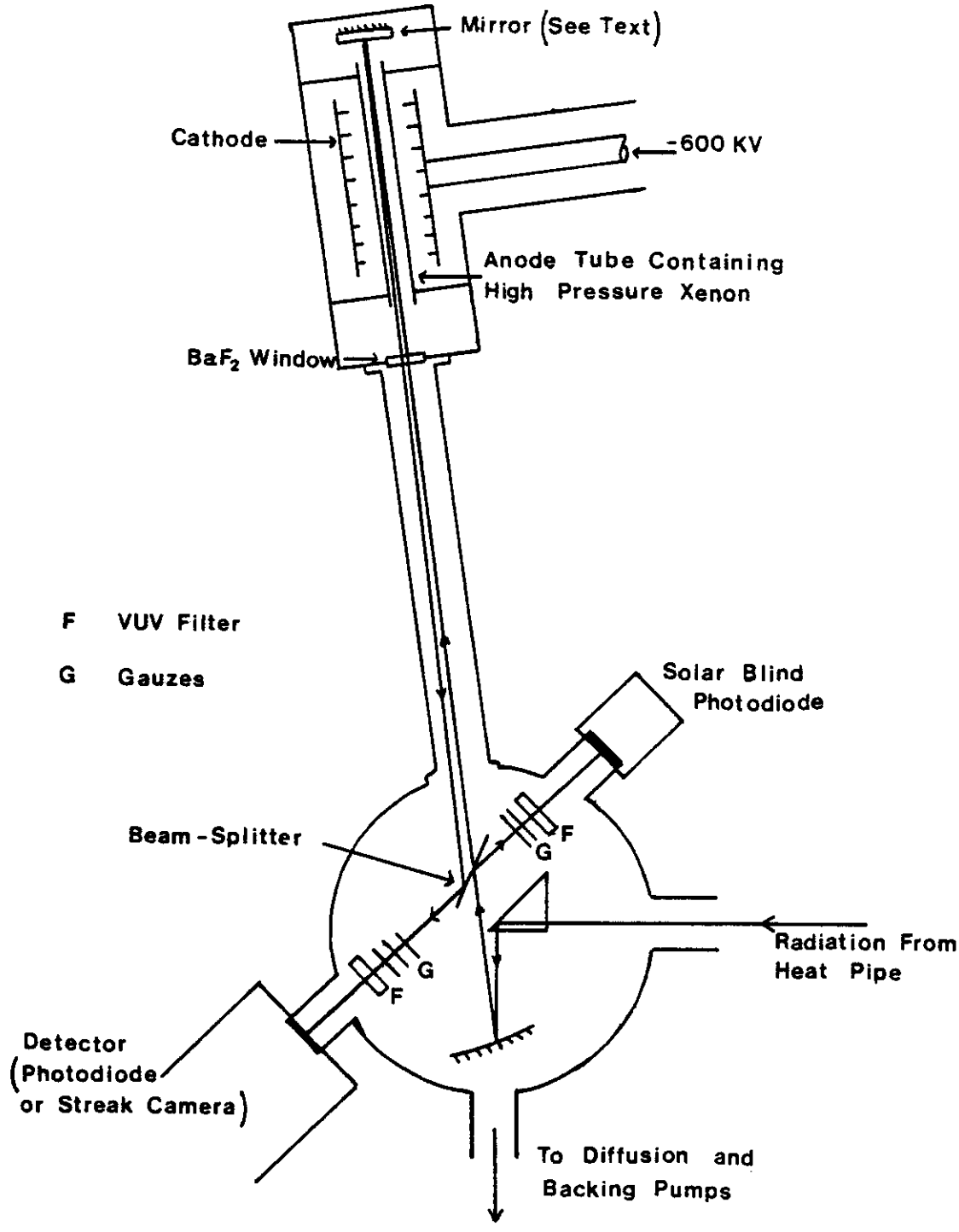

Fig 6-2

The anode tube is 4 mm in diameter and has an excited length of 12 cm. A gain of 0.2 cm^{-1} may be expected using the Febetron, which, with a Blumlein arrangement, delivers a 5 nsec pulse of 0.5 MeV electrons, and thereby deposits $\sim$ 10 Joules into the gas. Using a mirror to focus the fourth harmonic pulses into the xenon, it may be expected that they will be sufficiently powerful to saturate the gain at the point of focus on the return trip.

The curved mirror at the end of the anode tube, as depicted in Figure 6-2, has a 50% reflecting front face and a 100% reflectivity back face (at 1735 Å). Its function is to return a set of sub-pulses, of known relative intensity and separation, along the gain length. Hopefully the leading pulse will saturate the gain at the focus, and the following pulses, as observed on a streak camera, should indicate the rate of build-up of gain by their relative intensities, and thus give a measure of the vibrational relaxation time.

A mirror is used to steer the beam into the xenon since its focal length is precisely known. Using a lens would give the additional complication of an uncertainty in the position of focus, since the refractive indices are not accurately known at vuv wavelengths. The prism is used to steer the beam through a right angle so that it is incident on the focussing mirror at a small ($\sim 5^{\circ}$) angle of incidence, which makes astigmatism negligible.

Obviously it is necessary to synchronise the firing of the Febetron 706 so that fourth harmonic pulses are travelling along the anode tube length when there is gain in the xenon. The suggested method here is to use the red filter in front of the oscillator's rear mirror as a beam splitter, and to monitor the build-up of mode-locking using a photo-diode and 519 oscilloscope combination. By altering the number of neutral density filters infront of this photo-diode, the oscilloscope may be triggered up to several hundred nanoseconds

before the mode-locked train proper emerges from the oscillator.

The output gate of the oscilloscope may then be used to trigger a Krytron Box. It is suggested that a stacked krytron configuration should be used, consisting of two KN 22 krytrons in series, which can hold off up to 10 KV. By switching this voltage onto a Blumlein, the resultant voltage is large enough to trigger the first spark gap in the Marx bank of capacitors in the Febetron. Preliminary investigations have indicated that this triggering mechanism works, and sufficient delay is obtainable for synchronisation to be possible.

IV. Conclusions

Although the experiment as described above is possible in principle, there are severe limitations on its practical realisation, due to the various behavioural characteristics of the available equipment. Perhaps the most important of these is the jitter in the firing of the Febetron 706. The variation in the time at which the voltage pulse appears at the cathode is $\pm$ 75 nsec, which is to be compared with a fourth harmonic pulse train length of approximately 100 nsec or less. Additionally, the duration of the gain is about the same as that of the pumping pulse, i.e. 5 nsec, which is half the separation of fourth harmonic pulses. This means that even if the pumping pulse occurs somewhere in the fourth harmonic pulse train, there is still a good chance that it will fail to amplify a pulse.

The situation is made worse by the fact that the system cannot be fired more than once every fifteen minutes, due to the requirement that the gas be cooled. As mentioned in Chapter 5, the heat pipe may be run for a maximum of about five hours, so the number of shots is limited to about twenty in a "run" before the magnesium has to be

replaced. Obviously this means that acquisition of data will be very slow.

Some of these difficulties may be overcome if a higher repetition rate system were developed. There is available a high repetition rate xenon laser, capable of firing twice a second [103], which might be used, if the ruby oscillator and amplifier system could be used to run at a higher rate. The problem with the jitter still remains, but this would be balanced by the huge increase in the number of shots it would be possible to make in a "run". It must be concluded that with the present equipment described in this thesis, however, such an experiment would be probably unfruitful.

The pulses generated have possible uses in other areas. Having a photon energy of 7 eV, the pulses may have applications in photo-fragmentation spectroscopy. Most bands in large organic molecules found in plant and human tissue may be broken with light of this energy. The analysis of the fragments produced may then reveal the structure of these molecules.

The frequency generated is sufficiently high for diagnostic purposes in high density plasmas. The plasma frequency ω_p [104] is the frequency which must be exceeded if a phton is to propagate through the plasma. The ω_p for the fourth harmonic corresponds to an electron density of about 3×10^{22} cm^{-3}. Thus scattering measurements could be made on very high density plasmas.

GENERAL CONCLUSIONS

The development of a reliable, mode-locked ruby oscillator has been described. This laser is capable of delivering a train of single pulses, having a peak power of 15 MW, with a success rate of between 80% and 90%. The pulses have been shown to be between 15 psec and 30 psec in duration, and are unbroadened by non-linear effects before the middle of the train. Pulses after the middle of the train broaden gradually to about 40 psec on average (for a saturable dye transmission of 70%). Such a high degree of reproducibility was achieved by very tight control of the operating parameters, in particular the voltage on the capacitor bank, and the temperature of the cooling water. Temperature control of the saturable dye was also shown to significantly improve the reproducibility. This latter refinement for improving the performance of a passively mode-locked ruby laser has not been mentioned in the literature.

By employing a single stage amplifier, peak powers in the pulse train in excess of 200 MW were obtained, and the system was then considered to be of sufficiently high quality to perform harmonic generation studies. Many different types of non-linear processes should be accessible to study with this system. Second harmonic generation in a A.D.P. crystal was observed, and the conversion efficiency was estimated to be about 2%. This process provided a source of coherent light in the uv.

Fourth harmonic generation in Mg vapour was also extensively studied. This process used the second harmonic and fundamental pulses, and was investigated theoretically and experimentally. Good agreement

between the theoretical predictions and experimental observations were obtained at low Mg atomic number densities. Here the scaling of the fourth harmonic intensity with that of the fundamental was as expected, and phase matching curves were in close agreement with the theoretical shapes. It was found that the power dependencies deviated from theoretical predictions for high Mg atomic number densities, but phase-matching was still observed (though not at the predicted partial pressure ratios for Xe and Mg). The scaling of the fourth harmonic signal with number density was as predicted for all number densities. An experimental value for the fourth harmonic susceptibility $\chi^{(3)}$ $(-4\omega_1;\omega_1,\omega_1,2\omega_1)$ of $5.5\ (\pm\ 0.7) \times 10^{-49}\ m^5V^{-2}$ was inferred from the data. This disagreed with the theoretical value of $6.3 \times 10^{-48}\ m^5\ V^{-2}$.

It was concluded that the low value of the susceptibility probably reflected the lack of knowledge of the phases of the individual terms in the theoretical calculation. The drop in the observed power dependencies was thought to be attributable largely to intensity-dependent refractive index effects in the Mg vapour. At the highest number densities, a conversion efficiency of about 0.2% was achieved (from fundamental to fourth harmonic) and this process then provided a source of intense (0.3MW) radiation in the vuv.

It has been shown further that amplification of these pulses in Xe_2^* should be possible, and a measure of the vibrational relaxation time of the upper state could then be obtained. It was, however, concluded that with the present repetition rate of the ruby system, the jitter and duration of gain in the xenon system would prove large obstacles to the practical realisation of this proposal. If amplification is possible, the pulses may then be used in further non-linear processes, which should produce coherent radiation in the soft X-ray region of the spectrum.

APPENDIX

NUMERICAL EVALUATION OF $|I(\Delta k,\xi,\zeta)|^2$ FOR THE EXPERIMENTAL PARAMETERS

As indicated in Chapter 4, the integral

$$F(b\Delta k,\ b/L,\ f/L) = \left| \int_{-\zeta}^{\xi} \frac{\exp\{-(ib/2)\Delta k\xi'\}d\xi'}{(1+i\xi')^2} \right|^2 \qquad \text{(A-1)}$$

may only be evaluated analytically in the tight-focussing limit, in which case both ξ and ζ tend towards infinity. If this limit is not applicable for the experimental prameters used, then the integral must be calculated numerically. For the experiments described in this thesis, the length of the Mg vapour column was estimated to be $\leq$ 9 cm. Using Equation (4-14) and a value for the beam waist radius at the achromatic doublet of $\sim$ 2 mm, the confocal parameter b was calculated to be 2.15 cm, thus giving a value for b/L of $\sim$ 0.25. To evaluate the integral for this value, a computer program was used which employed a fast Fourier transform (FFT) algorithm.

It is noted that if the substitution

$$2\pi k' = \frac{b\Delta k}{2} \qquad \text{(A-2)}$$

is performed in (A-1), then the integral has the form of the Fourier transform of the function

$$\frac{1}{(1+ i\xi')^2} \qquad \text{(A-3)}$$

All that is then required is to perform a discrete Fourier transform on the computer. Using the notation H(n/ND) for the approximation to the continuous Fourier transform H(k'), and h(kD) for the function to be transformed h(ξ'), we have[105]

$$H\left(\frac{n}{ND}\right) = D\sum_{k=0}^{N-1} h(kD)\ \exp\ \{-i2\pi mk/N\} \qquad (A\text{-}4)$$

$$n = 0,1, \ldots N-1$$

where D is the size of each element in the spatial mesh, and N is the total number of elements. A value of N = 4096 was chosen, and a value for the total length X (= ND) of 40π. This meant that at the end of the program, when all the real and imaginary elements of (A-3) in the spatial array had been replaced by frequency components labelled by n, that the separation of each frequency element was $1/40\pi$

$$\text{i.e. } k'_{n+1} - k'_n = 1/40\pi \qquad (A\text{-}5)$$

or, using (A-2)

$$(b\Delta k) = 0.1 \qquad (A\text{-}6)$$

Thus the $b\Delta k$ values ran in discrete steps of 0.1, which was the resolution required in order that comparison with experimental results could be done.

The program sets up the real and imaginary parts of the function (A-3) on the spatial mesh such that the function is centred on the middle of the mesh. When the FFT has been performed, all the elements on the spatial mesh have been replaced by frequency components. The second half of the mesh then corresponds to the negative frequencies, running from zero at the centre to more negative values (going from left

to right). Swapping the two halves of the frequency array around gives the correct sequential order for the $b\Delta k$ values. When these values are printed out, only one hundred element values either side of $b\Delta k = 0$ are used, since all other values are very close to zero. The two values A and B in the program determine the limits between which the function (A-3) is transformed, i.e. which value of b/L is chosen.

The program was first run with the function (A-3) being evaluated and transformed over the entire length $X(= 40\pi)$, which should give output approximating to the analytical solution. This was found to be the case, agreement being to four decimal places between analytical and numerical solutions. Values of $b/L = 0.3$ and $b/L = 0.25$ were then used. Output for $b/L = 0.3$ agreed well with Bjorklund's results (Figure 4-2(b)). This indicated that the program gave accurate results. Using the $b/L = 0.25$ value gave output, having a maximum of 5.78 at $b\Delta k = -2.1$, which was in very good agreement with the experimental results (see Figure 5-10). The graphs for $b/L \simeq 0$, 0.25 and 0.3 calculated using this program are given in Figure A-1. A copy of the print-out of the program follows.

The algorithm for the FFT was taken from Brigham[105], who discusses it thoroughly. It is not intended to reproduce the text here. Note that these findings indicate that $(b\Delta k)_{OPT} = -2.1$, and so the theory presented in Chapter 4, Section IV is subject to a 5% error. With this adjustment, agreement between theory and experiment is practically exact at low number densities.

Numerical Calculations For F(bΔk, b/L, f/L)

(f/L = 0·5)

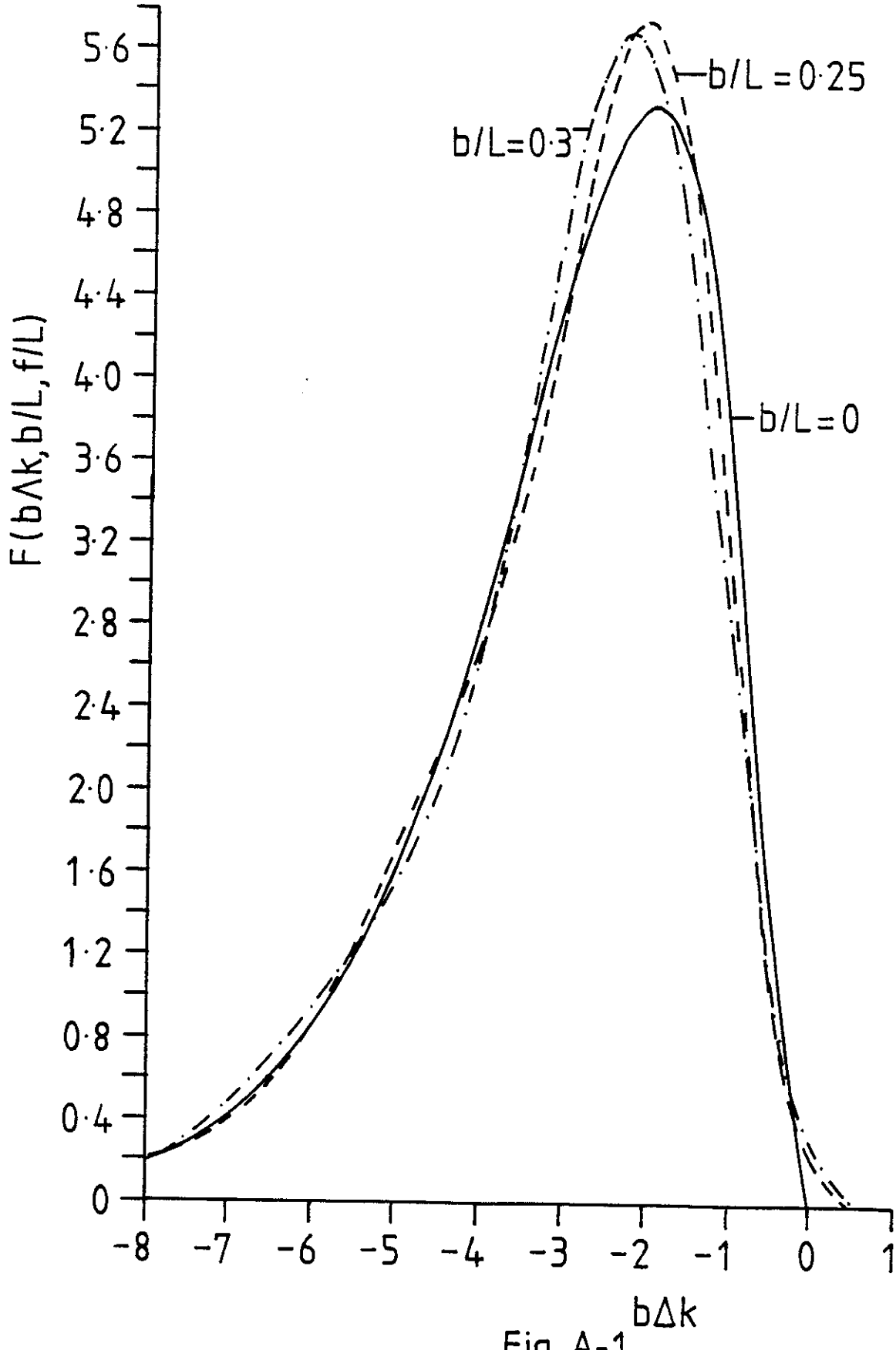

Fig A-1

```
      PROGRAM INTEGRL(OUTPUT,GRAPH,TAPE 6=GRAPH)
      DIMENSION XREAL(4096),XIMAG(4096),XSUM(4096),SDELK(200),F(200)
      IFM03=-1
      A=52.83185308
      B=72.83185308
    5 N=4096
      IF803=IF803+1
      NU=12
      X=40*3.141592654
C     X IS THE LENGTH OVER WHICH INTEGRATION IS PERFORMED
      DELTA=X/FLOAT(N)
C     DELTA IS THE INCREMENT FOR EACH STEP
C     COMPUTE XREAL ,XIMAG ARRAY FOR INPUT TO SUBROUTINE
      EXT=DELTA
      DO 10 I=1,N
      IF(EXT.GE.A.AND.EXT.LE.B)GO TO 20
      XREAL(I)=0.0
      XIMAG(I)=0.0
      GO TO 10
   20 T=EXT-(20*3.141592654)
      XREAL(I)=(1-(T**2))/((1+(T**2))**2)
      XIMAG(I)=(-2.0*T)/((1+(T**2))**2)
   10 EXT=EXT+DELTA
C     NOW CALL SUBROUTINE TO PERFORM FOURIER TRANSFORM
      CALL FFT(XREAL,XIMAG,N,NU)
      DO 30 I=1,N
      XREAL(I)=DELTA*XREAL(I)
      XIMAG(I)=DELTA*XIMAG(I)
   30 XSUM(I)=((XREAL(I)**2)+(XIMAG(I)**2))
C     NOW SWAP LAST HALF OF FREQUENCY ARRAY AROUND
      NTWO=N/2
      DO 40 I=1,NTWO
      J=I+NTWO
      XREALI=XSUM(J)
      XSUM(J)=XSUM(I)
   40 XSUM(I)=XREALI
      NMIN=NTWO-100
      DO 50 I=1,200
      L=I-1
      SDELK(I)=-10.0+(0.1*FLOAT(L))
      NMI=NMIN+I
   50 F(I)=XSUM(NMI)
      CALL GRAPIC(SDELK,F,200)
      DO 70 I=1,200
   70 WRITE(6,60)I-1,SDELK(I),F(I)
   60 FORMAT(I4,3X,F5.2,3X,F9.6)
      A=56.32022518
      B=59.34438093
      IF(IF803.EQ.0)GO TO 5
      STOP
      END
      SUBROUTINE FFT(XREAL,XIMAG,N,NU)
      DIMENSION XREAL(N),XIMAG(N)
      N2=N/2
      NU1=NU-1
      K=0
      DO 100 L=1,NU
  102 DO 101 I=1,N2
      P=IBITR(K/2**NU1,NU)
      ARG=6.283185*P/FLOAT(N)
      C=COS(ARG)
      S=SIN(ARG)
      K1=K+1
      K1N2=K1+N2
      TREAL=XREAL(K1N2)*C+XIMAG(K1N2)*S
      TIMAG=XIMAG(K1N2)*C-XREAL(K1N2)*S
      XREAL(K1N2)=XREAL(K1)-TREAL
      XIMAG(K1N2)=XIMAG(K1)-TIMAG
      XREAL(K1)=XREAL(K1)+TREAL
      XIMAG(K1)=XIMAG(K1)+TIMAG
  101 K=K+1
      K=K+N2
      IF(K.LT.N) GO TO 102
      K=0
      NU1=NU1-1
  103 N2=N2/2
      DO 105 K=1,N
      I=IBITR(K-1,NU)+1
      IF(I.LE.K) GO TO 103
      TREAL=XREAL(K)
      TIMAG=XIMAG(K)
      XREAL(K)=XREAL(I)
      XIMAG(K)=XIMAG(I)
      XREAL(I)=TREAL
      XIMAG(I)=TIMAG
  105 CONTINUE
      RETURN
      END
      FUNCTION IBITR(J,NU)
      J1=J
      IBITR=0
      DO 200 I=1,NU
      J2=J1/2
      IBITR=2*IBITR+(J1-2*J2)
  200 J1=J2
      RETURN
      END
```

ACKNOWLEDGEMENTS

I wish to thank my supervisor, Professor D.J. Bradley, F.R.S., for his encouragement and guidance during the period of my Ph.D. I would also like to express my sincere thanks to Dr. M.H.R. Hutchinson and Dr. Wilson Sibbett for many useful and enlightening discussions over the past six years.

Many thanks are especially due to Dr. Roy Taylor, whose positive and imaginative approach to experimental physics always proved invaluable, and occasionally inspirational.

I would like to thank the members of staff, both academic and technical, who provided help at some stage during this work. These include Drs. Bill Sleat and Paul Smith, and Mr. ~~George Buzby~~ Graham Busby, who helped with the electronic aspects of this work, Maurice Pimm of the Research Workshop, Nick Jackson of the Photography Section, and the group technicians, Basil Weekley and Roy Morrison.

Thanks are also due to Dr. John Elgin for his advice on the theoretical aspects of this work, and Charles Penman for his help with the computer program.

I would like to acknowledge the many members, both past and present, of the Laser Group whom I have been fortunate enough to work alongside during my stay here, and my friends in the Electron Diffraction, Spectroscopy and Plasma groups of this department, who made my social life enjoyable.

Thanks are also due to Sarah MacGowan for her accurate and efficient typing of this thesis, and to Joe Willson for proof-reading the manuscript.

Finally my thanks are due to Miss Betty Brown, and to Miss Akgün Özkök and Mr. Ersoy Ataser who provided accommodation rent-free during a period of financial hardship, and, most importantly of all, to my parents for their unswerving moral support and encouragement.

This work was supported by an S.R.C. Postgraduate studentship and a departmental Research Assistantship.

REFERENCES

1. P.A. Franken, A.E. Hill, C.W. Peters, G. Weinreich, Phys. Rev. Lett. 7, 118 (1961).
2. W. Kaiser, C.G.B. Garrett, Phys. Rev. Lett. 7, 229 (1961).
3. H.W. Mocker and R.J. Collins, Appl. Phys. Lett. 7, 270 (1965).
4. M. Matsuoko, H. Nakatsuka, J. Okada, Phys. Rev. A. 12, 1062 (1975).
5. T.R. Royt, C.H. Lee, Opt. Commun. 18, 108 (1976).
6. D.J. Bradley, C.H. Dugan, P. Ewart, A.F. Purdie, Phys. Rev. A. 13, 1416 (1976).
7. I.V. Tomov, R. Fedosejevs, M.C. Richardson, W.J. Sarjeant, A.J. Alcock, K.E. Leopold, Appl. Phys. Lett. 30, 146 (1977).
8. I.V. Tomov, R. Fedosejevs, M.C. Richardson, W.J. Sargeant, A.J. Alock, K.E. Leopold, Appl. Phys. Let. 31, 747 (1977).
9. G. Reksten, T. Varghese, D.J. Bradley, Appl. Phys. Lett. 38, 513 (1981).
10. M. Bass, P.A. Franken, A.E. Hill, C.W. Peters, G. Weinreich, Phys. Rev. Lett. 8, 18 (1962).
11. J.A. Giordmaine, Phys. Rev. Lett. 8, 19 (1962).
12. P.D. Maker, R.W. Terhune, M. Nissenoff, C.M. Savage, Phys. Rev. Lett. 8, 21 (1962).
13. J.F. Ward, G.H.C. New, Phys. Rev. 185, 57 (1969).
14. R.B. Miles, S.E. Harris, IEEE J. QE-9, 470 (1973).
15. D.M. Bloom, J.F. Young, S.E. Harris, Appl. Phys. Lett. 27, 390 (1975).
16. R.T. Hodgson, P.P. Sorokin, J.J. Wynne, Phys. Rev. Lett. 32, 343 (1974).

17. D.M. Bloom, J.T. Yardley, J.F. Young, S.E. Harris, Appl. Phys. Lett. 24, 427 (1974).

18. S.C. Wallace, G. Zdasuik, Appl. Phys. Lett. 28, 449 (1976).

19. T.J. Mckee, B.P. Stoicheff, S.C. Wallace, Optics Lett. 3, 207 (1978).

20. H. Junginger, H.B. Puell, H. Scheingraber, C.R. Vidal, IEEE J. QE-16, 1132 (1980).

21. T.H. Mazman, Nature 187, 493 (1960).

22. H.W. Mocker, R.J. Collins, Appl. Phys. Lett. 7, 270 (1965).

23. T.H. Mazman, Phys. Rev. Lett. 4, 564 (1960).

24. D.N. Dempster, T. Morrow, R. Rankin, G.F. Thompson, Chem. Phys. Lett. 22, 222 (1973).

25. M.S. Petty, PhD Thesis, Queen's University of Belfast, 1970.

26. D.J. Bradley, G.H.C. New, Proc. IEEE, 62, 313 (1974).

26. H. Kogelnik, T. Li., Appl. Opt. 5, 1550 (1966)
Proc. IEEE, 54, 1312 (1966).

28. V.S. Letokhov, Soviet Phys. J.E.T.P. 28, 562 (1969)
Soviet Phys. J.E.T.P. 28, 1026 (1969).

29. J.A. Fleck, Appl. Phys. Lett. 12, 178 (1968)
J. Appl. Phys. 39, 3318 (1968)
Phys. Rev. B. 1, 84 (1970).

30. G.H.C. New, Proc. IEEE 67, 380 (1979).

31. R.C. Eckart, C.H. Lee, J.N. Bradford, Opto.-Electron. 6, 67 (1974).

32. S.D. Zacharov, P.G. Kryukov, Yu. A. Matveets, S.V. Chekalin, S.A. Churilova, O.B. Shatsbershvili, Sov. J.Q.E. 3, 395 (1974).

33. E.G. Arthurs, D.J. Bradley, T. Glynn, Opt. Commun. 12, 136 (1974).

34. W.H. Glenn, IEEE J.QE-11, 8 (1975).

35. M.S. Demokan, P.A. Lindsay, Int. J. Electron. 42, 313 (1977).

36. P.G. Kryukov, V.S. Letokhov, IEEE J. QE-8, 766 (1972).

37. D.J. Bradley in "Ultrashort Light Pulses", pp 17-81 "Topics in Applied Physics" Vol. 18 Ed. S.L. Shapiro (Springer Verlag, 1977).

38. D. von der Linde, IEEE J. QE-8, 328 (1972).

39. A. Yariv, Quantum Electronics 2nd Edn. p.137 (Wiley, New York, 1975).

40. H. Kogelnik in "Modes in Optical Resonators" pp. 295-347, "Lasers" Vol. 1 Ed. A.K. Levine (Edward Arnold, London 1966).

41. Laser-Fusion Program Semiannual Report Jan-June 1973, Lawrence Livermore Laboratory, UCRL-50021-73-2.

42. A.N. Zherikhus, V.A. Kovalenko, P.G. Krinkov, Yu. A. Matveetz, S.V. Chekalin, and O.B. Shatberashvili, Sov. J. Quant. Electron. 4, 210 (1977).

43. D.J. Bradley, B. Liddy, W.E. Sleat, Opt. Commun. 2, 391 (1971).

44. H. Tashiro, J. Schultz-Hennig, A. Müller, Opt. Commun. 27, 442 (1978).

45. P.A. Franken, A.E. Hill, C.W. Peters, G. Weinreich, Phys. Rev. Letts. 7, 118 (1961).

46. A. Yariv, Quantum Electronics, 2nd Edn. pp.407-433 (Wiley, New York 1975).

47. D.A. Kleinman, Phys. Rev. 126, 1977 (1962).

48. P.D. Maker, R.W. Terhune, M. Nissenhoff, C.M. Savage, Phys. Rev. Lett. 8, 21 (1962).

49. J.A. Giordmaine, Phys. Rev. Lett.8, 19 (1962).

50. J.E. Midwinter, J. Warner, Brit. Journ. App. Phys. 16, 1135 (1965).

51. D.A. Kleinman, Phys. Rev. 128, 1761 (1962).

52. G.D. Boyd, A. Ashkin, J.M. Dziedzic, D.A. Kleinman, Phys. Rev. 137, 1305 (1965).

53. A. Ashkin, G.D. Boyd, J.M. Dziedzic, Phys. Rev. Letts. 11, 14 (1963).

54. R.S. Adhav, A.D. Vlassopoulous, Laser Focus, 10, 47 (1974).

55. F. Zernike, Jour. Opt. Soc. Am. 54, 1215 (1964).

56. B. Weekly - Private Communication.

57. R.C. Miller, Phys. Letts. 26A, 1977 (1968).

58. G.C. Bjorklund, IEEE J. QE-11, 287 (1975).

59. I.V. Tomov, M.C. Richardson, IEEE J. QE-12, 521 (1976).

60. J.E. Bjorkholm, Phys. Rev. 142, 126 (1965).

61. J.A. Armstrong, N. Bloembergen, J. Ducuing, P.S. Pershan, Phys. Rev. 127, 1918 (1962).

62. J. Ducuing, in Quantum Optics, Proc. Int. School of Physics "Enrico Fermi" Course XLII, Ed. R.J. Glauber (Academic Press, New York 1969) pp 421-472.

63. P.N. Butcher, "Non linear Optical Phenomena" Bulletin 200 Eng. Expt. Station, Ohio State University (1965).

64. F. Zernike and J.E. Midwinter, "Applied Nonlinear Optics" (Wiley-Interscience, New York, 1973).

65. N. Bloembergen "Nonlinear Optics" (Benjamin, New York 1965).

66. J.F. Ward, Rev. Mod. Phys. 37, 1 (1965).

67. D.C. Hanna, M.A. Yuratich, D. Cotter, "Nonlinear Optics of Free Atoms and Molecules" Ed. D.L. MacAdam (Springer Verlag Press 1979) pp 36-41.

68. C.E. Moore, "Atomic Energy Levels", Circular Nat. Bur. Standards No. 467, Vol. 1, 1949.

69. Wiese, Smith, Miles, "Atomic Transition Probabilities - Sodium through Calcium", NSRDS-NBS 22 Vol 11 (1969).

70. C.J. Mitchell, J. Phys. B. 1, 25 (1975).

71. B.W. Shore, D.H. Menzel, "Principles of Atomic Spectra" (Wiley, New York, 1968).

72. I.I. Sobel'man, "An Introduction to the theory of Atomic Spectra" (Pergamon Press 1972).

73. A.R. Edmonds, "Angular Momentum in Quantum Mechanics" (Princeton Univ. Press, Princeton 1960).

74. J. Koch, Kungl. Fysiografiska Sallskapets I Lund Forhandlingar 19, 173 (1949).

75. R.E. Honig, D.A. Kramer, R.L.A. Review, 30, 287 (1969).

76. G.M. Grover, T.P. Cotter, G.F. Erikson, J. Appl. Phys. 35, 1990 (1964).

77. C.R. Vidal, J. Cooper, J. Appl. Phys. 40, 3370 (1969).

78. M.M. Hessel, T.B. Lucatorto, Rev. Sci. Instr. 44, 561 (1973).

79. J.R. Taylor, PhD Thesis, Queen's University of Belfast, 1974.

80. C.B. Edwards - Private Communication.

81. P. Dobson - Private Communication.

82. D.C. Hanna, M.A. Yuratich, D. Cotter, "Nonlinear Optics of Free Atoms and Molecules", Ed. D.L. MacAdam (Springer Verlag Press, 1979) p.169.

83. J.N. Elgin - Private Communication.

84. T.J. McIlrath, T.B. Lucatorto, Phys. Rev. Lett. 37, 428 (1976).

85. T.J. McIlrath, T.B. Lucatorto, Phys. Rev. Lett. 38, 1390 (1977).

86. A.H. Kung, J.F. Young, G.C. Bjorklund, S.E. Harris, Phys. Rev. Lett. 29, 985 (1972).

87. J.R. Taylor, Opt. Comm. 18, 504 (1976).

88. F.G. Houtermans, Helveta Physica Acta. 33, 933 (1960).

89. N.G. Basov, IEEE J. QE-2 354 (1966).

90. R.S. Mulliken, Journ. Chem. Phys. 52, 5170 (1970).

91. D.K. Anderson, Phys. Rev. 137A, 21 (1965).

92. G. Herzberg "Spectra of Diatomic Molecules" (D. van Nostrand Co. Inc. 1950).

93. D. Hull, PhD Thesis, University of London, 1975.

94. D. Smith, A.G. Dean, I.C. Plumb, Journ. Phys. B5, 2134 (1972).

95. D.R. Bates, Phys. Rev. 78, 492 (1950).

96. E.V. George, C.K. Rhodes, Appl. Phys. Lett. 23, 139 (1973).

97. G.R. Fournier, Opt. Commun. 13, 385 (1975).

98. D.J. Bradley, M.H.R. Hutchinson, H. Koetser, Opt. Commun. 7, 187 (1973).

99. H.A. Koehler, L.J. Ferderber, D.L. Redhead, P.J. Ebert, Phys. Rev. A9, 768 (1973).

100. J.B. Gerado, A.W. Johnson, IEEE, J. QE-9, 748 (1973).

101. F.H. Mies, Mol. Phys. 26, 1233 (1973).

102. F.H. Fink, F.J. Comes, Chem. Phys. Lett. 30, 267 (1975).

103. C.B. Edwards, PhD Thesis, University of London, 1978.

104. L. Spitzer, "Physics of Fully Ionized Gases" (Wiley, New York 1967).

105. E. Oran Brigham "The Fast Fourier Transform" (Prentice-Hall, Inc. Englewood Cliffs, New Jersey, 1974).